Event-by-event Fluctuations of Charged and Neutral Kaons in Pb-Pb collisions at $\sqrt{s_{\mathrm{NN}}}$ = 2.76 TeV with ALICE at the LHC

A Thesis
Submitted in partial fulfillment of
the requirements for the degree of
Doctor of Philosophy
by

Ranjit Kumar Nayak
(154120015)

Supervisor:
Prof. Sadhana Dash
Co−Supervisor:
Prof. Claude A. Pruneau

Department of Physics
Indian Institute of Technology Bombay
Mumbai 400076 (India)

May 2020

Dedicated to my family and teachers

Acceptance Certificate

Department of Physics

Indian Institute of Technology, Bombay

The thesis entitled “Event-by-event Fluctuations of Charged and Neutral Kaons in Pb-Pb collisions at $\sqrt{s_{\mathrm{NN}}}$ = 2.76 TeV with ALICE at the LHC” submitted by Ranjit Kumar Nayak (154120015) may be accepted for being evaluated.

Date: May 2020

Prof. Sadhana Dash

Approval Sheet

This thesis entitled "Event-by-event Fluctuations of Charged and Neutral Kaons in Pb-Pb collisions at $\sqrt{s_{NN}}$ = 2.76 TeV with ALICE at the LHC" by Ranjit Kumar Nayak is approved for the degree of Doctor of Philosophy.

Pradip Sahu

Examiners

Sadhana Dash

Supervisor (s)

Biswal

Chairman

Date: 4.5.20

Place: Mumbai

Declaration

I declare that this written submission represents my ideas in my own words and where others' ideas or words have been included, I have adequately cited and referenced the original sources. I declare that I have properly and accurately acknowledged all sources used in the production of this report. I also declare that I have adhered to all principles of academic honesty and integrity and have not misrepresented or fabricated or falsified any idea/data/fact/source in my submission. I understand that any violation of the above will be a cause for disciplinary action by the Institute and can also evoke penal action from the sources which have thus not been properly cited or from whom proper permission has not been taken when needed.

Ranjit Kumar Nayak

Date: 3 May 2020 (154120015)

Abstract

In ultra-relativistic heavy-ion collisions, the normal hadronic matter undergoes a transition to a deconfined phase of quarks and gluons. The produced partons interact with each other to form a strongly correlated system of QCD matter widely known as quark-gluon plasma (QGP). The primordial state of matter was believed to have existed for a few millionths of second shortly after the Big Bang. The matter which was created at very high energy density and temperature undergoes a collective expansion and eventually hadronizes. As per Lattice QCD, in the limit of zero baryo-chemical potential and high temperature, hadronic matter is expected to show a phase transition to a deconfined state where the effective mass of quark is zero. The chiral symmetry is expected to be restored. However, strong experimental evidence of the restoration of chiral symmetry in heavy-ion collisions is yet to be observed. Further, it is still a matter of speculation if the de-confinement phase transition and the chiral phase transition occur at the same temperature. Several experimental searches have been made in recent years to understand the de-confinement phase transition while the chiral phase transition is still a mystery for high energy physicists.

The analysis of the event-by-event fluctuations of charged and neutral kaons in Pb-Pb collisions at $\sqrt{s_{\mathrm{NN}}} = 2.76$ TeV is presented using the data collected by ALICE detector at the LHC. The analysis is carried out for different centrality classes (namely 0-10%, 10-20%, 20-40%, 40-60%, and 60-80%). The event and track selection cuts are used to obtain quality tracks. The combined information of TPC and TOF detectors are used to identify charged kaons. The K_s^0s are reconstructed from the invariant mass analysis of their hadronic decay channel $K_s^0 \rightarrow \pi^+ + \pi^-$. These are selected after implementing various topological cuts based on decay length, Cosine of pointing angle (Cos(PA)), Armenteros-Podolanski parameter, DCA to primary vertex, etc. The combinatorial background (due to random $\pi^+\pi^-$ pairs not originating from K_s^0 decay vertex) present in the selected mass range of $\pi^+\pi^-$ invariant mass distribution is accounted for by performing a detailed background correction. The yield of $K^\pm$s and K_s^0s are corrected for detector efficiency and limited detector acceptance. The statistical uncertainty is estimated using the

sub sample method. The systematic uncertainties due to various sources are estimated for each centrality class. The effect of centrality bin width correction has also been studied.

The obtained values of $\nu_{dyn}[K_s^0, K^{\pm}]$ are studied as a function of centrality. The measured $\nu_{dyn}[K_s^0, K^{\pm}]$ values monotonically decrease from peripheral to central collisions. The values are also compared to the expectation of HIJING and AMPT (3 modes) MC models. The estimated values from both the models show similar trend as a function of collision centrality and underestimate the measured values. The $\nu_{dyn}[K^+, K^-]$ is also estimated and compared to the MC expectations as a function of collision centrality. The obtained values are negative and the magnitude decreases from peripheral to central collisions. The MC estimations also show a good agreement with the measured values. The observation is attributed to the charge conservation as charged kaons are predominately produced by pair creation. The scaled values of measured $\nu_{dyn}[K_s^0, K^{\pm}]$ (scaled with the number of sources approximated as $\langle dN_{ch}/d\eta \rangle$) exhibit a violation of source scaling, however, the violation is not observed in MC models. The scaled $\nu_{dyn}[K^+K^-]$ exhibits some collision centrality dependence, and the implied scaling violation is considerably smaller than that observed for $\nu_{dyn}[K_s^0, K^{\pm}]$. The study indicates that the correlated production of neutral and charged kaons is different from the correlated production of oppositely charged kaons.

A simple toy model simulation of the implementation of DCC like events is carried out to study the sensitivity of the ν_{dyn} observable in the presence of DCC like events at LHC energy. The $\nu_{dyn}[K_s^0, K^{\pm}]$ is estimated as a function of centrality for four different scenarios related to the size and number of DCC domains. For a given centrality class, $\nu_{dyn}[K_s^0, K^{\pm}]$ shows a monotonic increase with the size of the DCC domain and has a large magnitude for the events containing large DCC domains in this study. The values of $\nu_{dyn}[K_s^0, K^{\pm}]$ scaled by the mean of the number of kaons ($\sqrt{\langle N_{K_s^0} \rangle \langle N_{K^{\pm}} \rangle}$) and mean charged-particle multiplicity ($\langle dN_{ch}/d\eta \rangle$) are observed to be independent of the considered collision centrality class for the baseline measurement, where DCC fluctuations are not introduced. However, with the implementation of DCC fluctuations in the MC model, the scaled values are no longer invariant with centrality classes but sharply increase for most central collisions. The scaled values of the MC (containing DCC fluctuations) are consistent with the ALICE measurement for $\nu_{dyn}[K_s^0, K^{\pm}]$.

The mechanism of particle production in high energy hadronic and heavy-ion collisions are studied using different phenomenological approaches. The first approach involves a two-component Glauber model, which is used to describe the contribution of hard and soft processes towards particle production in heavy-ion (Au-Au and Pb-Pb) collisions. The model describes the charged particle multiplicity density and the transverse

energy density quite well. It is observed that the fractional contribution of hard processes increases with an increase in beam energy. A pairwise ratio of multiplicity densities for two different energies is obtained for similar $\langle N_{part} \rangle$ values. A scaling observed for the pairwise ratio indicates that the observed trend is due to the contribution from the hard scattering component and the energy difference while the same is not observed for transverse energy densities. The second approach involves the study of the normalized moments of multiplicity distribution in pp collisions in the forward rapidity region using the Weibull model. Two different event classes, NSD (non-singly diffractive events) and INEL > 0 (inelastic events having at least one charged particle for $|\eta| < 1.0$) are considered in this study. The model describes the charged particle multiplicity distributions quite well. The higher order normalized cumulants and factorial moments (upto 5^{th} order) are calculated from the extracted fit parameters in different event classes for various η intervals. The normalized cumulants and factorial moments show an increasing trend with the increase in energy for all η windows, however, the second order moments exhibit no beam energy dependence. The observed trend of the higher order moments with the beam energy suggests a strong violation of KNO scaling in forward regions, obtained for both NSD and INEL > 0 event classes. The third approach involves the study of enhancement of strange particles in high multiplicity pp collisions using rope hadronization mechanism implemented in PYTHIA8 model. The measured strangeness enhancement in pp collisions at $\sqrt{s} = 7$ TeV in ALICE is well described by the rope hadronization mechanism within the framework of color reconnection, while the values obtained without the effect of rope hadronization fail to describe the measured data. The values obtained from the rope hadronization without the color reconnection also fail to describe the data, which indicates that the color reconnection framework is needed with the rope hadronization mechanism to describe the enhancement in data. The observed enhancement of strange particle saturates at higher multiplicities and is independent of the collision energies.

Table of Contents

List of Figures

List of Tables

Chapter 1

Introduction

The quest for the understanding of the vast universe began in antiquity. The interplay of science and technology has enabled our society to prosper and flourish. Physics is the study of natural phenomena and the constituents of matter. The laws of physics are the same for an object irrespective of its position and time in the universe. If the experimental observations are performed correctly, they lead to the same results.

The most elementary and fundamental question in physics one can easily ask is “what are things made up of?" The answer can be given by considering an object and studying its constituents. A new type of substructure appears when the constituents are studied on a more fundamental level. At the beginning of the twentieth century, Rutherford discovered that atoms have a small and dense nucleus. After years of studies of the nucleus, it was found that the nucleus has a substructure. It consists of neutrons and protons, known as nucleons. The deep inelastic experiment performed in 1968 [1] confirmed that protons and neutrons consist of quarks.

Everything in the universe is found to be made up of fundamental particles governed by four fundamental interactions. The Standard Model [2] explains how the basic building blocks of matter are governed and interact among themselves. The Standard Model describes three of the four known fundamental interactions i.e, the Electromagnetic, the Weak, and the Strong interactions between elementary particles. However, the most familiar force experienced in our everyday lives, Gravitation, is not a part of the Standard Model. Integrating this interaction into this framework has proved to be a difficult challenge. It has been a difficult task to unify the quantum theory that describes the microscopic world, and the general theory of relativity which describes the macroscopic world. The four fundamental interactions have different ranges and different strengths. Gravity is the weakest but can be experienced at infinite distance. The range of electromagnetic interaction is also infinite but the interaction is stronger than gravity. The Weak

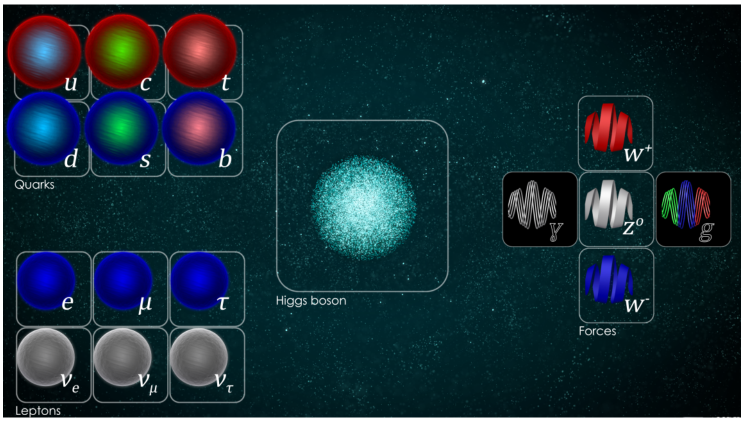

Figure 1.1: The list of elementary particles in the Standard Model [3].

and Strong forces are short range forces and are effective at the level of subatomic particles. As the name suggests, the Strong force is the strongest of all interactions. The Standard Model combines the Electroweak theory (a combined theory of Electromagnetic and Weak interactions) with Quantum Chromodynamics (QCD) which is the theory of the Strong interaction. These fundamental forces operate by the exchange of force carrier particles called gauge bosons. Each fundamental force has its own carrier. These carriers are known as bosons having spin-1. The “gluon" is the mediator of the Strong force. The Electromagnetic force is mediated by the “photon", and the “W and Z bosons" mediate the Weak force. The “graviton" is conjectured to be the mediating particle of Gravity. However, no evidence for the existence of graviton has been provided so far by experimental measurements. On 4^{th} July 2012, the Large Hadron Collider (LHC) at the European Organization for Nuclear Research (CERN) confirmed the discovery of Higgs boson. It is a spin-0 particle and it explains the generation of mass in elementary particles.

The elementary particles of the Standard Model are shown in Fig. 1.1 along with the Higgs boson.

Proton and neutron are the lightest particles in a strongly interacting state of fermions known as baryons. They contain three quarks. There also exist strongly interacting bosonic states called mesons, which contain a quark and an anti-quark. Baryons and mesons are collectively called hadrons. The electron, muon, tau particle, and their corresponding neutrinos form a separate group of weakly interacting particles widely known as leptons. Neutrinos take part in the Weak interaction only, but the electrons can also experience Electromagnetic interaction. The theory of Electromagnetic interaction which involves the exchange of massless photons is known as quantum electrodynamics (QED). Leptons are the elementary point-like particles with no known substructure. The Strong force is usually observed at two ranges. This force is responsible for the binding of protons and neutrons to form nucleus mediated by mesons. At short ranges, this force is responsible for the binding of quarks into hadrons. The theory of Strong interaction, which involves the exchange of gluons between quarks, is called quantum chromodynamics (QCD) [4].

1.1 Theory of Strong Interaction

QCD, much like QED is a gauge field theory described by a Lagrangian. In QCD, the Lagrangian is required to be invariant under SU (3) group transformation. The symmetry of the Lagrangian under SU (3) transformation, introduces color charges. The QCD Lagrangian density is given by,

$$\mathcal{L} = -\frac{1}{4}G^{\mu\nu}_a G^a_{\mu\nu} + \sum_{flavours} \bar{q}(i\gamma^\mu D_\mu - m_q)q, \tag{1.1}$$

where

$$D_\mu = \partial_\mu - ig\frac{\lambda_a}{2}A^a_\mu(x), \tag{1.2}$$

and

$$G^a_{\mu\nu}(x) = \partial_\mu A^a_\nu(x) - \partial_\nu A^a_\mu(x) + f_{abc}A^b_\mu(x)A^c_\nu(x), \tag{1.3}$$

where f_{abc} corresponds to SU(3) group structure constants, λ_a are the Gell-Mann matrices, and $A^a_\mu(x)$ corresponds to eight vector gauge fields. According to QCD, spin-$\frac{1}{2}$ quarks and spin-1 gluons are the basic building blocks of all matter and they interact strongly. In QED there are two kinds of charges, historically denoted as positive (+) and negative (-), whose interaction is mediated by photons with no electric charge. The theory of QED is an Abelian gauge theory, where the elements of the gauge group obey commutative law. However, QCD is a non Abelian gauge theory (non-commutative) consisting of 6 flavours known as quarks and mediated by 8 colored gluons. Unlike photons, gluons have self interaction due to their color charge. Although gluons are massless, they act at very short distances giving rise to a short range color force. The Cornell potential for the Strong force between quark-antiquark interaction consists of two terms as given in Eq. 1.4.

$$V(r) = -\frac{4}{3}\frac{\alpha_s}{r} + kr. \tag{1.4}$$

The Coulomb potential ($\propto$ 1/r) dominates at small distance r whereas the linear term is responsible for the confinement of quarks. The linear term is also responsible for the production of mesons and baryons. The properties of QCD can be understood by studying the Strong interaction coupling constant given by,

$$\alpha_s(Q^2) = \frac{4\pi}{(11 - 2n_f/3)lnQ^2/\Lambda^2}, \tag{1.5}$$

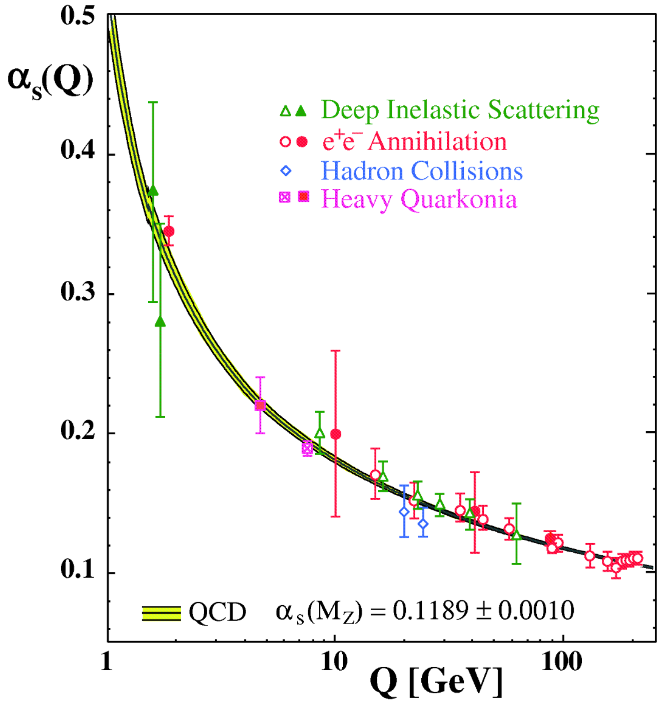

Figure 1.2: The variation of α_s(Q) as a function of momentum transfer from different experiments. The solid lines represent the QCD predictions [5].

where Q^2 is the momentum transfer, n_f is the number of quark flavours, and Λ is a scaling parameter. From the above equation, it is clear that the strong interaction coupling constant decreases with increasing momentum transfer and for large values of Q^2, the coupling $\alpha_s(Q^2) \to 0$. This phenomenon at large Q^2 is historically known as asymptotic freedom. It was first predicted by Politzer [6], Gross and Wilczek [7] in 1973 and they were awarded Nobel prize in the year 2004 for this discovery. Fig. 1.2 depicts the variation of $\alpha_s(Q^2)$ as a function of momentum transfer. For low momentum transfer and large distances, $\alpha_s(Q^2)$ becomes very large and color charged particles cannot be found in isolation. This property of quarks at large distances is called color confinement and also known as infra-red slavery. As a consequence of these two remarkable properties of QCD, the QCD medium at very high temperatures and energy densities is expected to exist in a deconfined state of quarks and gluons interacting through colour charge.

1.2 Phase Transitions in QCD

As mentioned in the previous section, QCD predicts that a deconfined state of quarks and gluons in the QCD medium is expected to be formed at high energy densities and high temperatures. The normal hadronic matter of colour singlet state undergoes a phase transition to a state where quarks and gluons are no longer confined inside bound state

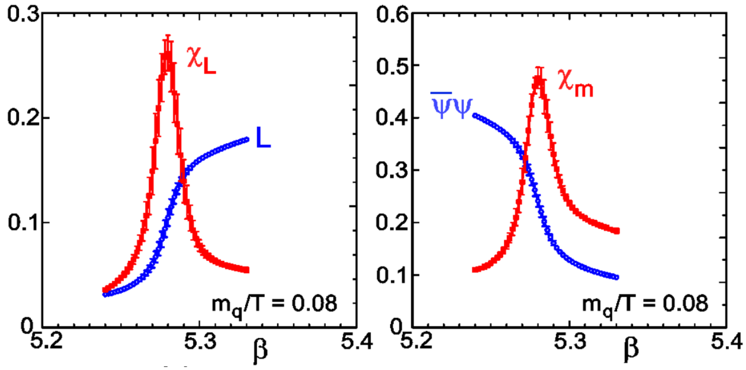

Figure 1.3: The Polyakov loop (**Left panel**) and the chiral susceptibilities (**Right panel**) versus gauge coupling, β in 2 flavour QCD. $< L >$ is the order parameter for deconfinement in the pure SU(3) symmetry ($m_q \to \infty$). $< q\bar{q} >$ is the the order parameter for chiral phase transition in the chiral limit ($m_q \to 0$) [8].

hadrons. The phase transition in QCD can be described in a similar way as the phase transition in water, where different forms of water are illustrated in different regions of a phase diagram and are characterized by the thermodynamic parameters in those regions. The chiral symmetry is a symmetry of QCD Lagrangian in vacuum in the limit of vanishing quark masses. At low temperature and large distances (~ 1 fm), and finite value of quark masses, chiral symmetry is broken and quarks are confined inside hadrons. The chiral symmetry is characterized by an observable called quark (or chiral) condensate, $< q\bar{q} >$ which has a non-zero value for the chiral symmetry broken phase. The chiral symmetry is approximately restored in a system at high temperatures and the condensate vanishes, $< q\bar{q} > = 0$.

The Lattice QCD suggests that at the limit of zero baryonic-chemical potential and high temperature, the hadronic matter shows a phase transition to a deconfined phase and chiral symmetry might be restored. But, there is no experimental evidence to indicate whether the de-confinement phase transition and chiral phase transition (where chiral symmetry is restored), occur at the same temperature. From simulation studies [8, 9], it has been predicted that both transitions occur approximately at the same temperature even though the two are physically distinct. A system which undergoes a phase transition is characterized with an order parameter which has different values in different phases of the matter. The de-confinement transition is associated with Polyakov loop, $< L >$ as its order parameter, while chiral transition has the quark condensate, $< q\bar{q} >$ as its order parameter [8, 9]. Fig. 1.3 shows the behaviour of the chiral (χ_m) and Polyakov loop (χ_L) susceptibilities from two transitions as a function of the gauge coupling ($\beta \propto$ T). Both the transitions exhibit a rapid change of their order parameters at a particular tempera-

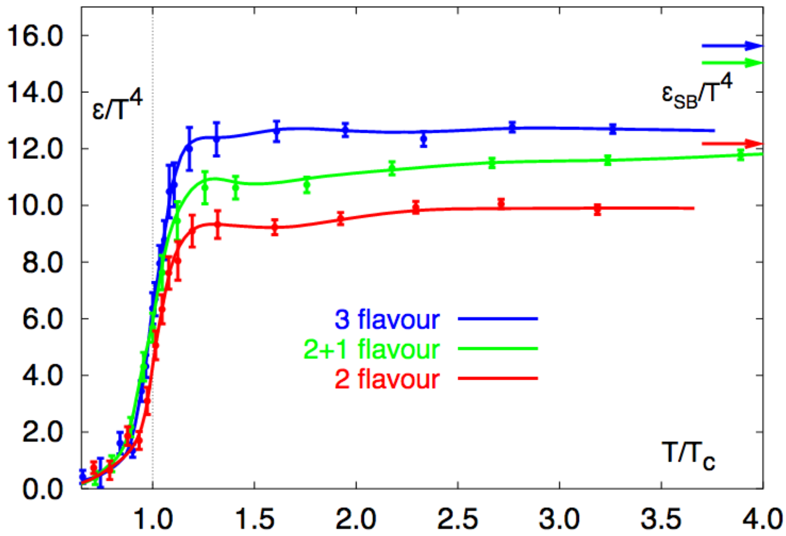

Figure 1.4: The energy density calculated in Lattice QCD for different number of flavours. 2+1 flavour QCD represents the QCD with two light quarks (up and down) and a heavier strange quark. [10].

ture. The susceptibilities of the two transitions also reach their maxima at nearly the same temperature. Even though the transitions can be a smooth cross-over (not of first order), the temperature at which the susceptibilities reach their maximum is commonly known as “critical temperature".

Lattice QCD (LQCD) calculations predict that the transition from a hadronic phase to QGP phase occurs within a temperature range of $T_c \sim$ 150-200 MeV and at an energy density of $\sim$ 1 GeV/fm^3 [10]. LQCD simulations are performed on a discrete space-time lattice. The thermodynamic properties such as energy density, pressure, and entropy density are studied as a function of temperature. Fig. 1.4 displays the energy density as a function of critical temperature (T/T_c). It shows that the energy density scaled by the temperature, ϵ/T^4, sharply rises over a narrow temperature range of 150-200 MeV and saturates at a very high temperature. The values obtained from LQCD calculations are substantially lower than the Stefan-Boltzmann limit. This implies that at high but finite temperature, constituents of QGP are not free. Fig. 1.4 depicts that the number of degrees of freedom rapidly increases indicating a de-confinement phase transition.

The experimental measurements conducted so far suggest that the matter produced in relativistic heavy-ion collisions is in the form of a quasi-perfect QCD fluid. A gaseous plasma that is believed to have existed in the early universe is expected to be formed if the temperature is increased beyond T_c. However, at lower temperatures and high baryon densities, a color superconducting plasma state is expected to be formed which exists in

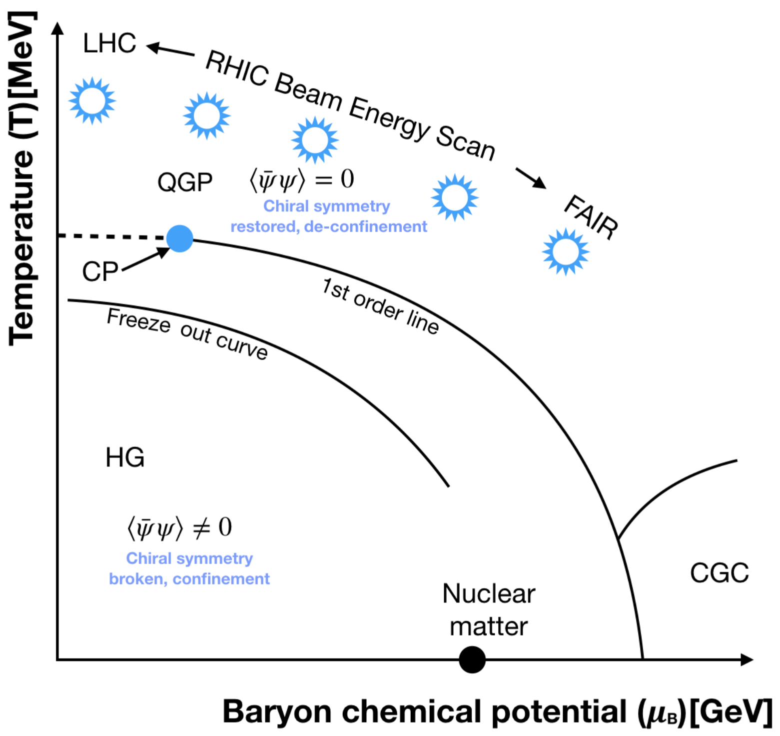

Figure 1.5: The schematic diagram of the QCD phase transition

the core of the neutron stars [11]. The various phases of QCD matter are shown in Fig. 1.5 as a function of temperature (T) and baryonic chemical potential (μ_B). The Lattice calculations along with the predictions of QCD based models predict the existence of a first order phase transition at high baryon densities. The QCD critical point (CP) lies at the endpoint of the first order transition. At very low μ_B and high temperature, there exists a cross over [12] which is shown as a dotted line in Fig. 1.5.

1.3 Collision of Heavy Ions and the Picture of Space-Time Evolution

It is believed that after the Big Bang, QGP is thought to have existed for a millionth of second. The temperature of the universe at that time is estimated to be around 2000 billion degrees. It is a challenging task for physicists to study the fundamental constituents of matter at high temperature and energy density. The observation and study of this novel state of matter can be achieved by colliding heavy-ions at extremely high energies in accelerators such as the Relativistic Heavy Ion Collider (RHIC) and the Large Hadron Collider (LHC).

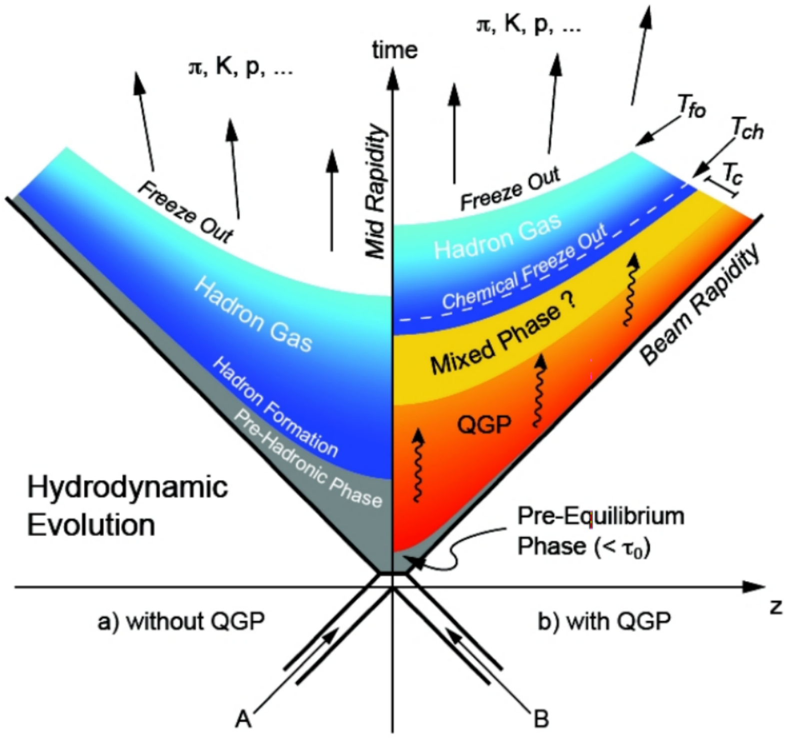

Figure 1.6: The schematic showing the space-time diagram of QGP evolution

When two nuclei moving with relativistic speed collide head-on, a fireball is created. The evolution of this fireball is described by considering the space-time (z,t) diagram as shown in Fig. 1.6.

In the initial stages of the collision, due to parton-parton hard scatterings, a large amount of energy is deposited which leads to the creation of hot medium. This pre-equilibrium phase is estimated to last for 1 fm/c or less. The dynamics of this phase is computed with perturbative QCD. Soon after the pre-equilibrium phase, multiple partonic interactions lead to the formation of a thermally equilibrated state known as QGP phase. The rapid expansion of the system decreases the temperature of the medium. As the system expands from the QGP phase to the hadronic phase, a mixed phase consisting of a mixture of QGP and hadrons is expected to occur through the critical temperature. A mixed phase may exist for a longer lifetime (> 10 fm/c) as hadrons require a finite time to form. The collective expansion exists even inside the hadronic phase due to hadronic interactions and it continues until a temperature, T_{ch} is reached. At this temperature, the inelastic interactions between the hadrons cease, which oppose any formation of new particles. This is called chemical freeze-out. However, the elastic interactions continue until the mean free path of hadrons exceeds the system size. The temperature at which elastic interactions stop and particles freely stream out is called kinetic freeze-out.

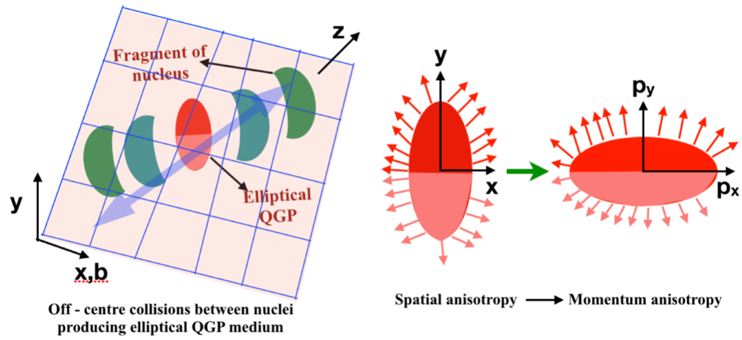

Figure 1.7: The schematic diagram showing elliptic flow in heavy-ion collisions.

1.4 Observable Used in the Study of QGP

The deconfined state of matter produced in heavy-ion collisions cannot be measured directly. Different proposed probes are considered to study the QGP formation in experiments. Experimental probes used to study the QGP formation are divided into two categories - hard probes and soft probes. The hard probes are the ones which probe the initial stages of the collisions and consist of signatures like Jet quenching, formation of bound states of heavy quarks, thermal photons, dilepton production etc. The soft probes include the signals of bulk matter such as strangeness enhancement, flow, particle spectra, correlations and fluctuations. These provide information about spatial evolution and the degree of thermalization. Some of the signatures are discussed in the following sections.

1.4.1 Fluid Like Property of the Medium

The matter created in heavy-ion collisions undergoes collective expansion due to a large pressure gradient. This collective expansion, or flow, is one of the prime signatures of the QGP medium. The hadrons carry the encrypted message of the initial stage information. The study of the transverse momentum spectra of produced particles after freeze-out reveals the properties of the initial stages. The study of the collective flow of the deconfined medium provides essential information about the equation of state of matter. The collective flow is classified into radial flow and anisotropic flow. In non-central collisions (with non-zero impact parameter), the initial stage spatial anisotropy is converted into anisotropy in momentum-space. The correlation between spatial positions and momentum of the emitted particles is measured by Fourier expansion of the azimuthal momentum distribution [13, 14, 15], given by,

$$E\frac{d^3N}{dp^3} = \frac{1}{2\pi}\frac{d^2N}{p_T dp_T dy}[1 + 2\sum_n v_n cos[n(\phi - \Psi_n)]], \tag{1.6}$$

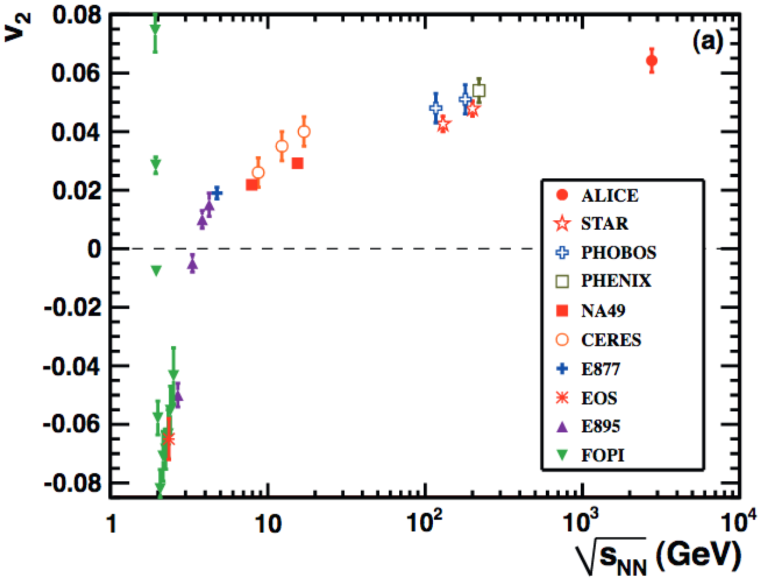

Figure 1.8: The variation of integrated elliptic flow as a function of collision energy in the 20-30% centrality class [23].

where v_n's are the flow harmonics, ϕ is the azimuthal plane angle and Ψ_n is the reaction plane angle. The first three Fourier coefficients, v_1, v_2, and v_3 are widely known as directed flow, elliptic flow, and triangular flow respectively. The collective expansion of the created fireball is schematically illustrated in Fig. 1.7 and was first observed in Pb-Pb collisions at SPS [16] and in Au-Au collisions at RHIC [17]. The elliptic flow is sensitive to the evolution of early stage and freeze-out conditions. Fig. 1.8 depicts the variation of v_2 with collision energy. The energy dependence of v_2 from RHIC to LHC energies shows an increasing trend, suggesting that a hotter and longer partonic phase is created at LHC energies. The thermodynamic transport properties of the system are studied from it. The hydrodynamic calculations predict a lower value of shear viscosity to entropy density ratio, which indicates that a strongly interacting fluid like plasma is created in heavy-ion collisions [18, 19, 20, 21, 22].

The information regarding the transport coefficient of the medium and fluctuations in the initial-state can be obtained by measuring the various Fourier flow coefficients. The anisotropic flow has also been measured in small systems in recent years [24]. However, recent studies do not provide any definitive conclusions concerning the collective behaviour in small systems.

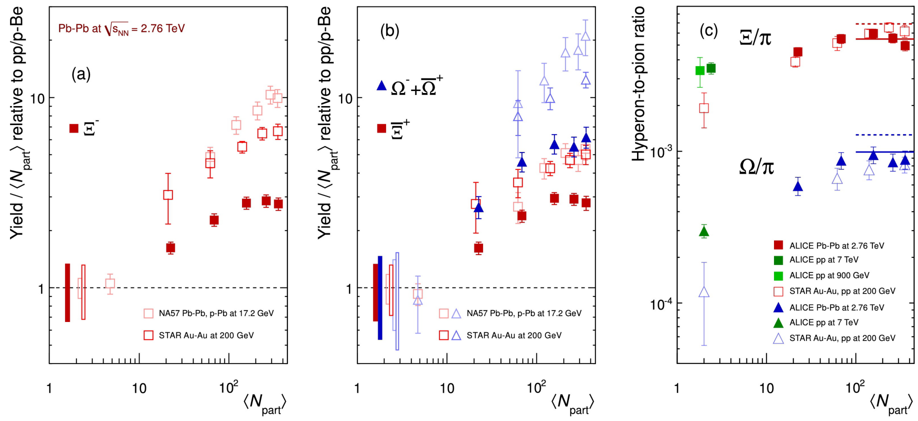

Figure 1.9: The enhancement of the multi-strange particles as a function of the mean number of participants shown for ALICE (full symbols), RHIC and SPS (open symbols) data [25].

1.4.2 Strangeness Enhancement

The enhanced production of strange particles was proposed as a signal of QGP formation by Rafelski and Muller [27]. The strange particles are predominately observed in high p_{T} region due to their production from processes like flavour excitation and flavour creation, which are hard scattering processes. The yield of strange and multi-strange hadrons has been predicted to be enhanced in nucleus-nucleus collisions as compared to the hadronic scenario [25]. Fig. 1.9 depicts the enhancement of various strange particles in Pb-Pb collisions at the LHC. The strangeness enhancement is defined as the ratio of the yield of a strange or multi-strange particle relative to a non strange particle. Enhancement of strangeness production in central heavy-ion collisions with respect to pp system [28] has been observed at RHIC. Statistical thermal models which assume a grand canonical ensemble approach, successfully describe the enhancement observed in heavy-ion collisions. The enhancement increases with an increase in the strangeness content of hadrons. The enhanced production of strange particles has also been observed in high multiplicity pp collisions at the LHC [26]. Fig. 1.10 indicates that the integrated yield of strange and multi-strange hadrons, relative to that of pions, increases significantly with charged particle multiplicity. The multiplicity dependence of strangeness production is similar in pp and p-Pb system and follows the trend observed in central Pb-Pb collisions.

1.4.3 Correlations and Fluctuations

Correlations and fluctuations of global observables such as transverse momentum and multiplicity etc, are believed to be sensitive to the phase transition and can provide information about different stages of heavy-ion collisions [29]. There are several types

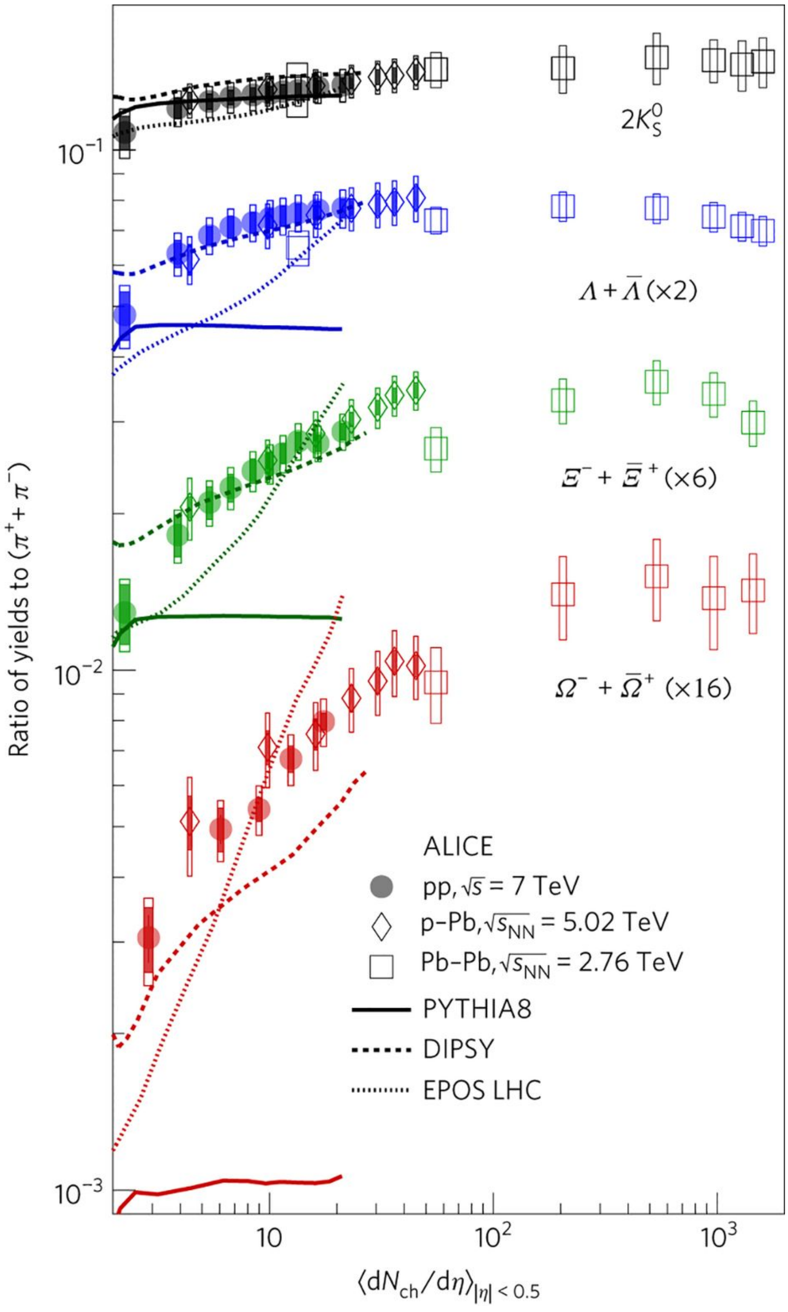

Figure 1.10: The ratio of strange baryon to pion yield as a function of charged particle multiplicity production in pp, p-Pb and Pb-Pb collisions at the LHC, compared with predictions from various models [26].

of fluctuations. There can be quantum fluctuations which arise if an observable does not commute with the Hamiltonian of the system. The response of the system can give rise to dynamical fluctuations. The dynamical fluctuations of interest include event-by-event measurements of multiplicity fluctuations, mean p_T fluctuations, particle yield ratio fluctuations, and fluctuations of conserved quantities like net-charge, net-baryon [29]. Finally, there are statistical fluctuations that are an inherent feature of stochastic processes.

1.5 Chiral Symmetry in QCD

Chiral symmetry is a global symmetry of the Strong interaction occurring in the limit of vanishing quark masses. The mass of quarks is finite but small compared to the hadronic scale. The masses of the lightest quarks -up and down are very small. Chiral symmetry can be considered as an approximate symmetry of Strong interactions. The existence of chiral symmetry was first inferred in nuclear beta decay. There are two types of currents associated with chiral symmetry, vector current and axial current. The underlying symmetry associated with vector current is the well known isospin symmetry of the Strong interaction and hence the hadronic vector current is identified as isospin current. The identification of axial current is not so straight forward because the symmetry associated with it is spontaneously broken. The spontaneous breaking of chiral symmetry leads to the formation of massless Goldstone-boson i.e, pions. If chiral symmetry was a perfect symmetry, the pions would be massless. However, the chiral symmetry is only approximate which causes the pion to have a finite but smaller mass compared to other hadrons [30].

It is predicted that at very high temperatures and energy densities, chiral symmetry can be restored. The restoration and breaking of chiral symmetry can be explored by considering the Lagrangian of two flavours of massless fermions given by,

$$\mathcal{L} = i\bar{\psi}_j \partial\!\!\!/ \psi_j, \tag{1.7}$$

where j refers to two different flavours, known as up and down, and $\partial\!\!\!/ = \partial_\mu \gamma^\mu$. The vector transformation, Λ_V, transforms the state as,

$$\Lambda_V : \psi \to e^{-i\frac{\vec{\tau}}{2}\vec{\Theta}}\psi \simeq \left(1 - i\frac{\vec{\tau}}{2}\vec{\Theta}\right)\psi, \tag{1.8}$$

where $\vec{\tau}$ refers to the Pauli - spin matrices. The conjugate field can be transformed as,

$$\bar{\psi} \to e^{i\frac{\vec{\tau}}{2}\vec{\Theta}}\bar{\psi} \simeq \left(1 + i\frac{\vec{\tau}}{2}\vec{\Theta}\right)\bar{\psi}. \tag{1.9}$$

These expressions of state and its conjugate in the equation of the Lagrangian results in,

$$i\bar{\psi}\partial\!\!\!/\psi = i\bar{\psi}\partial\!\!\!/\psi. \tag{1.10}$$

The Lagrangian is invariant under vector transformation. The effect of axial vector transformation on the Lagrangian can be seen by considering,

$$\Lambda_A : \psi \rightarrow e^{-i\gamma_5 \frac{\vec{\tau}}{2}\vec{\Theta}}\psi \simeq \left(1 - i\gamma_5 \frac{\vec{\tau}}{2}\vec{\Theta}\right)\psi, \tag{1.11}$$

and the conjugate state is,

$$\bar{\psi} \rightarrow e^{i\gamma_5 \frac{\vec{\tau}}{2}\vec{\Theta}}\bar{\psi} \simeq \left(1 - i\gamma_5 \frac{\vec{\tau}}{2}\vec{\Theta}\right)\bar{\psi}. \tag{1.12}$$

In this expression, anti-commutation relation of γ matrices are used, specifically, $\gamma_0\gamma_5 = -\gamma_5\gamma_0$. Under axial transformation, the Lagrangian becomes

$$i\bar{\psi}\partial\!\!\!/\psi \rightarrow i\bar{\psi}\partial\!\!\!/\psi - i\vec{\Theta}\left(\bar{\psi}i\partial_\mu\gamma^\mu\gamma_5\frac{\vec{\tau}}{2}\psi + \bar{\psi}\gamma_5\frac{\vec{\tau}}{2}i\partial_\mu\gamma^\mu\psi\right) = i\bar{\psi}\partial\!\!\!/\psi. \tag{1.13}$$

The second term vanishes because γ_μ anti-commutes with γ_5. The Lagrangian of massless fermions and hence massless QCD, under vector and axial-vector transformation is invariant. This symmetry is known as chiral symmetry of QCD. In group structure notation, it is denoted as $SU(2)_V \times SU(2)_A$. Λ_V exhibits invariance of the mass term while Λ_A does not. Thus Λ_A is not a good symmetry if quarks have finite mass but can be considered as an approximate symmetry as long as quark masses are small.

The mesons and baryons have definite properties under axial-vector and vector transformations which depend on their spin and parity. The combination of quark fields that carry relevant quantum numbers of the mesons are given by,

pion-like state : $\vec{\pi} \equiv i\bar{\psi}\vec{\tau}\gamma_5\psi$; sigma-like state : $\sigma \equiv \bar{\psi}\psi$

rho-like state : $\vec{\rho}_\mu \equiv \bar{\psi}\vec{\tau}\gamma_\mu\psi$; a_1 − like state : $\vec{a}_{1\mu} \equiv \bar{\psi}\vec{\tau}\gamma_\mu\gamma_5\psi$

Under vector transformation, the pion-like state transforms to another pion-like state and sigma-like state transforms into itself as,

$$\vec{\pi} \rightarrow \vec{\pi} + \vec{\Theta} \times \vec{\pi} \tag{1.14}$$

$$\sigma \rightarrow \sigma \tag{1.15}$$

Under axial transformation, pion and sigma-meson are rotated into each other as,

$$\vec{\pi} \rightarrow \vec{\pi} + \vec{\Theta}\sigma \tag{1.16}$$

$$\sigma \rightarrow \sigma - \vec{\Theta}\vec{\pi} \tag{1.17}$$

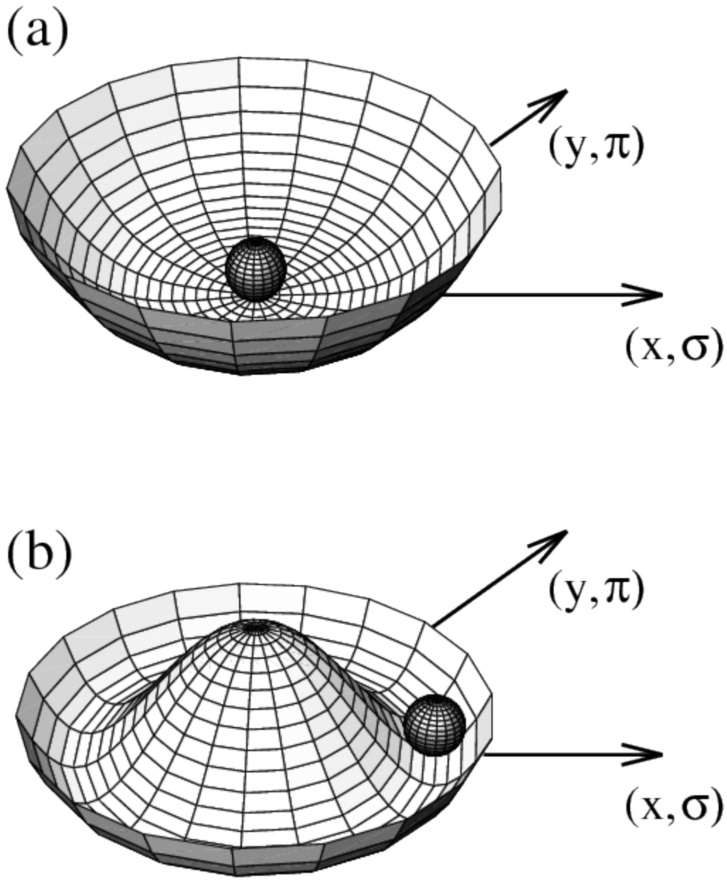

Figure 1.11: (a) No spontaneous breaking of chiral symmetry. (b) Spontaneous breaking of chiral symmetry [30].

1.5.1 Spontaneous Chiral Symmetry Breaking

The massless QCD Lagrangian is invariant under vector and axial transformations of the quark fields. The chiral symmetry is spontaneously broken due to inclusion of finite quark masses. Let two potentials which are rotationally invariant be considered as shown in Fig. 1.11(a), where the ground state of the potential is in the middle and invariant under rotation. In Fig. 1.11(b), the ground state is at a certain distance from the centre. The center in this figure is at local maxima and hence unstable which breaks the rotational symmetry. The same analogy can be applied to understand the breaking of axial-vector symmetry in Strong interactions. The effective QCD potential at zero temperature has a form similar to that depicted in Fig. 1.11(b) with the (x,y)- coordinates replaced by (σ,$\vec{\pi}$)-

fields. The sigma-field carries the quantum numbers of the vacuum and thus has a finite expectation value. The quark condensate has a finite value i.e, $< q\bar{q} >\neq 0$. In this case, the mass of pions vanish.

If the effective potential of QCD at very high temperature and density has a form similar to that depicted in Fig. 1.11(a), the system is in stable equilibrium position. In this case, quark condensate melts away, resulting in a system where chiral symmetry is restored.

1.6 Event-by-Event Fluctuations of Charged and Neutral Particle Multiplicity

In ultra-relativistic heavy-ion collisions at Large Hadron Collider (LHC), a deconfined state of matter is created at very high temperature and high energy densities. This matter expands and cools through the critical temperature thereby forming hadrons. Within the hot and dense plasma of quarks and gluons, equilibrium regions are produced, where the chiral symmetry is nearly restored. The restoration of chiral symmetry and its subsequent relaxation towards the normal vacuum is additionally posited to yield transient regions where the value of the chiral order parameter differs from that of the surrounding medium. These regions are called Disoriented Chiral Condensates (DCC) [31, 32, 33] and their decays are expected to produce large event-by-event fluctuations in neutral-to-charge particles. The formation of DCCs and their decays can be understood from the potential of linear sigma model at finite temperature, T given by,

$$V_{eff} = \frac{\lambda}{4}(\sigma^2 + \vec{\pi}^2)^2 - \frac{\lambda(\sigma^2 + \vec{\pi}^2)}{2}\left(f_\pi^2 - \frac{m_\pi^2}{\lambda} - \frac{T^2}{2}\right) - f_\pi m_\pi^2 \sigma. \tag{1.18}$$

Fig. 1.12 shows the shape of the effective potential of linear sigma model for spontaneous breaking of chiral symmetry. The last term of Eq. 1.18 leads to explicit symmetry breaking, which lifts the degeneracy of the vacuum present at unstable equilibrium position. The field is unstable and hence moves towards the stable equilibrium position and oscillates. A chiral condensate is produced when the chiral symmetry breaks and is characterised by a non vanishing order parameter given by, $< \sigma > \sim < \bar{u}u + \bar{d}d >$. When the field moves from a higher potential to lower potential, it emits pions of different isospins. In a generic particle production scenario, because of isospin conservation in the Strong interaction, the production of π^+, π^-, and π^0 are equally probable. The neutral pion fraction is defined as:

$$f_\pi = \frac{n_{\pi^0}}{n_{\pi^0} + n_{\pi^\pm}}, \tag{1.19}$$

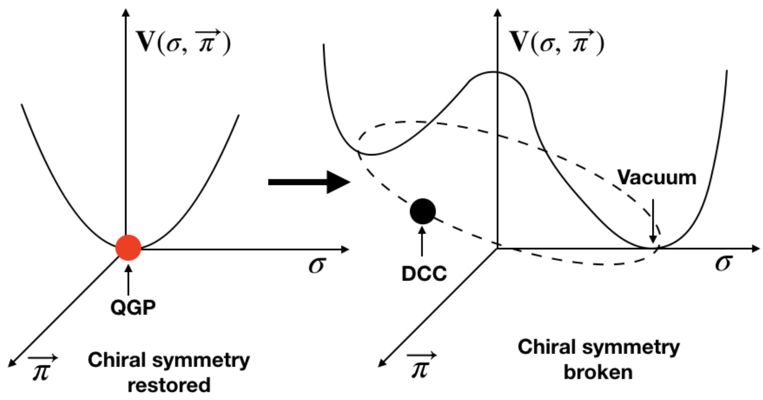

Figure 1.12: Effective potential of linear sigma model, which indicates the transition of a chiral symmetric restoration phase to a chiral symmetry broken phase.

where n_{π^0} is the number of total neutral pions and $n_{\pi^\pm}$ is the number of total charged pions. The generic particle production leads to a binomial distribution of the neutral pion fraction with a mean of 1/3. i.e, $< f_\pi >= 1/3$. If a DCC is formed, then the chiral field is misaligned with respect to the true vacuum. As the DCC tries to realign with the true vacuum, it radiates pions. The probability distribution of the neutral pion fraction produced by the decay of DCC domains is very different from that of a generic case and is given by [33],

$$P(f_\pi) = \frac{1}{2\sqrt{f_\pi}}, \qquad 0 < f_\pi \leq 1. \tag{1.20}$$

The distribution can be derived by expressing f_π in terms of Cartesian pion fields:

$$f_\pi = \frac{\pi_z^2}{\pi_x^2 + \pi_y^2 + \pi_z^2}, \tag{1.21}$$

and parametrizing the field in Spherical coordinates as:

$$(\sigma, \pi_z, \pi_x, \pi_y) = (cos\theta, sin\theta cos\phi, sin\theta sin\phi cos\eta, sin\theta sin\phi sin\eta), \tag{1.22}$$

gives,

$$f_\pi = cos^2\phi. \tag{1.23}$$

The distribution of $p(f_\pi)$ can be expressed as,

$$p(f_\pi) = \int_\pi^f P(f')df' = \frac{1}{\pi^2}\int_0^{2\pi} d\eta \int_0^\pi d\theta sin^2\theta \int^{arccos\sqrt{f_\pi}} d\phi sin\phi = \sqrt{f_\pi} + c. \tag{1.24}$$

This yields

$$P(f_\pi) = \frac{dp}{df_\pi} = \frac{1}{2\sqrt{f_\pi}}. \tag{1.25}$$

A similar analogy can be explored with SU(3) symmetry where the chiral condensate characterized by up-down-strange symmetric field is given by, $< \sigma > \sim < cos\theta(\bar{u}u + \bar{d}d) + sin\theta(\bar{s}s) >$. The normal kaon production would lead to a binomial distribution of the neutral kaon fraction, f_K $(= (n_{K^0} + n_{\bar{K}^0})/(n_{K^0} + n_{\bar{K}^0} + n_{K^\pm}))$ with a mean of 1/2. Here, $n_{K^0} + n_{\bar{K}^0}$ corresponds to the total number of neutral kaons and $n_{K^\pm}$ corresponds to the total number of charged kaons. On the other hand, production of kaons from DCC regions would lead to a probability distribution of $P(f_k)$ given by [34],

$$P(f_k) = 1, \qquad 0 \leq f_k \leq 1. \tag{1.26}$$

This can be obtained by considering four-dimensional sub-space of the kaon field i.e, the direction of kaon field vector,

$$\vec{k} = (\cos\phi_k \sin\upsilon_k \sin\psi_k, \sin\phi_k \sin\upsilon_k \sin\psi_k, \cos\upsilon_k \sin\psi_k, \cos\psi_k). \tag{1.27}$$

The kaon fraction is,

$$f_k = 1 - sin^2\upsilon_k sin^2\psi_k. \tag{1.28}$$

The distribution is given by,

$$P(f_k) = \frac{1}{2\pi^2}\int_0^\pi d\psi_k sin^2\psi_k \int_0^\pi d\upsilon_k \sin\upsilon_k \times \int_0^{2\pi} d\phi_k \delta(f_k - 1 + \sin^2\upsilon_k \sin^2\psi_k) \tag{1.29}$$

$$= \frac{1}{\pi}\int_0^\pi d\psi_k \sin\psi_k \theta(f_k - \cos^2\psi_k) \times [f_k - \cos^2\psi_k]^{-1/2} \tag{1.30}$$

$$= \frac{2}{\pi}\int_0^{\sqrt{f_k}} d\cos\psi_k [f_k - \cos^2\psi_k]^{-1/2} \tag{1.31}$$

$$= 1. \tag{1.32}$$

According to theoretical predictions, the mean momentum of such kaons is inversely proportional to the size of the DCC domains [35] and kaons from DCC regions were expected to be produced at modest transverse momentum [36]. The role of DCC has additionally been utilised to explain the enhanced yield of Ω (and $\bar{\Omega}$) baryons observed in 17 A GeV Pb-Pb collisions measured at the CERN SPS [38]. The observed enhancement was attributed to topological defects resulting from the production of DCC regions. In this context, the evolution of distinct DCC domains might affect the strange particle production and thus can lead to fluctuations of the relative yields of neutral and charged kaons [36]. These fluctuations can be measured by calculating $\nu_{dyn}[K_0, K^\pm]$ [36]. Specifically, it was predicted that the production of DCC domains in central nucleus-nucleus collisions might lead to an anomalous scaling of ν_{dyn} with collision centrality. At low beam energies, the linear sigma model simulation indicates that pion fluctuations dominate three flavour

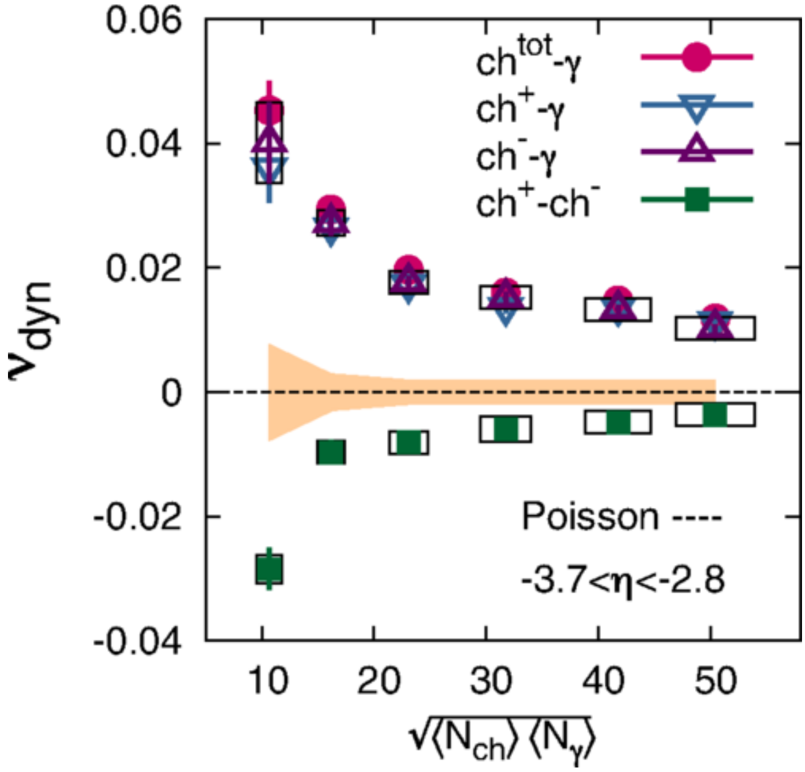

Figure 1.13: The centrality dependence of ν_{dyn} for different combinations of γ - ch and ch^{+} - ch^{-} [37].

DCC, as the fraction of energy imparted to kaon fluctuations is relatively small owing to its larger mass. However, at LHC energies, the strange quark mass can be neglected compared to the total energy available towards particle production, which can lead to up-down-strange symmetric chiral condensate. A search of kaon (pion) isospin fluctuations at LHC energies is thus of significant interest even though past searches in the pion sector have yielded no evidence of DCC production [37].

Fig. 1.13 shows the STAR [37] measurement of the correlation between neutral and charged pions. It shows that the variation of ν_{dyn} with multiplicity, has an approximate $1/\sqrt{\langle N_{ch}\rangle\langle N_{\gamma}\rangle}$ behaviour. The values of ν_{dyn} for the combinations of photons and total charged particles are very close to that of the values of ν_{dyn} for photons and individual (positive and negative) charges. The values of ν_{dyn} for the combination of positively and negatively charged particles are different in sign and magnitude compared to those of total charged particle and photon correlation. The ν_{dyn} value is negative for oppositely charged particles due to the dominance of the large correlation term arising from pairs of oppositely charged particles produced from the decay of neutral resonances. A previous study of ν_{dyn} in kaon sector [39] suggested that ν_{dyn} is sensitive to the collision centrality. It was observed that, ν_{dyn} changes sign with the variation of the percentage of DCC in the events

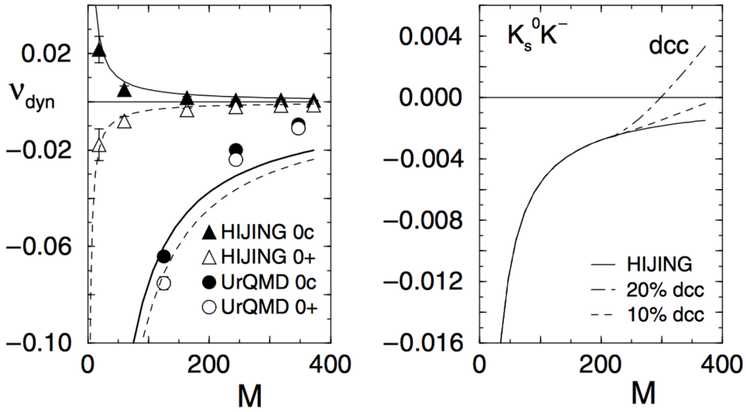

Figure 1.14: (**Left Panel**): ν_{dyn} of $K_s^0K^{\pm}$ and $K_s^0K^{+}$ are compared to solid and dashed curves computed using a wounded nucleon model normalized to pp simulations. (**Right Panel**): DCC was implemented in HIJING events [39].

as illustrated in Fig. 1.14. Therefore, the measurement of $\nu_{dyn}[K_s^0, K^{\pm}]$ with centrality at LHC energies would shed light on the mechanism of the correlated production of strange particles in high energy heavy-ion collisions. The event-by-event fluctuations of $K^{\pm}$s and K_s^0s are measured in Pb-Pb collisions at $\sqrt{s_{\rm NN}}$ = 2.76 TeV.

1.7 Organisation of Thesis

The thesis reports the measurement of the event-by-event fluctuations of the charged and neutral kaons in Pb-Pb collisions at $\sqrt{s_{\rm NN}}$ = 2.76 TeV with the ALICE detector at the LHC. The measurement is performed by calculating the statistical observable $\nu_{dyn}[K_s^0, K^{\pm}]$ for different centrality classes. Chapter 2 presents an overview of ALICE experiment at the LHC. It gives a brief description of different sub-detectors of ALICE together with the information about data handling in ALICE. A toy model simulation to study the sensitivity of ν_{dyn} to the presence of DCC like events is discussed in Chapter 3. Chapter 4 presents the details of data analysis and methodology used to measure event-by-event fluctuations in neutral and charged kaons. Chapter 5 discusses the different phenomenological approaches to study particle production mechanism in high energy hadronic and heavy-ion collisions. Chapter 6 summarises the various investigations carried out in this thesis.

Chapter 2

The ALICE Experiment at the LHC

2.1 The Accelerators

Scientific theories need experimental verification. Huge accelerators are used to obtain the experimental dataset in high energy physics which are systematically analysed to obtain the results and compare them to existing theoretical predictions. The accelerators are huge machines that accelerate charged particles at relativistic energies and allow them to collide with other particles.

2.1.1 The Large Hadron Collider

The Large Hadron Collider [40] (LHC) is the largest accelerator in the world having a circumference of 27 kms, located at CERN, Geneva. It uses the tunnel previously used by the Large Electron-Positron (LEP) collider. The collider was chosen for construction underground at a depth of 100 meters, which provides a good shielding against radiation (provided by earth's crust). There are two beam pipes inside the tunnel which are kept at ultra high vacuum and are surrounded by superconducting electromagnets. The electromagnets are kept at a supercooled temperature of around -271.3 C (1.9 K). Two separate high energy particle beams travel at nearly the speed of light before the collision, inside these beam pipes. A total of 1232 dipole magnets of length 15 metres each are used to bend the beams and 392 quadrupole magnets of length 5-7 metres each, are used to focus the beams. The schematic diagram of the LHC ring and CERN accelerator complex is shown in Fig 2.1. The beams in the LHC ring collide at four main interaction points. At each interaction point, detectors are set up to record the collision data in accordance with the physics goal at that point. A Toroidal LHC ApparatuS (ATLAS) and Compact Muon Solenoid (CMS) are the high luminosity experiments, which are situated diametrically opposite in LHC ring at Point 1 and Point 5, respectively. They are designed to address

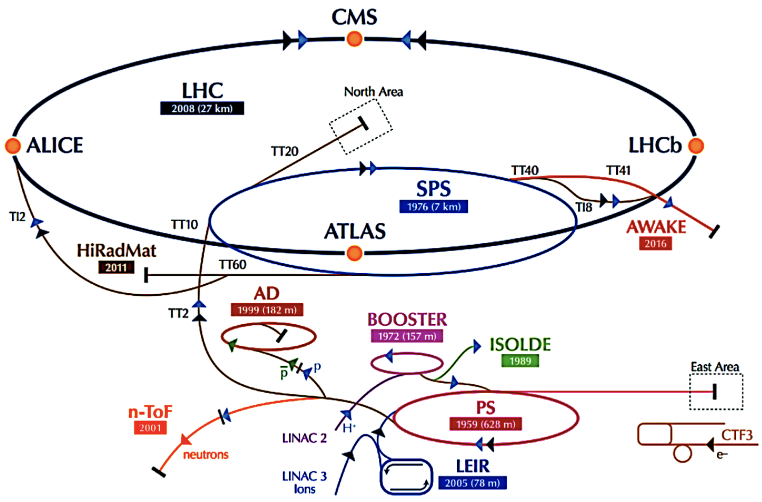

Figure 2.1: The schematic diagram of LHC ring at CERN's accelerator complex [41].

the physics of pp collisions like standard model particles, super symmetry, physics of particles that can explain dark matter and extra dimensions. The heavy-ion collision data is also analysed by these experiments to address the physics of heavy-ion collisions. The Large Hadron Collider beauty (LHCb) experiment at point 8 is designed to investigate matter and antimatter anomaly of the universe by studying the "beauty quark". A Large Ion Collider Experiment (ALICE) detector located at point 2 is designed to study the physics of a deconfined state of matter produced in heavy-ion collisions. The purpose and design of the detector are described in detail in section 2.2.

2.1.2 Proton Acceleration

The hydrogen atoms obtained from the hydrogen gas cylinder are fed at a precisely controlled rate to the source chamber of the Linear Accelerator (LINAC 2), where electrons are stripped away from the hydrogen atoms to get protons. The proton beams are accelerated by an electric field and then injected at nearly 1/3rd of the speed of light to a BOOSTER of circumference 157 metres. The BOOSTER accelerates the proton beams up to 91.6% of the speed of light and injects the beam into Proton Synchrotron (PS) of circumference 628 metres. The proton beams inside the PS are further accelerated to 99.9% of the speed of light. At this point, the speed of the protons cannot be further increased by the pulsating electric field, instead the added energy manifests itself as an increase in the mass of protons. In PS ring, protons are accelerated up to 25 GeV and then injected into Super Proton Synchrotron (SPS), a huge ring of circumference 7 kms where the proton beams are accelerated up to 450 GeV. Finally, the proton beams are energised sufficiently to be launched into the orbit of the Large Hadron Collider ring, where they are further accelerated to 99.9999996% of the speed of light. The beams circulate clockwise in one beam pipe and anticlockwise in another. The beams collide at four interaction points equipped with suitable detectors. There are 2808 bunches of protons with a bunch spacing of 25 ns which provide a nominal luminosity of $10^{34} cm^{-2} s^{-1}$ [40].

2.1.3 Heavy-Ion (Pb) Acceleration

The injection of Pb-ions inside the LHC ring involves complex processes. It starts with the heating of a 2 cm long and 500 mg of a pure lead piece at about 550°C to form lead atom vapour. An electric current is passed to rip the electrons from the lead atom to form lead ions. The lead ions are then transferred to a linear accelerator called LINAC 3 with an energy of 4.5 MeV per nucleon. The ions are passed through carbon foil which further strips the ions to make it Pb^{54+}. Next, the Pb^{54+} are injected into the Low Energy Ion Ring (LEIR) where they are accelerated up to 72 MeV per nucleon. The beams are injected into the PS by two pulsed bumper magnets, where the final stripping of electrons is achieved by the aluminium foil to make Pb^{82+}. These ions are further accelerated to 5.9 GeV per nucleon followed by their injection to SPS. The SPS accelerates the beams to 177 GeV per nucleon and finally injects them in two directions into the LHC ring. During the Pb-ion collisions, 600 bunches each of 7×10^7 lead ions are filled in LHC ring to provide designed luminosity of $10^{27} cm^{-2} s^{-1}$ [40].

2.2 A Large Ion Collider Experiment (ALICE)

ALICE [42, 43] is one of the important detectors at the LHC designed to study the physics of heavy-ion collisions. It has obtained data in pp, p-Pb, Pb-Pb, and Xe-Xe collisions at the LHC energy. It is a 10,000-tonnes detector of length 26 meters, height 16 meters and width 16 meters. It consists of 18 sub-detectors, which are assembled in the central barrel part and in the forward region. It has excellent tracking and particle identification ability over a wide range of momenta. Fig 2.2 presents a schematic layout of the various sub-detector systems in ALICE. It is made up of the following basic elements.

- **Magnet:** Most of the ALICE detectors are housed inside a large solenoidal magnet designed to provide a 0.5 T field.

- **Vertex detector:** It provides the vertex position of the primary particles with a precision of a tenth of millimetre. It also locates the position of the disintegration of the short lived particles containing heavy quarks.

- **Tracking chamber:** The image of the particle trajectories are obtained.

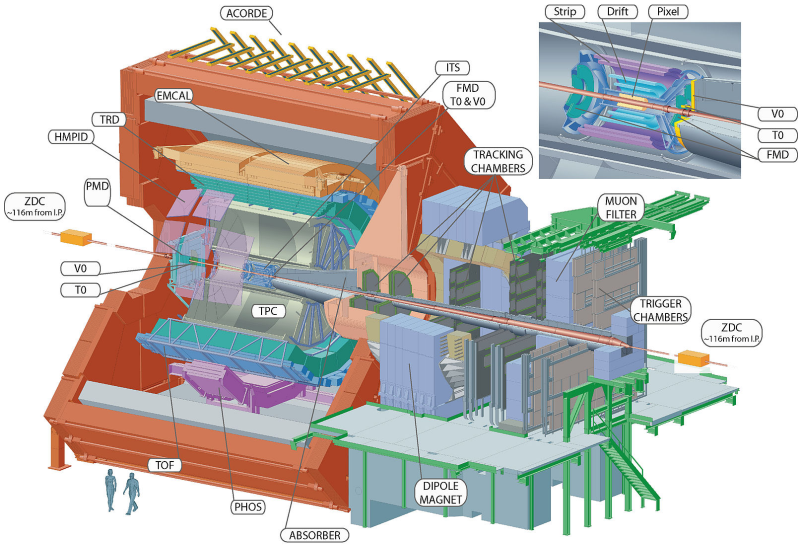

Figure 2.2: The schematic view of the ALICE sub-detectors [42].

- **Calorimeter:** It measures the EM energy of electrons and photons produced by collisions. It also measures a fraction of the energy of charged hadrons.

- **Muon spectrometer:** The muons interact with matter very rarely and thus are difficult to identify. The spectrometer is shielded with a material absorber, which absorbs all other particles except muons. This helps to study the open heavy flavour production and quarkonia production at LHC energies in pp, p-A, and nucleus-nucleus collisions, via the muonic channel.

- **Trigger:** These detectors are used to determine the quality of the events and help to isolate the rare and interesting events.

The central barrel tracker covers the polar angles from 45° to 135 ° corresponding to the pseudo-rapidity range from -0.9 to 0.9. The components of tracker include the Inner Tracking System (ITS), a cylindrical Time Projection Chamber (TPC), three particle identification arrays of Time of Flight (TOF), a ring Imaging Cherenkov (HMPID) and Transition Radiation detectors (TRD), as well as two electromagnetic calorimeters (PHOS and EMCAL). All these detectors cover the full azimuth except HMPID, PHOS, and EMCAL detectors.

2.2.1 Inner Tracking System (ITS)

The ITS [44] detector is comprised of six cylindrical layers formed by 3 groups of silicon detectors. Due to large particle density in heavy-ion collisions at LHC, Silicon Pixel detectors (SPD) have been considered for the inner two layers. Silicon micro-Strip

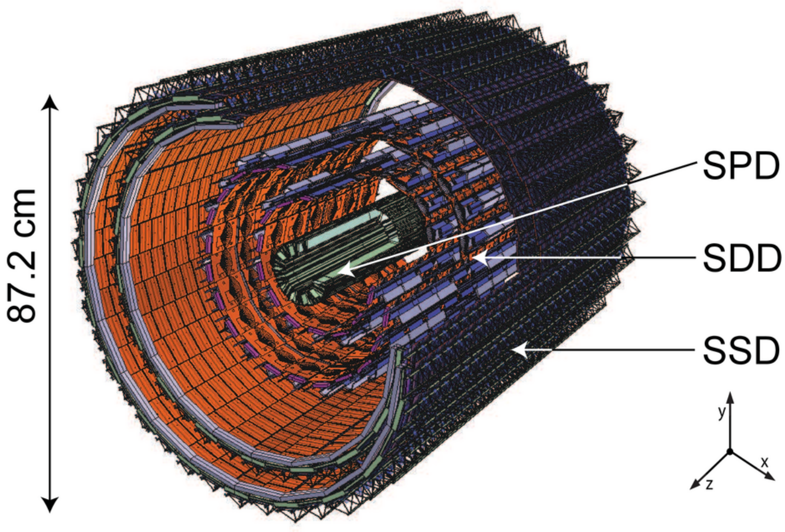

Figure 2.3: The schematic view of the ITS detector around LHC beam pipe [45].

Detectors (SSD) are used at the two outermost layers and Silicon Drift Detectors (SDD) are used in the two middle layers. It has a pseudorapidity coverage of $|\eta| < 0.9$ and covers full azimuthal acceptance. It locates the vertex position of the primary particles and reconstructs the vertex position of secondary particles from their decay. The momentum and angle resolution of the particles reconstructed within TPC are improved by this detector and it reconstructs particles passing through dead regions of the TPC. The detector also recovers particles that do not reach or miss the external detectors due to limited acceptance or momentum cut-off. Fig 2.3 depicts the schematic view of the ITS detector around the LHC beam pipe.

When particles pass through the ITS detector, the energy loss distribution (dE/dx) of those particles is measured by the four outer layers of the detector. The measurement of the cluster charge provides the dE/dx value for each layer of the detector. The value of dE/dx is calculated for each track by measuring the truncated mean of the energy loss measured in each pad row. Fig 2.4 shows the truncated mean energy loss distribution as a function of momentum in the ITS detector.

2.2.2 Time Projection Chamber (TPC)

The TPC [46] is used mainly as a tracking detector in the central barrel. It is also used for particle identification, vertex determination and charged-particle momentum measurement with good two-track separation. The vector meson resonance particles are studied using TPC along with ITS and TRD. It has full azimuthal acceptance except for the dead zone and it covers a pseudo-rapidity range of $|\eta| < 0.9$. The inner and outer

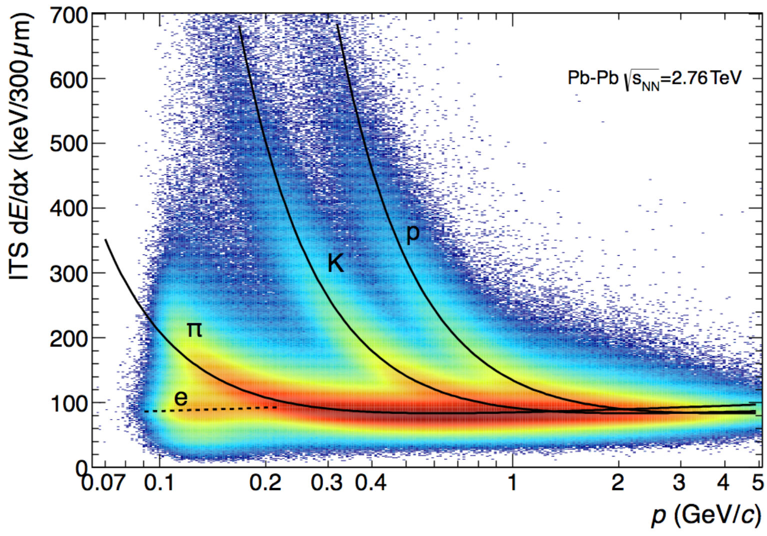

Figure 2.4: The energy loss distribution as a function of momentum in ITS. Both the energy loss and the momentum were measured by the ITS detector [44].

radius of the cylindrical volume of TPC are about 85 cm and 250 cm, respectively and it has an overall length of 500 cm along the beam direction. Each end plate of TPC contains multi-wire proportional chambers (MWPC) with cathode pad readout. A schematic view of the TPC is shown in Fig 2.5.

The charged particles leave behind the footprints of their passage in the form of a long trace of ionized gas. During the process of ionization, the emitted electrons drift from the central electrode to the cathode pad readouts at each end plate of the cylinder. The signals are obtained through the avalanche phenomena in the vicinity of anode wires. The TPC volume is filled with a mixture of Ne (90%), CO_2 (10%), and N_2 (5%). The end plates of the cylinder consist of wire planes and 5,60,000 electronics channels, which provide information regarding the ionization density of the trace. The carbon fibres are chosen for low material budget and high mechanical stability. The charge and the momentum of the particles are obtained from the bending of the tracks.

The particles are identified by measuring their specific energy loss per unit length (dE/dx) distribution, charge and momentum simultaneously. The specific energy loss is parametrised in the form of Bethe-Bloch formula, originally proposed by the ALEPH collaboration [47] given by,

$$f(\beta\gamma) = \frac{P_1}{\beta^{P_4}}\left(P_2 - \beta^{P_4} - ln(P_3 + \frac{1}{(\beta\gamma)^{P_5}})\right), \tag{2.1}$$

where β refers to the particle velocity, γ refers to the Lorentz factor, and P_{1-5} are the fit parameters.

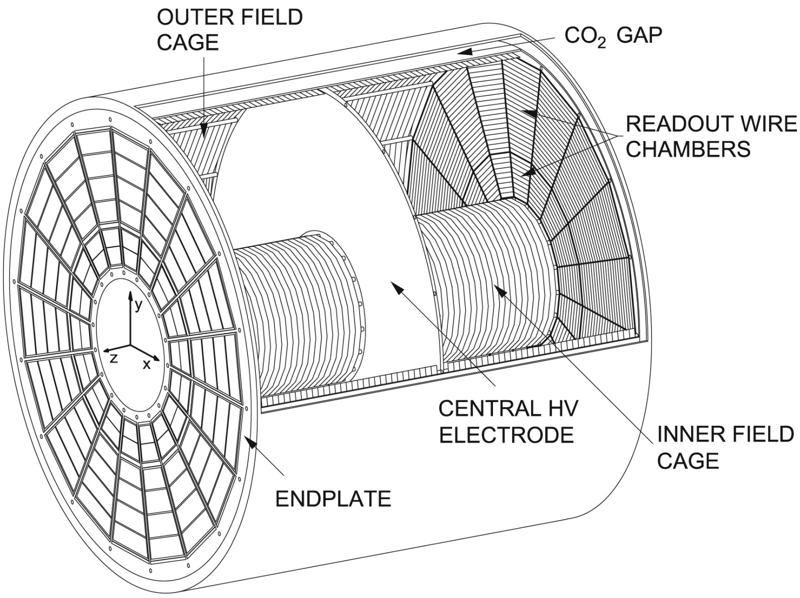

Figure 2.5: 3D view of the TPC field cage [46].

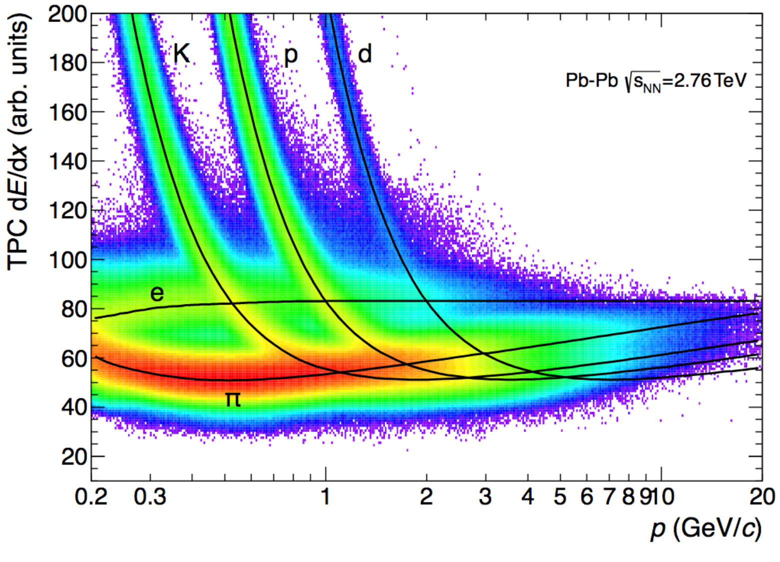

Figure 2.6: The energy loss per unit length in TPC as a function of track momentum in Pb-Pb collisions at $\sqrt{s_{NN}} = 2.76$ TeV [46].

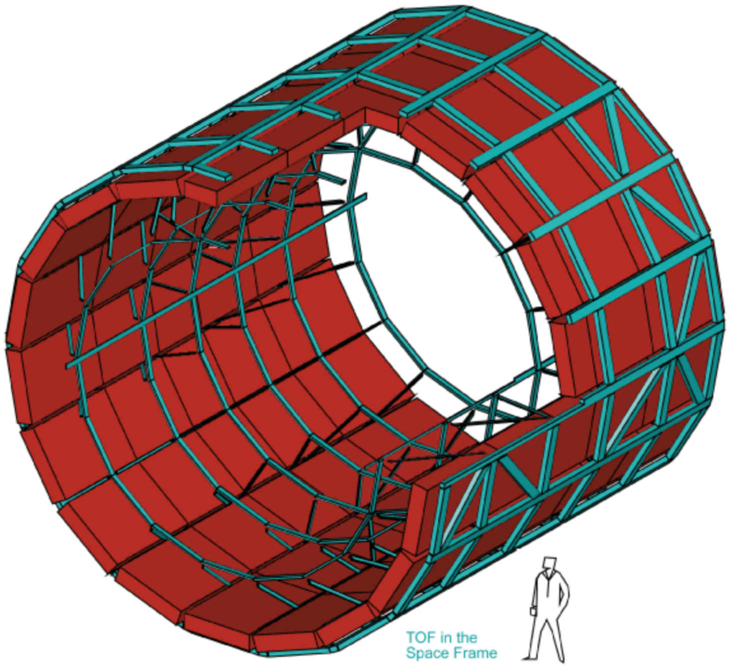

Figure 2.7: The schematic view of the TOF detector [48].

Fig 2.6 depicts the measured distribution of dE/dx with track momentum for TPC. The lines show parametrization of the expected energy loss (given by Bethe-Bloch approximation) for each particle.

2.2.3 Time of Flight (TOF)

TOF detector is used to measure the time of flight of the particles. The TOF detector is a cylindrical tube with having an inner and outer radius of 370 cm and 390 cm, respectively. It covers a pseudo-rapidity range of $|\eta| < 0.9$ and has full azimuthal coverage. Multi-gap Resistive-Plate Chamber (MRPC) technology is used in the TOF detector [48]. It is a 10-gap double-stack MRPC strip of length 122 cm and of width 13 cm. It has an active area of 120×7.4 cm^2, which is subdivided into two rows of 48 pads. The angle of these strips with respect to the axis of the cylinder increases from 0° in the central part of the detector to 45° in the extreme part of the module. The strips are enclosed in gas mixture of $C_2H_2F_4$ (90%), i-C_4H_{10} (5%) and SF_6 (5%). MRPC strips are connected with readout electronics. The ionization produced by charged particles initiates a gas avalanche, which produces a signal providing a stop time which is used to determine the time of flight of the particles. The pions and kaons are identified in the intermediate momentum range (2.5 GeV/c) and protons are identified up to 4 GeV/c. The mass of the

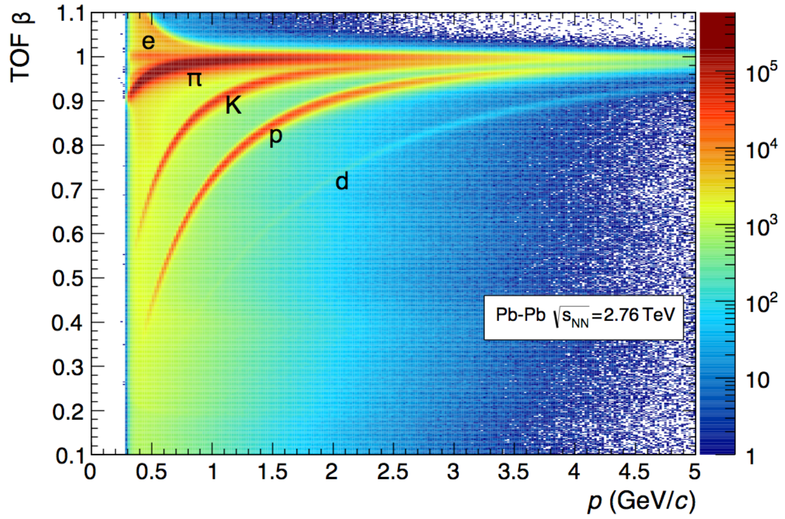

Figure 2.8: TOF β distribution as a function of track momentum in Pb-Pb collisions at $\sqrt{s_{NN}} = 2.76$ TeV [48].

charged particle can be obtained as,

$$m^2 = \frac{p^2}{c^2}\left(\frac{c^2t^2}{L^2} - 1\right), \tag{2.2}$$

where L represents trajectory length and t is the time of flight. When two charged particles of unequal masses, m_1 and m_2 move with different velocities, $v_1(\beta_1)$ and $v_2(\beta_2)$, and have energies E_1 and E_2, respectively, have same momentum and same track length, then the time of flight difference $t_1 - t_2$ can be expressed as,

$$t_1 - t_2 = L(\frac{1}{v_1} - \frac{1}{v_2}) \tag{2.3}$$

$$= \frac{L}{c}(\frac{1}{\beta_1} - \frac{1}{\beta_2}) \tag{2.4}$$

$$= \frac{L}{pc^2}(E_1 - E_2) \tag{2.5}$$

$$= \frac{L}{pc^2}\left(\sqrt{p^2c^2 + m_1^2c^4} - \sqrt{p^2c^2 + m_2^2c^4}\right). \tag{2.6}$$

For relativistic particles, E ~ pc >> mc^2. The time difference is given by,

$$t_1 - t_2 = \frac{Lc}{2}\left(\frac{m_1^2 - m_2^2}{p^2}\right). \tag{2.7}$$

Fig 2.8 illustrates the β distribution with track momentum (measured by TPC).

2.2.4 V0 Detector

V0 detector system is a small angle detector consisting of 32 scintillating counters in two arrays (V0A and V0C) [49]. The V0A is placed on the opposite side of the muon spectrometer at a distance of 330 cm away from the interaction point (IP) and the V0C is located 90 cm away from the IP on the front side of the hadronic absorber covering an η range of 2.8<η<5.1 and -3.7<η<-1.7, respectively. The main goal of the V0 detector is to provide Minimum Bias trigger and Centrality Trigger for pp and nucleus-nucleus collisions. The V0 amplitude is primarily used for the centrality estimator in ALICE.

2.2.5 T0 Detector

The main objectives of the T0 detectors [49] are to generate a timing signal which is independent of the vertex position for the TOF detector, to measure the vertex position of the interaction and provides L0 trigger, to provide a wake up signal to the TRD prior to the L0 trigger and to generate minimum bias and multiplicity triggers. The T0 detector consists of two arrays (T0-A and T0-C) of 12 Cherenkov counters. The T0-A is located at a distance 360 cm away from the IP and the T0-C is placed at a distance 70 cm away from the IP. A pseudo-rapidity range of $-3.28 \leq \eta \leq -2.97$ is covered by the T0-C and the T0-A covers the pseudo-rapidity range of $4.61 \leq \eta \leq 4.92$.

2.3 Trigger, Online and Offline Computing

It is crucial to store the data for physics analysis, which is performed by ALICE online system which consists of four subsystems: (i) Data Acquisition (DAQ), (ii) Central Trigger Processor (CTP), (iii) High Level Trigger (HLT) and (iv) Control Systems. Each subsystem is described briefly in the following sections.

2.3.1 Central Trigger Processor

CTP is designed to select a variety of events with different features satisfying the requirements of physics demand and conditions imposed by the DAQ and HLT [42, 50]. It is divided into two categories of trigger levels known as fast trigger and final level trigger (L2). The fast trigger consists of two levels: Level 0 (L0) and Level 1 (L1). L0 signal reaches detectors in 1.2 μs and receives all trigger inputs very fast. L1 signal is delivered after 6.5 μs and it picks up all the remaining fast inputs. A past-future protection circuit is used in ALICE to make events reconstructible. The final level trigger i.e, L2 trigger has to wait for the end of past-future protection interval (88 μs) to verify whether an event can be recorded or not. There are seven different types of 6U VME boards in CTP, which mediate the trigger signals housed in a single VME crate. There are 60 trigger inputs and 50 trigger classes for ALICE. It provides an interface between fast detector and DAQ to tag a physics event. Trigger inputs are provided by various trigger detectors. A trigger class is defined by some logical conditions and requires inputs from a set of detectors. It also records various types of data for its operations. It sends information about bunch crossing number, orbit number and trigger information in L2 accept (L2a) to detectors for each accepted event. It also checks the correct information on triggers at regular intervals. All trigger classes are grouped into two groups to avoid any loss of rare events: those corresponding to common processes and those corresponding to rare processes. All trigger classes are activated and can generate triggers at the initial stage. DAQ sends the signal to disable the common classes to make the bandwidth available for rare classes when temporary storage exceeds some predefined maximum limit. The common classes are again enabled by DAQ when the temporary storage has gone below the corresponding minimum limit.

2.3.2 Data AcQuisition

The DAQ [42, 50] is responsible to select desired physics events, to provide proper access to these events for the execution of high level trigger algorithms. It records the data into the data storage facility for later analysis. ALICE uses several triggers to collect data, which use a large fraction of total data acquisition bandwidth. The ALICE DAQ has to be really efficient to handle the demand for large data flow. Fig 2.9 displays the schematic diagram of the ALICE DAQ system. When the detector receives a signal from CTP through the Local Logical Unit (LTU), it immediately collects data. The Front-End Read-Out (FERO) electronics of detectors are interfaced with the ALICE-standard Detector Data Links (DDL). Local Data Concentrators (LDCs) receive event fragments via DDL and then assemble them logically into sub-events. LDC decides the destination of each sub-event. The availability of Global Data Collectors (GDCs) is informed by the Event-Destination Manager (EDM) to the LDCs. LDCs then send the sub-events to GDCs where the full event building is done with the appropriate trigger. The event building is managed by Event Building and Distribution System (EBDS) whose role is to synchronise all LDCs and their destination GDCs and it balances the loads on different GDCs. GDCs archive the data in Transient Data Storage once event building is done and after a fixed size of data is obtained. The files produced by GDCs are registered by AliEn and then TDS mover exports them to CERN Computing Center (CCC) to record them in Permanent Data Storage (PDS). DAQ communicates with its various elements via TCP/IP protocol. The software used for DAQ is Data Acquisition and Test Environment (DATE), which uses UNIX system tools and its configuration is realized with MySQL. Monitoring Of Online Data (MOOD) is used to check the quality and visualisation of data created by detectors. MOOD is interfaced with DATE and it handles online and offline data streams available

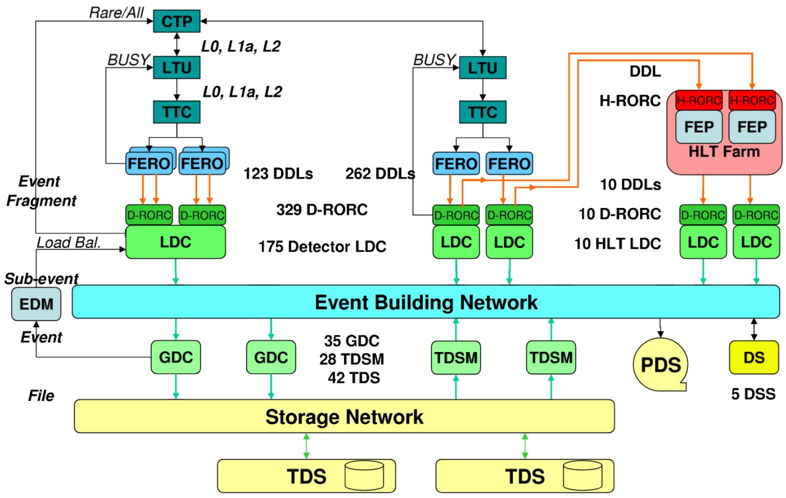

Figure 2.9: Schematic diagram of ALICE DAQ system and the interface to the HLT system [42].

on LDCs and on GDCs. DAQ framework has also Automatic Monitoring Environment (AMORE) to monitor the quality of the data by checking against some reference. If the collected plot does not meet the desired reference, it gives alarms on the operator screens and initiates automatic recovery actions.

2.3.3 High Level Trigger (HLT)

A single central nucleus-nucleus collision produces data of 75 MB and the data rate after all detectors information and trigger selection, becomes 25 GB/s. The physics content is very small and the DAQ archiving rate is 1 GB/s. Therefore, HLT [42, 50] does online processing of events to compress the data volume. Based on detailed online analysis, HLT accepts or rejects events. It selects the region of interest within an event by performing a partial readout. This is followed by application of compression algorithms on the accepted and selected events to reduce the event size without losing any physics information. HLT has six layers of architecture which are shown in Fig 2.10. All detectors are connected with HLT by 454 Detector Data Links (DDLs) in ALICE. Raw data is collected via these DDLs at layer 1. The basic calibration, hit and clusters information extraction are done in layer 2. Individual event reconstructions for each detector are done in the third layer. Assembling of all calibrated information of detectors and full event building is done in layer 4. In layer 5, selections of events or region of interest are done based on the run specific physics selection criteria. The data compression is done in the sixth layer. To perform the online analysis of events, HLT needs huge computing resources. It has a PC farm (located in the counting room in ALICE at Point2) of up

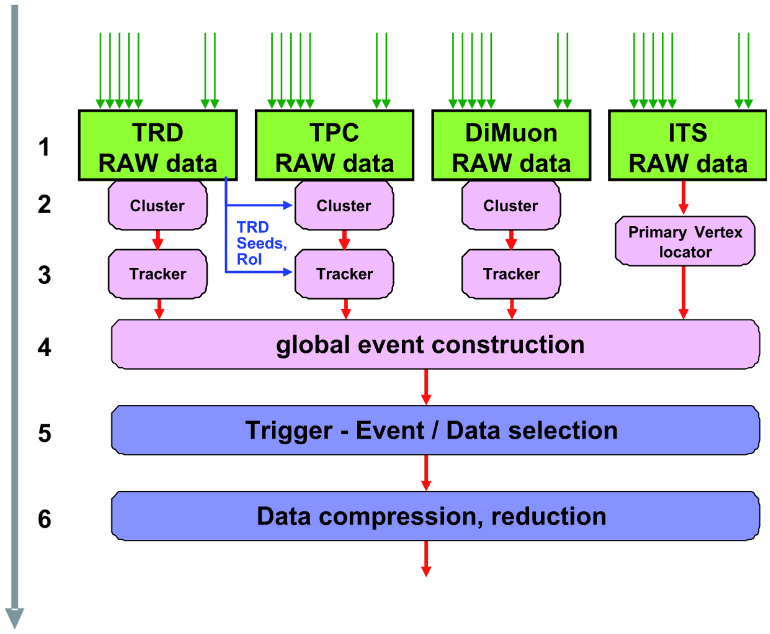

Figure 2.10: The six architectural layers of HLT [42].

to 1000 multi-processor computers running in parallel on the nodes of the computing cluster. In order to minimize inter-nodes network traffic, data processing is done in a natural hierarchical structure. Raw data processing of local data is done directly on the Front-End Processors hosted by HLT-REadout Receiver Card (H-RORC) and the Global data processing is done in the computing nodes. The trigger decision, compressed data and Event Summary Data (ESD) of reconstructed events are transferred to DAQ for data recording and archiving.

ALICE control system ensures the smooth and accurate running of the ALICE experiment. It provides access remotely and monitors all the detectors through a user interface which can be operated from the ALICE Control Room (ACR) at LHC point 2. It ensures the highest quality of data by using optimal operational techniques. It is divided into two parts: Experiment Control System (ECS) and Detector Control System (DCS), which are briefly discussed in the following sections.

2.3.4 Detector Control System (DCS)

The DCS [42, 50] accommodates all the changes in the experiment. The control system operates in every phase of the experiment (data taking, shut down, etc.). It is designed to deal with different modes of operations and monitors the proper running of each sub-detector. It checks the experimental environment, like cooling, high or low voltage, water leakage and temperature in the experimental area. There are 8 sub-detectors, which have gas systems with their associated control system. DCS checks those parameters regularly and warns if they show any anomaly. It provides protection to the sub-detectors through its interlock systems. DCS exchanges information such as magnet control system, safety systems, and the primary services with the LHC.

2.3.5 Experiment Control System (ECS)

There are several independent online systems in ALICE which perform different domains of activities. Due to the independent nature of the online system, it interacts with all the particle detectors, and allows partitioning. The detectors run and collect physics data collectively due to this splitting. During the commissioning phase of the beams, the detectors are tested as independent objects in a mode called “standalone mode". The role of ECS [42, 50] is to coordinate the operations of online systems by receiving and sending information to detectors through user interfaces based on Finite-State-Machines (FSM). ECS comprises of four major components, (i) Partition Control Agent (PCA), (ii) Detector Control Agent (DCA), (iii) Partition Control Agent Human Interface (PCAHI), and (iv) Detector Control Agent Human Interface (DCAHI). DCA receives commands from the human interface (DCAHI) and handles the standalone data acquisitions for the detectors running alone. The job of the PCA is to handle data acquisition runs using active detectors in the partition. The PCA can exclude/include any detector from a partition by receiving command from human interface PCAHI.

2.4 Analysis of the Data

The raw data is stored in terms of digital signals with the time information in Peta Bytes order. The reconstruction involves these steps: cluster finding for each detector, primary vertex reconstruction, track reconstruction, and secondary vertex reconstruction. The output is written in Event Summary Data (ESD) files with the name of AliESDs.root after the reconstruction. Later on, depending on the requirements of physics analysis, events are filtered and stored in Analysis Object Data (AOD) files.

Chapter 3

Monte Carlo Studies of the Event-by-Event Fluctuations of Neutral and Charged Particles

3.1 Introduction

A deconfined state of matter is expected to be formed at very high densities and high temperatures in high energy collisions. The equilibrium regions are produced in this hot dense QGP, where the chiral symmetry is nearly restored. The restoration of chiral symmetry and its subsequent relaxation towards the normal vacuum is additionally posited to yield transient region where the value of the chiral order parameter differs from that of the surrounding medium. This is called Disoriented Chiral Condensate (DCC). The region is unstable due to the explicit breaking of chiral symmetry and hence rolls down towards the stable equilibrium position and oscillates. The transition of the DCC region from unstable equilibrium to a stable equilibrium position is associated with the production of low p_{T} particles with different isospins. The low p_{T} pions and kaons which are produced from DCC regions differ in probabilities to the one produced from the normal hadronic state (section 1.6). The normal hadronic matter gives rise to multinomial distribution for the production of pions and kaons of mean 1/3 and 1/2 for pion fraction, f_π and kaon fraction, f_K, respectively. It is not easy to measure the neutral pion and kaon fraction in experiments. These fractions can be measured by obtaining the particle yields. In an experiment, there are particle losses due to reconstruction technique, detection inefficiencies of the device and the method of particle identification used. These particle losses increase the variance of the particle multiplicities in measurement. The yield of pions and kaons might fluctuate irrespective of the DCC production in the measurement.

So it is difficult to measure the fraction in this case. Further, neutral kaons exist as the weak eigenstates of K_L^0 and K_s^0 and on an event-by-event basis, the former is difficult to measure, however, the latter can be identified from its decay to oppositely charged pions having a branching ratio 69.2 %. In this measurement, K_s^0 yield is considered as the total neutral kaon yield as K_L^0 is not measured. Evidently, due to the weak mixing of eigenstates and due to finite branching ratio, K_s^0 yield fluctuates on an event-by-event basis. It is difficult to observe K_s^0 yield directly. The identification of K_s^0 is done by the invariant mass reconstruction using various topological cuts. The reconstruction of the invariant mass of $\pi^+\pi^-$ pairs combinatorially gives K_s^0 candidates in the measurement. It is clear from the above discussion that the yield of K_s^0 and $K^\pm$, hence the kaon fractions fluctuate in various ways. Hence, the fraction, f_K is not a suitable observable to predict the existence of DCC in the measurements. A robust observable which is independent of the detection efficiency is required to study the DCC fluctuations. These can be achieved by studying the fluctuation observable, ν_{dyn} [51] in the analysis, which is predicted to be the indicator of isospin fluctuations in pion and kaon sectors [36].

3.2 Statistical Observable ($\nu_{\rm dyn}$)

Let $\langle N\rangle$ and $\langle N(N-1)\rangle$ be the first and second order factorial moments, of the multiplicity distribution of the considered particles. The variance constructed out of these moments is given by $V = \langle N^2\rangle - \langle N\rangle^2$. For two particle density distribution, the covariance is defined as $V_{ab} = \langle N_a N_b\rangle$ - $\langle N_a\rangle\langle N_b\rangle$, where '$a$' and '$b$' represent distinct particles. The robust variance, R_{aa}, and covariance, R_{ab}, are given by [51],

$$R_{aa} = \frac{V - \langle N_a\rangle}{\langle N_a\rangle^2} = \frac{\langle N_a(N_a-1)\rangle}{\langle N_a\rangle^2} - 1, \tag{3.1}$$

and

$$R_{ab} = \frac{V_{ab}}{\langle N_a\rangle\langle N_b\rangle} = \frac{\langle N_a N_b\rangle}{\langle N_a\rangle\langle N_b\rangle} - 1. \tag{3.2}$$

These two quantities are independent of detection efficiency. Their robustness can be verified by considering the probability of detecting each particle as p and the probability of not detecting it as 1-p. The average number of measured particle for a binomial approximation is $\langle N_{measured}\rangle = \mathrm{p}\langle N\rangle$ and the average square is $\langle N^2\rangle_{measured} = \mathrm{p}^2\langle N^2\rangle + \mathrm{p}(1-\mathrm{p})\langle N\rangle$. The variance is written as,

$$\begin{aligned} V_{measured} &= \langle N^2\rangle_{measured} - \langle N\rangle^2_{measured} \\ &= \mathrm{p}^2\langle N^2\rangle + \mathrm{p}(1-\mathrm{p})\langle N\rangle - \mathrm{p}^2\langle N\rangle^2 \quad (3.3) \\ &= \mathrm{p}^2\left(\langle N^2\rangle - \langle N\rangle^2\right) + \mathrm{p}(1-\mathrm{p})\langle N\rangle. \quad (3.4) \end{aligned}$$

$$
\begin{aligned}
V_{measured} - \langle N\rangle_{measured} &= \mathrm{p}^2\left(\langle N^2\rangle - \langle N\rangle^2\right) + \mathrm{p}(1-\mathrm{p})\langle N\rangle - \mathrm{p}\langle N\rangle \\
&= \mathrm{p}^2\left(V - \langle N\rangle\right).
\end{aligned} \tag{3.5}
$$

From the above equations, the measured value of the $R_{aa}^{measured} = R_{aa}$, which is independent of the detection efficiency. By using the similar technique of detection efficiency, the robustness of covariance term, R_{ab}, can be verified. A statistical dynamic observable, ν_{dyn} is defined as a linear combination of these correlators as [51],

$$\nu_{dyn} = R_{aa} + R_{bb} - 2R_{ab}. \tag{3.6}$$

The individual terms and ν_{dyn} vanish in the absence of pair correlations, i.e., for Poissonian particle production. The values of the correlators (both ν_{dyn} and individual terms) deviate from zero for genuine particle correlations and their magnitude approximately scales inversely to the total multiplicity of heavy-ion collisions [51].

Let N_+ and N_- be the multiplicities of positive and negative particles, respectively. Alternative expression of ν_{dyn} can be obtained by considering variance of the relative multiplicity dependence, which is given by [51],

$$\nu_{+-} = V\left(\frac{N_+}{\langle N_+\rangle} - \frac{N_-}{\langle N_-\rangle}\right) \tag{3.7}$$

$$= \left\langle\left(\frac{N_+}{\langle N_+\rangle} - \frac{N_-}{\langle N_-\rangle}\right)^2\right\rangle \tag{3.8}$$

The variances of hadrons which are independently produced are,

$$\langle N_+^2\rangle - \langle N_+\rangle^2 = \langle N_+\rangle \tag{3.9}$$

$$\langle N_-^2\rangle - \langle N_-\rangle^2 = \langle N_-\rangle \tag{3.10}$$

$$\langle N_+N_-\rangle = \langle N_+\rangle\langle N_-\rangle. \tag{3.11}$$

In this limit,

$$\nu_{+-,stat} = \frac{1}{\langle N_+\rangle} + \frac{1}{\langle N_-\rangle}. \tag{3.12}$$

The fluctuation measures are affected by both dynamical and statistical components. The correlator can be written as, $\nu_{+-} = \nu_{+-,dyn} + \nu_{+-,stat}$. Hence, the dynamical charge observable can be constructed by taking the difference,

$$\nu_{+-,dyn} = \nu_{+-} - \nu_{+-,stat}. \tag{3.13}$$

A nonzero value of $\nu_{+-,dyn}$ indicates that the net charge fluctuations are correlated.

Similarly, the relative fluctuations of K_s^0s and $K^\pm$s yield can be determined by obtaining the $\nu_{dyn}[K^\pm, K_s^0]$. The magnitude of $\nu_{dyn}[K^\pm, K_s^0]$ is determined by the relative strength of charged and neutral kaon correlations: R_{cc} measures the strength of charged kaon correlations, R_{00} measures the strength of neutral kaon correlations, and R_{c0} is sensitive to charged-neutral kaon correlations. Together, the three terms measure the strength of relative fluctuations. Thus, $\nu_{dyn}[K^{\pm}, K_s^0]$ is sensitive to fluctuations of the neutral fraction f_K. The robustness of ν_{dyn} against detection efficiencies has been observed. The multiplicity distributions of the produced particles are affected due to variations in various kinematic cuts. The robustness of ν_{dyn} for the above conditions can be verified by adopting the methods discussed in [52].

3.3 HIJING and AMPT Model Predictions

A baseline study of $\nu_{dyn}[K_s^0, K^{\pm}]$ was performed in Pb-Pb collisions at $\sqrt{s_{NN}} = 2.76$ TeV, by using HIJING and AMPT MC event generators. The study analysed a total of 3 Million HIJING events, whereas 39, 53, and 39 Million AMPT events were studied using options (1) string-melting on (SON) and re-scattering off (ROFF), (2) string-melting off (SOFF) and re-scattering on (RON), and (3) string melting on and re-scattering on, respectively [53]. The generation of events in these MC simulations does not involve any momentum smearing or particle losses and the produced K_s^0s are not decayed. The total number of events are divided into five centrality classes based on the fractional cross-section studied, as a function of the total charged particle multiplicity observed in the forward pseudo-rapidity range ($2.8 \leq \eta \leq 5.1$ and $-3.7 \leq \eta \leq -1.7$). The $K^{\pm}$s and K_s^0s are selected in the $p_{\rm T}$ range $0.2 < p_{\rm T} < 1.5$ GeV/c and the pseudo-rapidity range $|\eta| < 0.5$ for various centrality classes. The inclusive yield of the number of charged kaons, N_c, and the number of K_s^0s, N_0, are obtained on an event-by-event basis. These are used to calculate the first order moments $\langle N_c \rangle$ and $\langle N_0 \rangle$, and second order moments $\langle N_c(N_c - 1) \rangle$, $\langle N_0(N_0 - 1) \rangle$, and $\langle N_c N_0 \rangle$. These moments are combined to calculate the correlators R_{cc}, R_{00}, R_{c0}, and $\nu_{dyn}[N_c, N_0]$ according to Eq. (3.6), for various centrality classes.

The DCC production is not implemented in heavy-ion generators such as HIJING and AMPT but they are equipped with appropriate physical processes to explain most of the observable physical effects in heavy-ion collisions. These models can, therefore, be used to estimate the baseline values of ν_{dyn} without the DCC fluctuations. The strength and the behaviour of the correlator, ν_{dyn}, for various centralities are obtained for these MC models and it exhibits a simple source scaling where the number of sources is expressed in terms of total charged particle multiplicity.

The variation of the values of ν_{dyn} as a function of collision centrality classes obtained from HIJING and AMPT (3 dynamical modes) is shown in Fig. 3.1. A monotonic

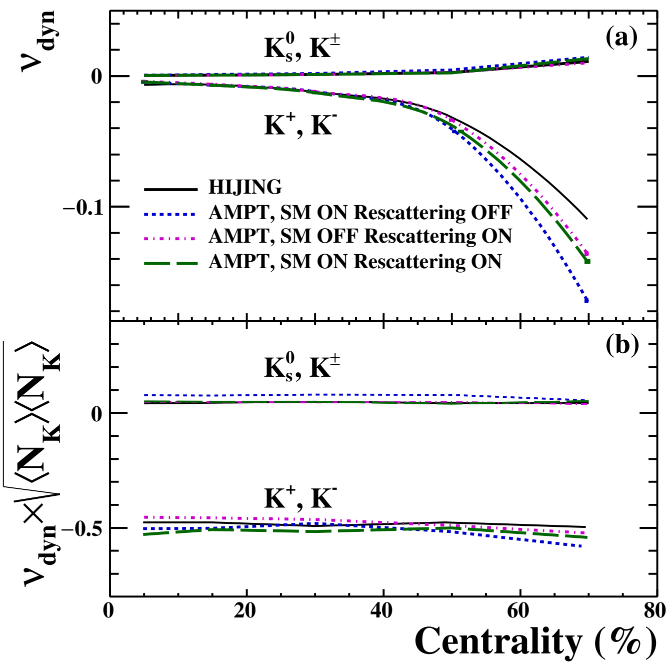

Figure 3.1: (a) The collision centrality dependence of $\nu_{dyn}[K_s^0, K^\pm]$ and $\nu_{dyn}[K^+, K^-]$ in Pb-Pb collisions at $\sqrt{s_{NN}}$ = 2.76 TeV, estimated for MC simulations. (b) ν_{dyn} values scaled by the geometric mean of kaon multiplicities [53].

decrease in the values of ν_{dyn} is observed in all four cases from most peripheral collisions (60-80%) to most central collisions (0-10%). There is a small difference between the values of the obtained correlator for HIJING and AMPT dynamical modes at any given centrality and follow a similar trend with collision centrality. The figure indicates that, even if the effect is small, ν_{dyn} is sensitive to the production of $K^\pm$s, K_s^0s and their correlations.

To account for the source scaling, the values of ν_{dyn} are scaled with the number of sources, N. Here the number of sources refer to the geometric mean of the number of $K^\pm$s and K_s^0s. Fig. 3.1 (b) depicts the variation of $\nu_{dyn} \times \sqrt{N_{K^\pm} N_{K_s^0}}$ as a function of collision centrality. The scaled values obtained from HIJING and AMPT/RON have no collision centrality dependence, whereas the one with AMPT/SON/ROFF exhibits a weak collision centrality dependence. This observation verifies more or less the 1/N scaling.

The values of $\nu_{dyn}[K^\pm, K_s^0]$ are compared with the values of $\nu_{dyn}[K^+, K^-]$ obtained from the model calculations and is depicted in Fig. 3.1 (a). The covariance term of $\nu_{dyn}[K^+, K^-]$, $R_{K^+K^-}$, is larger than either of $R_{K^+K^+}$ or $R_{K^-K^-}$ and therefore $\nu_{\mathrm{dyn}}[K^+, K^-]$ is negative for all collision centralities. However, the charge conservation does not influence the fluctuations of the relative yields of $K^\pm$s, K_s^0s and $\nu_{dyn}[K_s^0, K^\pm]$ substantially and

$\nu_{dyn}[K_s^0, K^\pm]$ takes positive values for all centrality classes. The magnitude of $\nu_{dyn}[K^+, K^-]$ influences in part the value of $\nu_{dyn}[K_s^0, K^\pm]$, given $N_c = N_{K^\pm}$, $N_+ = N_{K^+}$, and $N_- = N_{K^-}$,

$$\begin{aligned}
\langle N_c \rangle &= \langle N_+ \rangle + \langle N_- \rangle \\
\langle N_c(N_c - 1) \rangle &= \langle N_c^2 \rangle - \langle N_c \rangle \\
&= \langle N_+^2 \rangle + \langle N_-^2 \rangle + 2\langle N_+ N_- \rangle - \langle N_+ \rangle - \langle N_- \rangle \\
&= \langle N_+(N_+ - 1) \rangle + \langle N_-(N_- - 1) \rangle + 2\langle N_+ N_- \rangle \qquad (3.14)
\end{aligned}$$

$$\frac{\langle N_c(N_c - 1) \rangle}{\langle N_c \rangle^2} = \frac{\langle N_+(N_+ - 1) \rangle}{\langle N_c \rangle^2} + \frac{\langle N_-(N_- - 1) \rangle}{\langle N_c \rangle^2} + 2\frac{\langle N_+ N_- \rangle}{\langle N_c \rangle^2}. \qquad (3.15)$$

Multiplying the numerator and denominator of first, second, and third term of the Eq. 3.15, by $\langle N_+ \rangle^2$, $\langle N_- \rangle^2$, and $\langle N_+ \rangle \langle N_- \rangle$ respectively, the following is obtained,

$$\begin{aligned}
\frac{\langle N_c(N_c - 1) \rangle}{\langle N_c \rangle^2} &= \frac{\langle N_+(N_+ - 1) \rangle \langle N_+ \rangle^2}{\langle N_c \rangle^2 \langle N_+ \rangle^2} + \frac{\langle N_-(N_- - 1) \rangle \langle N_- \rangle^2}{\langle N_c \rangle^2 \langle N_- \rangle^2} + 2\frac{\langle N_+ N_- \rangle \langle N_+ \rangle \langle N_- \rangle}{\langle N_c \rangle^2 \langle N_+ \rangle \langle N_- \rangle} \\
R_{cc} &= f^2 R_{++} + (1 - f)^2 R_{--} + 2f(1 - f) R_{+-} \\
&= \frac{1}{4}\left[2R_{++} + 2R_{--} - \nu_{\mathrm{dyn}}(N_+, N_-)\right], \qquad (3.16)
\end{aligned}$$

where $f = \langle N_+ \rangle / \langle N_c \rangle$ and in the Eq. 3.16, it is assumed that $f = 0.5$, which is approximately valid at LHC energy. The values of $\nu_{dyn}[K^+, K^-]$ scaled by the geometric mean of the number of charged kaons do not have collision centrality dependence, while AMPT/SON/ROFF exhibits a modest collision centrality dependence.

3.4 DCC Model Simulations

There are various factors on which experimental observations of DCC signals can rely, such as the probability of the production of DCC in a collision, the number of produced DCC domains in an event, domain size, the particles emitted from these domains, and the interaction of the particles with the rest of the collision system. These factors make the detection of the DCC signal challenging experimentally. A simplistic toy model simulation is performed in this section in accordance with [54, 55], which simulates qualitatively the DCC production in the strange sector in heavy-ion collision systems. The numbers and sizes of such DCC regions relative to the full system size are varied in this study.

The simulated pion and kaon multiplicity are similar to as measured by the ALICE experiment in Pb-Pb collisions at $\sqrt{s_{\mathrm{NN}}} = 2.76$ TeV. The simulator is designed to possess both normal and DCC generation components. The normal generation produces charged and neutral particles based on binomial distribution, whereas the DCC particle generation is obtained from Eqs. (1.20, 1.26) for pions and kaons, respectively. A parameter, f_{DCC}, is used to set the DCC matter either entirely or as a mixture of normal and DCC matter.

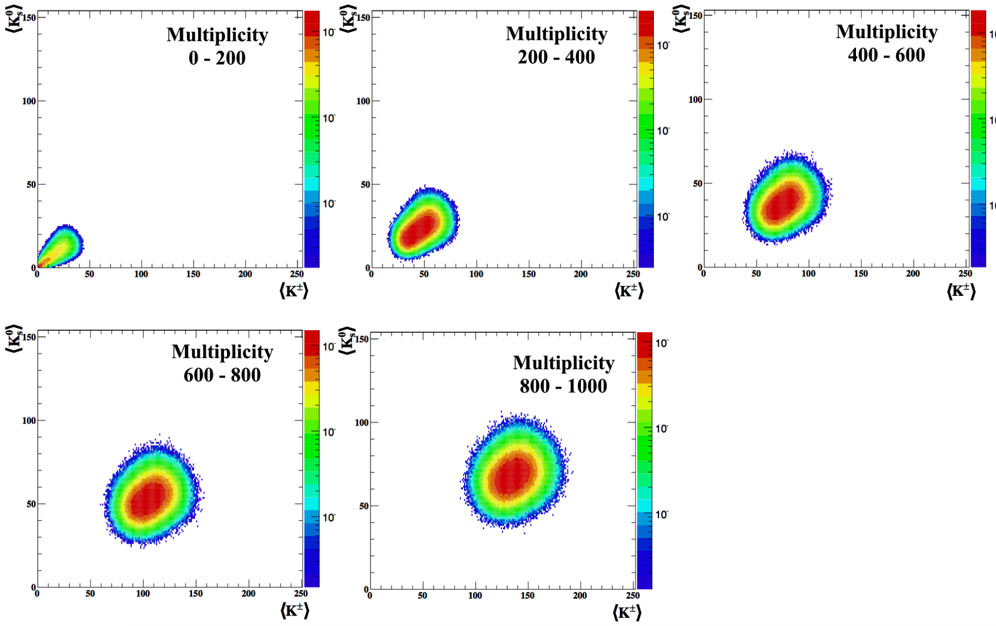

Figure 3.2: The variation of mean number of K_s^0s, $\langle K_s^0 \rangle$, with mean number of $K^{\pm}$s, $\langle K^{\pm} \rangle$ for various multiplicity classes obtained from toy model simulations.

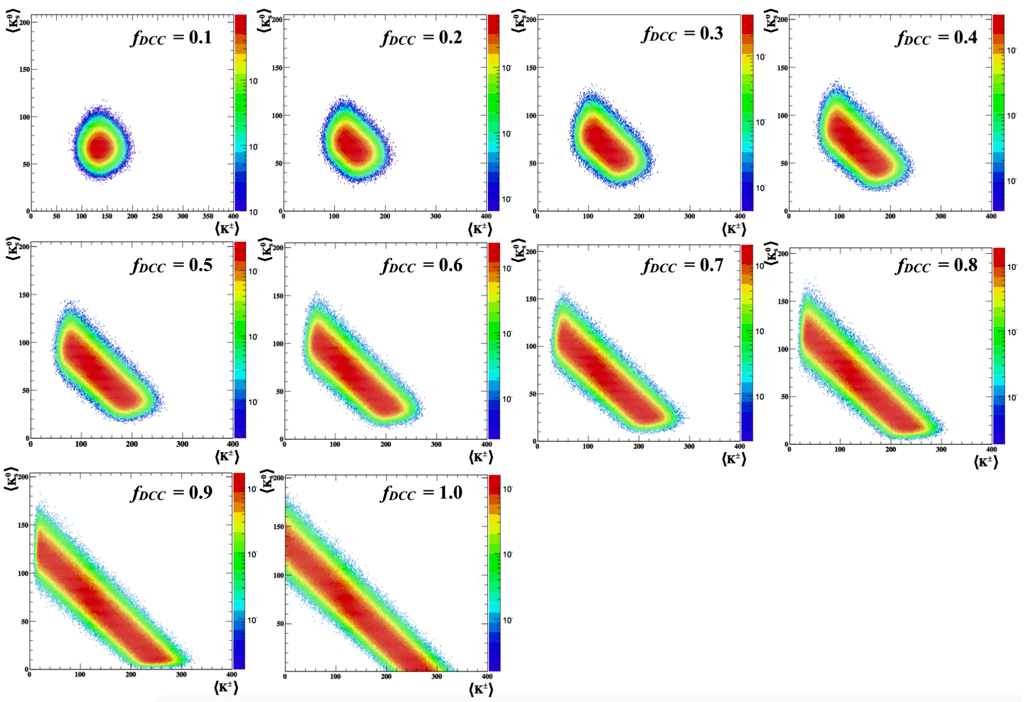

Figure 3.3: The variation of mean number of K_s^0s, $\langle K_s^0 \rangle$, with mean number of $K^{\pm}$s, $\langle K^{\pm} \rangle$ for various values of f_{DCC} for a given multiplicity class (800-1000 multiplicity).

This parameter controls the production of charged and neutral particles under binomial and DCC components. A user selected parameter, f_K, is set at the start of the simulation to obtain the average fraction of particles consisting of kaons in this simulation. The ratio of the kaon to pion yield fluctuates according to the binomial distribution determined by this user selected fraction and the multiplicity. This multiplicity distribution is obtained from the uniform distribution that approximately reproduces the charged particle multiplicity in 0-10% collision centrality reported by ALICE collaboration. The total kaons are generated out of the multiplicity according to a binomial distribution. The number of K_s^0s are generated randomly for both DCC and normal production according to a binomial distribution with a mean probability of 0.5 based on the neutral kaon numbers in each part. Fig. 3.2 depicts the evolution of the mean number of K_s^0s and mean number of $K^{\pm}$s with multiplicity, for binomial production. Fig. 3.3 illustrates the evolution of mean number of K_s^0s and mean number of $K^{\pm}$s with f_K, for high multiplicity (800-1000) events.

The numbers and sizes of the DCC regions are varied to explore the effect of DCC production in generated event samples. Fig. 3.4 (a) depicts the probability distribution of the neutral pion fraction and (b) displays the probability distribution of the neutral kaon fraction obtained using the selected values of the DCC fraction $f_{\rm DCC}$ in generated events. Various particle production scenarios were considered in this study: **Scenario 1**: All the generated events contain one DCC domain but the domain size is varied by varying the fraction of (a) pions and (b) kaons produced relative to the system. Fig. 3.5 displays the variation of ν_{dyn} with the event multiplicity for various values of DCC fraction for pions (a) and kaons (b). The figure shows that ν_{dyn} increases monotonically with the DCC size and has higher values for events containing large DCC fractions. The value of the ν_{dyn} increases from large event multiplicity to small event multiplicity for a particular DCC fraction. The cross correlation (R_{c0}) weakens compared to R_{00} and R_{cc} in the small event multiplicity. The higher values of $\nu_{dyn}[\pi^0, \pi^{\pm}]$ are observed compared to $\nu_{dyn}[K_s^0, K^{\pm}]$ for a particular DCC fraction. **Scenario 2**: The probability of the occurrence of DCC ($p_{\rm DCC}$) is changed while keeping DCC size fixed. Fig. 3.6 illustrates that ν_{dyn} increases as a function of $p_{\rm DCC}$. The values are sensitive to pions compared to kaons and they have distinct values even for the small occurrence of the probability i.e, $p_{\rm DCC} = 0.01$. **Scenario 3**: The generated HIJING events are considered as the baseline measurement for event-by-event fluctuations of the kaons and their productions. The DCC fluctuations are introduced in HIJING events by randomising the neutral and charged kaons on an event-by-event basis. Fig. 3.7 (a) depicts the the evolution of $\nu_{dyn}[K_s^0, K^{\pm}]$ with collision centrality obtained by increasing the fraction of events containing a single DCC. The default values of HIJING denote that DCC is not introduced in the generated events. The

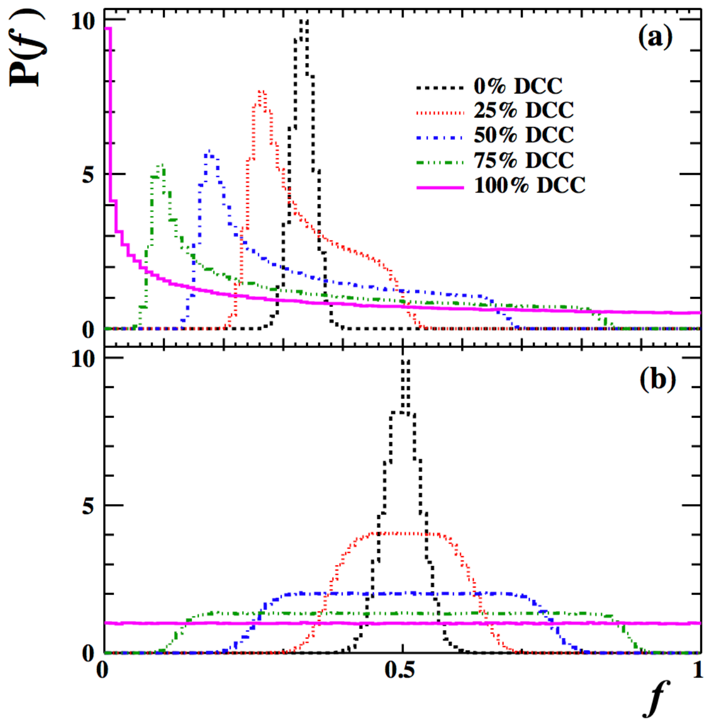

Figure 3.4: The probability distribution of (a) neutral pion fraction, f_π and (b) neutral kaon fraction, f_k for selected values of f_{DCC} [53].

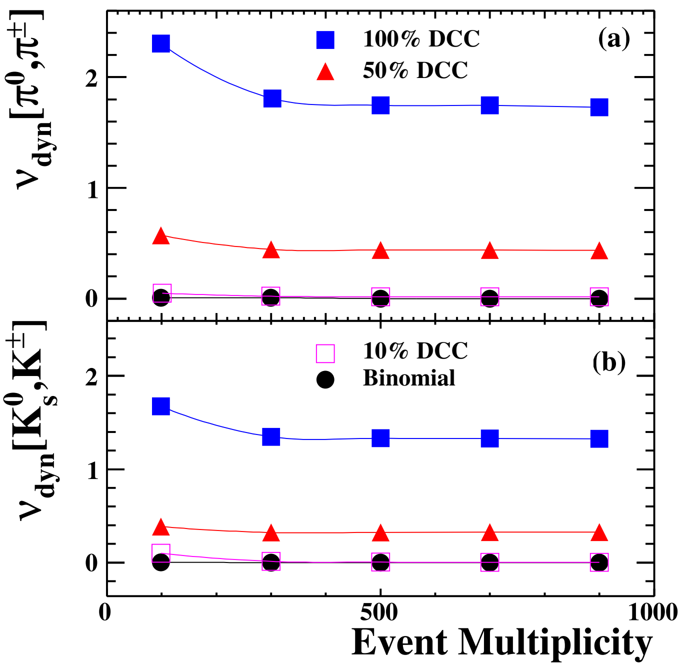

Figure 3.5: Evolution of (a) $\nu_{dyn}[\pi^0, \pi^\pm]$ and (b) $\nu_{dyn}[K_s^0, K^\pm]$, with event multiplicity for selected values of the fraction of particles produced within DCCs [53].

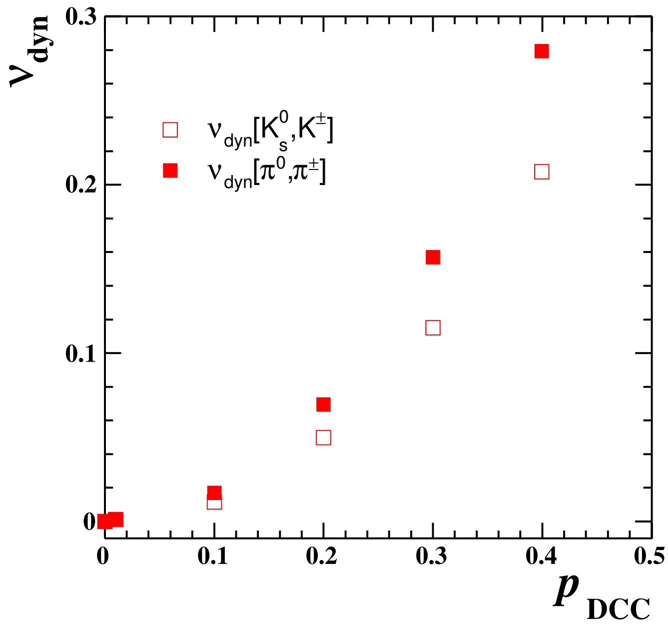

Figure 3.6: ν_{dyn} as a function of percentage of DCC-like events (p_{DCC}) for a given multiplicity bin [53].

figure depicts that, with an increase in event multiplicity, ν_{dyn} exhibits approximate 1/N scaling, where N is the number of sources. The introduction of DCC like fluctuations in HIJING events changes both the behaviour and values of ν_{dyn}. The values are sensitive to the fraction of DCC in events and the values are substantially higher compared to the default values. The values are scaled with the geometric mean of the number of kaons (Fig. 3.7 (b)) and the mean charged particle density (Fig. 3.7 (c)) to nullify the effect of centrality. The scaled values are invariant with collision centrality for HIJING baseline (default) study. However, the values have large centrality dependence for HIJING events with DCC like fluctuations. The significant deviation is observed even for 1% DCC fraction in the generated events. From this study, it is evident that ν_{dyn} is sensitive to the DCC like fluctuations in Pb-Pb collisions. **Scenario 4**: All generated HIJING events are assumed to contain multiple DCC domains by considering differential regions of η and ϕ. The size of the multiple domains is varied by changing the fraction of kaons on an event-by-event basis. The values of the ν_{dyn} are calculated for events with multiple domains of DCC and compared with the events containing single DCC domain, obtained for 1%, 2%, and 5% DCC fraction as depicted in Fig. 3.8(a), (b), and (c), respectively. A centrality dependence is observed in the multiple domains scenarios and ν_{dyn} is sensitive to the number of DCC regions. It can also be observed from Fig. 3.8(a) that, with an

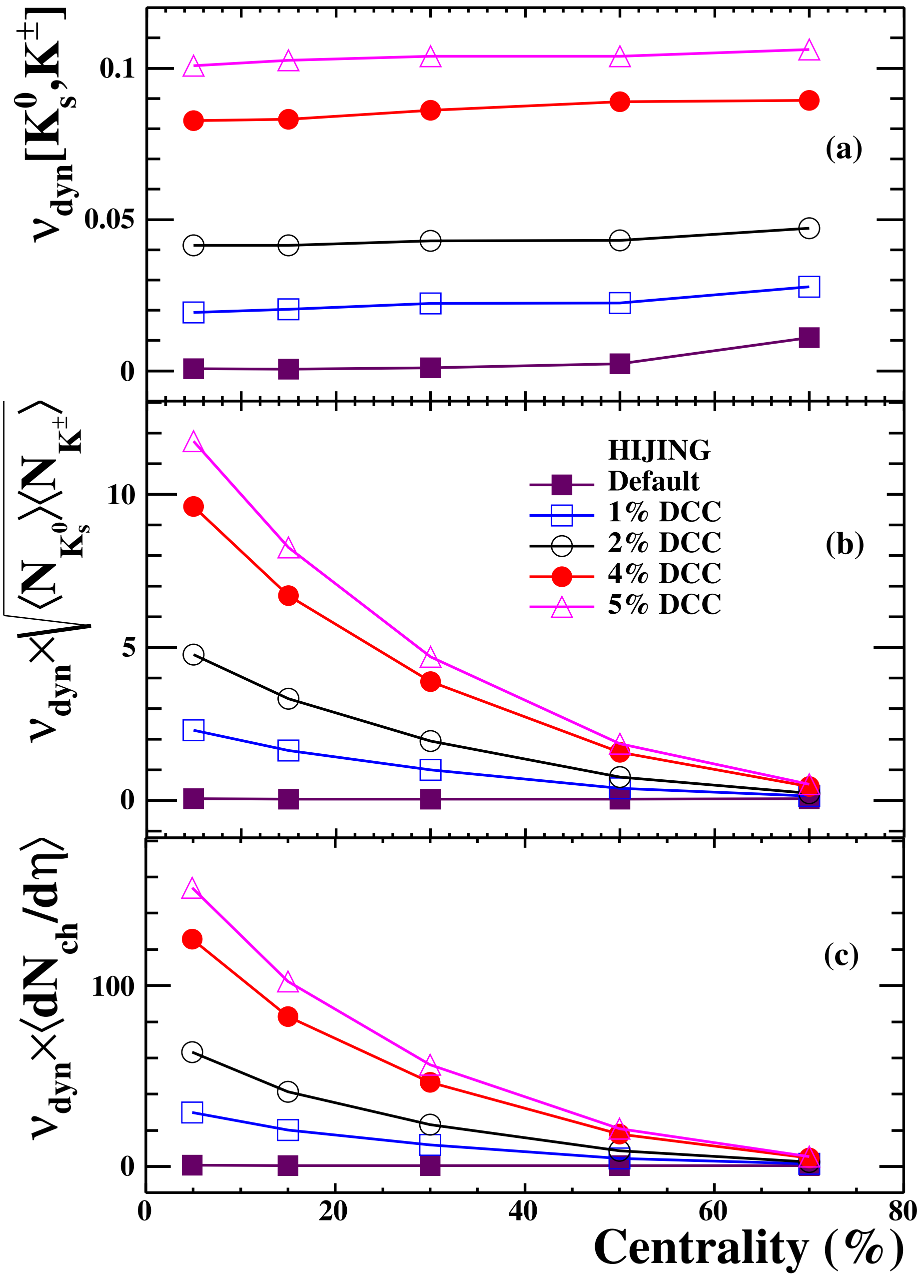

Figure 3.7: (a): $\nu_{dyn}[K_s^0, K^\pm]$ as a function of centrality, (b): $\nu_{dyn}[K_s^0, K^\pm]$ scaled with kaon multiplicity as a function of centrality, and (c): $\nu_{dyn}[K_s^0, K^\pm]$ scaled with charged particle multiplicity density as a function of centrality, for Pb−Pb collisions at $\sqrt{s_{\rm NN}}$ = 2.76 TeV [53].

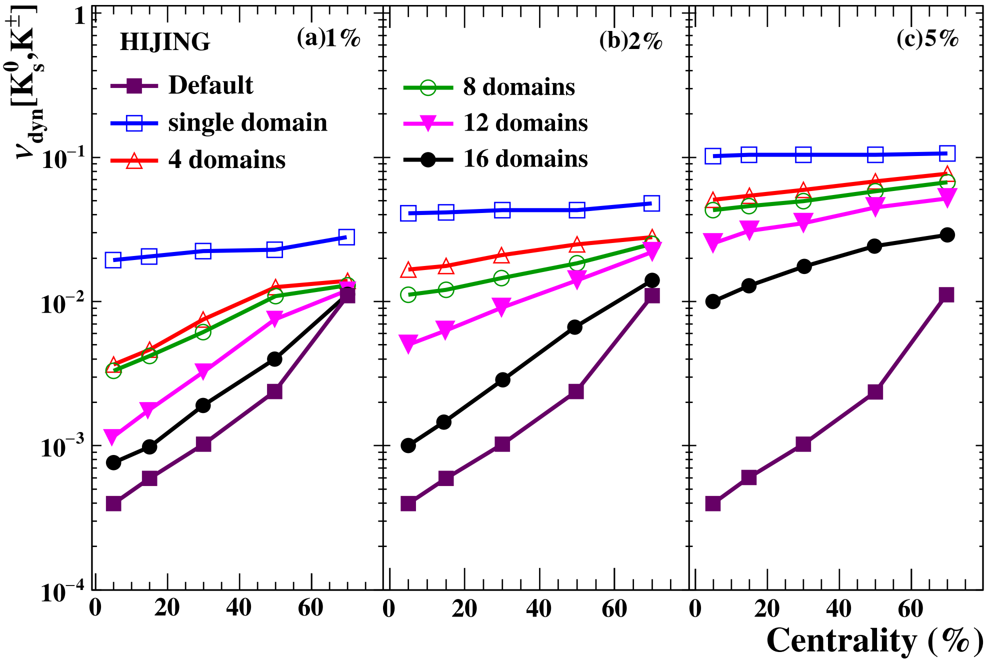

Figure 3.8: $\nu_{dyn}[K_s^0, K^{\pm}]$ as a function of centrality in single and multi-domain scenarios of DCC production for (a) 1%, (b) 2%, and (c) 5% of DCC fractions for Pb−Pb collisions at $\sqrt{s_{\rm NN}}$ = 2.76 TeV [53].

increase in the number of DCC domains, ν_{dyn} nearly approaches the values of HIJING baseline. A similar trend is observed even for higher values of DCC fraction which are depicted in Fig. 3.8(b) and Fig. 3.8(c). The studies indicate that ν_{dyn} is sensitive to the presence of DCC like events in heavy-ion collisions.

Chapter 4

Analysis of the Event-by-Event Fluctuations of Charged and Neutral Kaons in Pb-Pb Collisions at $\sqrt{s_{\mathrm{NN}}}$ = 2.76 TeV

4.1 Introduction

The analysis of event-by-event fluctuations of the relative yield of neutral and charged kaons in the Pb-Pb collisions at $\sqrt{s_{\mathrm{NN}}}$ = 2.76 TeV using ALICE detector at the LHC has been discussed in this chapter. The statistical observable, ν_{dyn}, has been used to measure the fluctuation and the method discussed in the previous chapter has been employed for this analysis. The values of the observable quantify the fluctuations. A number of model studies have been performed to establish a baseline for the kaon isospin fluctuations. The Geometry and Tracking (GEANT) simulations have been performed to study the response of the detector system. The background corrections, systematic and statistical uncertainties calculations are discussed.

4.2 Experimental Data Sample

The analysis was carried out using 13 Million Pb-Pb (LHC 10h pass2) events at $\sqrt{s_{\mathrm{NN}}}$ = 2.76 TeV, which were collected during the first LHC heavy-ion run in 2010. The Monte-Carlo (MC) data (at generated and reconstructed level) was used to study the effect of detector performance. The analysis was carried out with the simulated Pb-Pb collisions data produced with the HIJING [56] and AMPT [57] MC event generators. The details of the datasets are shown in Table 4.1. All sets of simulated data were analyzed with selection parameters and conditions, identical to those used in the analysis of the experimental data.

Details of the real and MC dataset	
Data type	Number of events
ALICE Data	13 Million (LHC10h pass2)
HIJING	3 Million (LHC11a10a_bis)
AMPT(String Melting ON Rescattering OFF)	39 Million (LHC13f3a)
AMPT(String Melting OFF Rescattering ON)	53 Million (LHC13f3b)
AMPT(String Melting ON Rescattering ON)	39 Million (LHC13f3c)

Table 4.1: ALICE datasets obtained for Pb-Pb collisions at $\sqrt{s_{\mathrm{NN}}}$ = 2.76 TeV used for the present analysis.

4.3 Event Selection

The following section briefly describes the event selection criteria used for this analysis. The main purpose of the event selection in the heavy-ion run is to obtain high-efficiency interactions after rejecting background from beam-beam interactions and background induced by machines. The following section describes the detailed event selection criteria used for this analysis.

4.3.1 Minimum Bias Trigger Selection

A Minimum Bias (MB) trigger has been used in this analysis, which provides ideally no bias while selecting the event. The MB trigger requires three simultaneous hits in the two inner layers of the Inner Tracking System (ITS) and at least one hit in both V0A and V0C detectors.

4.3.2 Background Rejection

After selecting the triggered events, the effect of additional background events originating due to the interaction of beams with the matter in the machine is studied. The effect of this background increases with the intensity of the beam and also depends on the residual gas pressure inside the beam pipe. Another source of background is due to the interaction of beam halo ions with the machines. These interactions mostly occur outside the interaction region and thus produce a signal that is detected earlier in the same-side of V0 detector, compared to the one in the nominal interaction region between the V0 detectors. Therefore, these events can be rejected using the timing information of the V0 detectors. The photo-production and photo-nuclear interactions generated due to the electromagnetic fields of the relativistic heavy-ions also give rise to background induced by these physical processes. These processes should be isolated from the hadronic interactions in heavy-ion collisions and are generally achieved by implementing selection cuts in each of the neutron ZDC detectors.

4.3.3 Vertex Selection

The background events can be reduced by applying a constraint on the z component of the collision vertex. The position of the z vertex, V_z, is determined by the SPD by calculating the weighted mean of the z_i distributions around the region of interest. All the events are populated around the nominal interaction point i.e, $z \sim 0$. The background events are positioned at a higher V_z values. Therefore a vertex selection cut of $|V_z| < 10$ cm is applied to reduce the background and to achieve a uniform acceptance of the central detectors.

4.3.4 Centrality Selection

Each event in heavy-ion collisions has a certain impact parameter, b. The impact parameter cannot be measured directly in the experiment. An experimentally measured quantity, centrality, is defined, which is related to the total hadronic interaction cross-section, σ_{AA}. The centrality percentile, c, of nucleus-nucleus collision with impact parameter, b, is defined as [58],

$$c(b) = \frac{\int_0^b \frac{d\sigma}{db'} db'}{\int_0^\infty \frac{d\sigma}{db'} db'} = \frac{1}{\sigma_{AA}} \int_0^b \frac{d\sigma}{db'} db'. \tag{4.1}$$

Experimentally, the centrality can be obtained by measuring charged particle multiplicity, N_{ch}, and energy deposition in ZDC, E_{ZDC},

$$c \approx \frac{1}{\sigma_{AA}} \int_{N_{\mathrm{ch}}}^\infty \frac{d\sigma}{dN'_{\mathrm{ch}}} dN'_{\mathrm{ch}} \approx \frac{1}{\sigma_{AA}} \int_0^{E_{\mathrm{ZDC}}} \frac{d\sigma}{dE'_{\mathrm{ZDC}}} dE'_{\mathrm{ZDC}}. \tag{4.2}$$

The centrality is determined by the charged particle multiplicity measured in V0 detectors as shown in Fig. 4.1. The centrality bins are obtained by integrating the charged particle multiplicity distribution in Eq 4.2. To obtain the absolute scale, the V0 amplitude

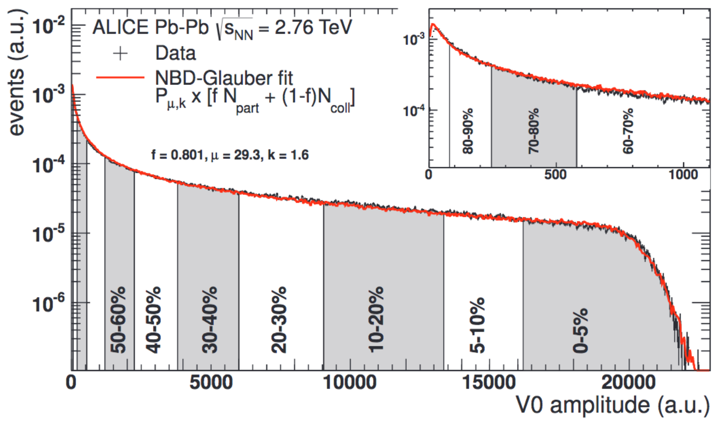

Figure 4.1: Distribution of the V0 amplitude (sum of V0A and V0C) measured by ALICE experiment in Pb-Pb collisions at $\sqrt{s_{\mathrm{NN}}}$ = 2.76 TeV. The centrality bins are defined by integrating from right to left following Eq. 4.2. The absolute scale is determined by fitting to the NBD-Glauber model (red line) [59].

is fitted with NBD-Glauber fit. Assuming that nucleons follow straight-line trajectories and encounter binary nucleon-nucleon collisions, the Glauber model describes collision geometry using a known nuclear density profile [58]. The MC Glauber model is used to calculate the number of participants, N_{part}, and the number of binary collisions, N_{coll}, for a given impact parameter. The charged particle multiplicity distribution is modelled using a two-component approach which is used to quantify the relative contribution of soft and hard processes in the particle production mechanism at different energies [59]. In the scenario dominated by a soft process, the charged particle multiplicity is expected to linearly scale with N_{part} [59]. The linear scaling with N_{coll} is expected for particle production where hard collisions dominate over soft collisions. If $N_{\mathrm{ancestors}}$ be the number of emitting sources of particles then it can be determined by the two-component model as [60],

$$N_{\mathrm{ancestors}} = fN_{\mathrm{part}} + (1-f)N_{\mathrm{coll}}, \tag{4.3}$$

where f controls the relative contribution from the soft and hard process. The anchor point (AP) is defined as the absolute scale of centrality determination which requires the knowledge of the trigger efficiency and the remaining background contamination in nuclear collision events. Table 4.2 represents the centrality ranges, corresponding minimum (b_{min}) and maximum (b_{max}) impact parameter and total charged particle multiplicity density ($\langle dN_{ch}/d\eta \rangle$) for Pb-Pb collisions at $\sqrt{s_{\mathrm{NN}}}$ = 2.76 TeV. In this analysis, the V0 detector is used as a centrality estimator and 0-80 % centrality has been selected.

Centrality	b_{min} (fm)	b_{max} (fm)	$dN_{ch}/d\eta$
0-5 %	0.0	3.5	1601 ± 60
5-10 %	3.5	4.95	1294 ± 49
10-20 %	4.95	6.98	966 ± 37
20-30 %	6.98	8.55	649 ± 23
30-40 %	8.55	9.88	426 ± 15
40-50 %	9.88	11.04	261 ± 9
50-60 %	11.04	12.09	149 ± 6
60-70 %	12.09	13.06	76 ± 4
70-80 %	13.06	13.97	35 ± 2

Table 4.2: The centrality, corresponding impact parameter, and total charged particle multiplicity density obtained from MC NBD-Glauber fit to the V0 amplitudes as measured by ALICE experiment in Pb-Pb collisions at $\sqrt{s_{\mathrm{NN}}}$ = 2.76 TeV [59].

4.4 Track Selection

An event in heavy-ion collisions produces thousands of particles that come out of the reaction zone and hit the detectors. The particles which are tracked in the detectors are not all primary. There are contributions coming from secondary interactions with the materials of the detectors. There is a possibility that primary tracks may not fall in the detector acceptance and hence cannot be reconstructed efficiently. Primary tracks are the tracks produced in the collision, including products of strong, electromagnetic decays and weak decays of charm and beauty particles, free from the strange weak decays and other secondary particles [61]. The tracks are selected according to the analysis requirements and detector acceptance in the region of interest. The tracks are selected on the basis of specific quality cuts and are technically assigned a filter bit values. Filter bit 272 is used in this analysis which has predefined cuts based on distance of closest approach (DCA) of a track to the event vertex, the number of TPC clusters, χ^2/ndf of the track fitting, kink produced from weak decays and asking whether it requires ITS refit or not for track reconstruction. The DCA cuts of 2.4 cm and 3.2 cm are applied in the xy and z direction, respectively, to ensure the tracks from the primary vertex. The cut for number of TPC clusters is 70. This cut is used which ensures high-efficiency track reconstruction and minimizes the contribution of photon conversion and secondary charged particles production in detector materials. A χ^2/ndf cut of 4 is used to remove the tracks which are not coming from collision vertex. The tracks with the kink are rejected. The tracks with transverse momentum (p_{T}) range 0.2-1.5 GeV/c has been applied and a pseudorapidity

Track parameters	Cut values
Minimum number of TPC clusters	70
χ^2/ndf per TPC cluster	4
DCA to vertex-xy	2.4 cm
DCA to vertex-z	3.2 cm
Accept kink daughter	No
TPC refit require	Yes
ITS refit require	Yes

Table 4.3: The values of the track cuts (filter bit 272) in Pb-Pb collisions at $\sqrt{s_{NN}}$ = 2.76 TeV.

(η) of $|\eta| < 0.5$ is selected. The details of the track cuts are given in Table 4.3. The ALICE experiment has the ability to identify particles with momentum from 0.1 GeV/c up to a few tens of GeV/c.

4.5 Particle identification

The main objective of the analysis is to obtain the number of charged ($K^{\pm}$) and neutral (K_s^0) kaons for each centrality. The $K^{\pm}$s are selected on the basis of combined information from TPC and TOF detectors. The V0 reconstruction technique has been used to select K_s^0s.

4.5.1 Charged Kaon Selection

The $K^{\pm}$s are selected on the basis of signals measured in the TPC and TOF detectors. The particle identification in TPC is based on the measurement of specific energy loss of the particle in the TPC volume while the time of flight information is used to identify particle in the TOF. Fig. 4.2 represents the energy loss of particles per unit length as a function of momentum of the tracks. These bands merge at a certain momentum range. Fig. 4.4 **(a)** shows the distribution of the specific energy loss of pion, electron and kaon within track momentum interval of 0.38 - 0.39 GeV/c. The energy loss distribution is fitted with a triple Gaussian function. From the figure, it can be observed that the kaons are contaminated by other misidentified tracks (i.e, electrons and pions). The increase in the track momentum increases the contamination of kaon tracks by pions. A high efficiency kaon sample can be obtained by applying $|n\sigma|$ cuts. This is defined as the deviation of measured energy loss to the expected energy loss of a particle species given

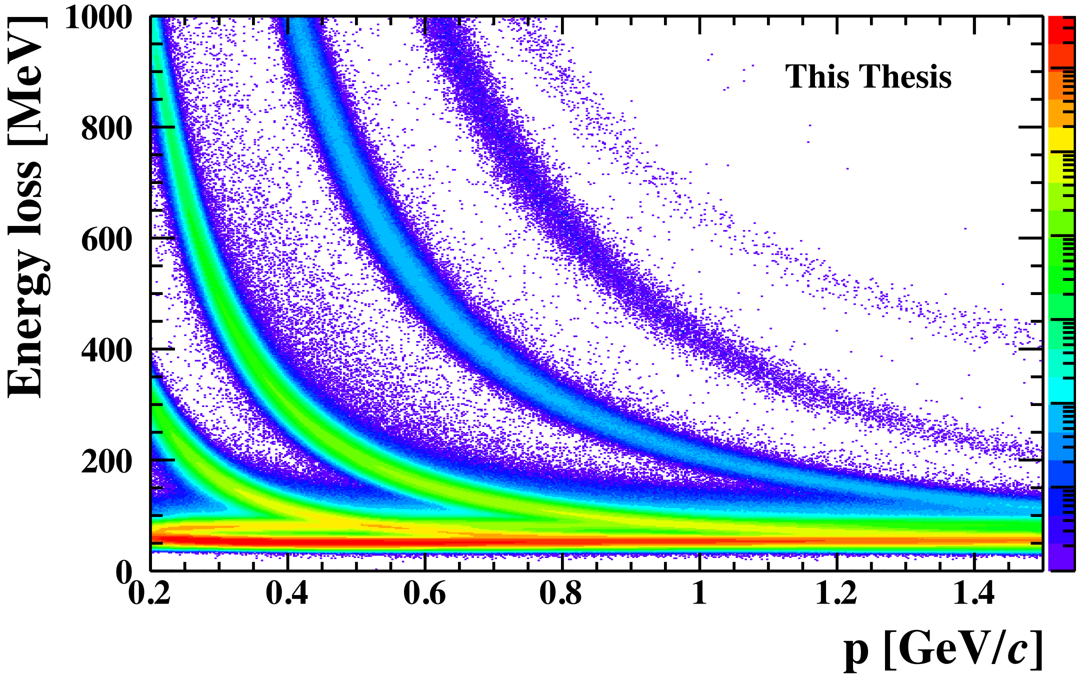

Figure 4.2: The specific energy loss (dE/dX) of tracks as a function of track momentum in Pb-Pb collisions at $\sqrt{s_{\mathrm{NN}}}$ = 2.76 TeV, as measured by ALICE TPC.

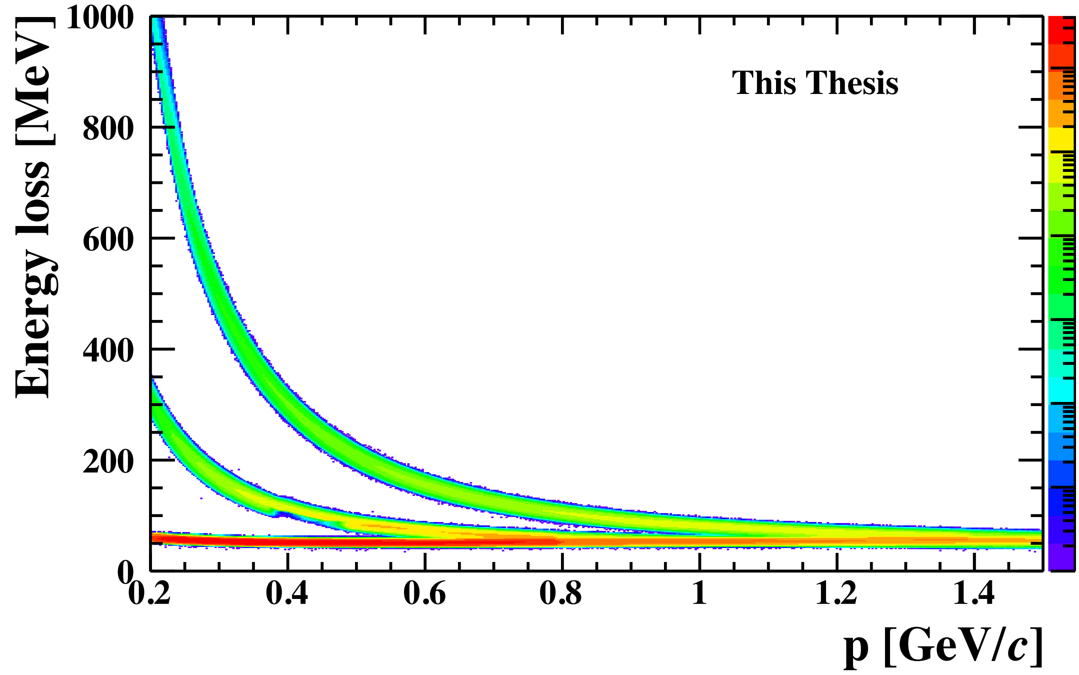

Figure 4.3: The specific energy loss (dE/dX) of tracks as a function of track momentum after applying suitable particle identification cuts in Pb-Pb collisions at $\sqrt{s_{\mathrm{NN}}}$ = 2.76 TeV, as measured by ALICE TPC.

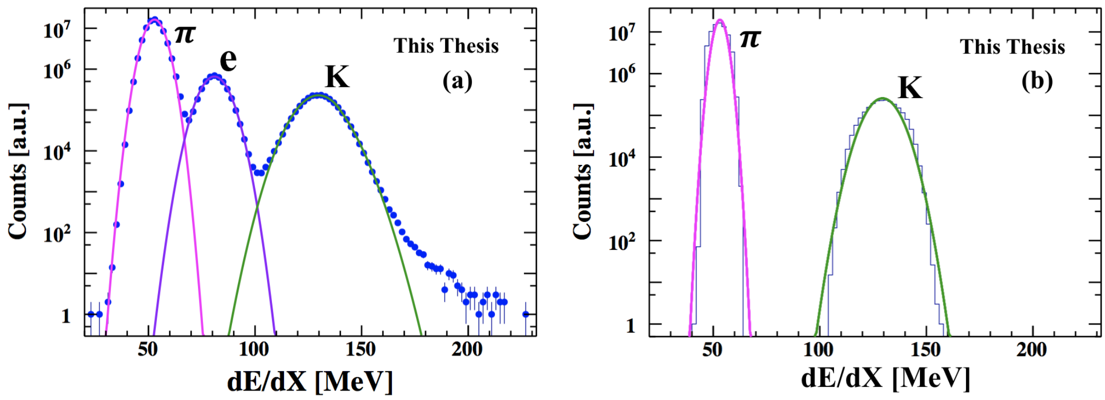

Figure 4.4: The distribution of dE/dX (measured in TPC) before **(a)** and after **(b)** applying particle identification cuts in Pb-Pb collisions at $\sqrt{s_{\rm NN}}$ = 2.76 TeV. The solid line corresponds to the Gaussian fit. The peaks correspond to different identified tracks.

by,

$$n\sigma_{TPC} = \frac{|\frac{dE}{dX}|_{\rm measured} - |\frac{dE}{dX}|_{\rm expected}}{\sigma\left(\frac{dE}{dX}\right)}, \tag{4.4}$$

where $\sigma\left(\frac{dE}{dX}\right)$ is the dE/dX resolution of TPC detector, $|\frac{dE}{dX}|_{\rm measured}$ is the energy loss measured in the TPC and $|\frac{dE}{dX}|_{\rm expected}$ is the energy loss calculated from Bethe-Bloch equation [47] for a particular particle species. The specific energy loss of tracks are obtained as a function of track momentum after applying $|n\sigma|$ cuts and is shown in Fig. 4.3. The bands obtained after the implementation of cuts are fairly distinct in low momentum region. Fig. 4.4 **(b)** depicts the energy loss distribution of particle tracks for momentum interval between 0.38 - 0.39 GeV/c. The information from TOF detector is used along with TPC to obtain a purer sample of kaons upto 1.5 GeV/c. The TOF detector uses the time of flight information of the particle given by,

$$n\sigma_{TOF} = \frac{(time_{hit} - startTime) - time_{expected}}{\sigma(\mathrm{TOF})}, \tag{4.5}$$

where σ(TOF) refers to the resolution of TOF detector, $time_{hit}$ is the time of flight measured in TOF detector and $time_{expected}$ is the expected time of flight of particle of interest. The velocity (β) of the particle can be obtained by measuring the time difference and the particles are identified by studying the variation of TOF β as a function of track momentum (shown in Fig. 4.6). The particle bands appear quite distinct after applying $n\sigma$ cuts for TOF (shown in Fig. 4.7). The pion and the proton exclusion cuts of $|n\sigma| > 2$ were applied in all momentum bins. A $|n\sigma|$ cut of 2 was applied for $K^{\pm}$s in all momentum bins except in the range $0.39 < p < 0.47$(GeV/c), as this momentum interval has substantial contamination. The momentum dependent cuts used are listed in Table 4.4. The con-

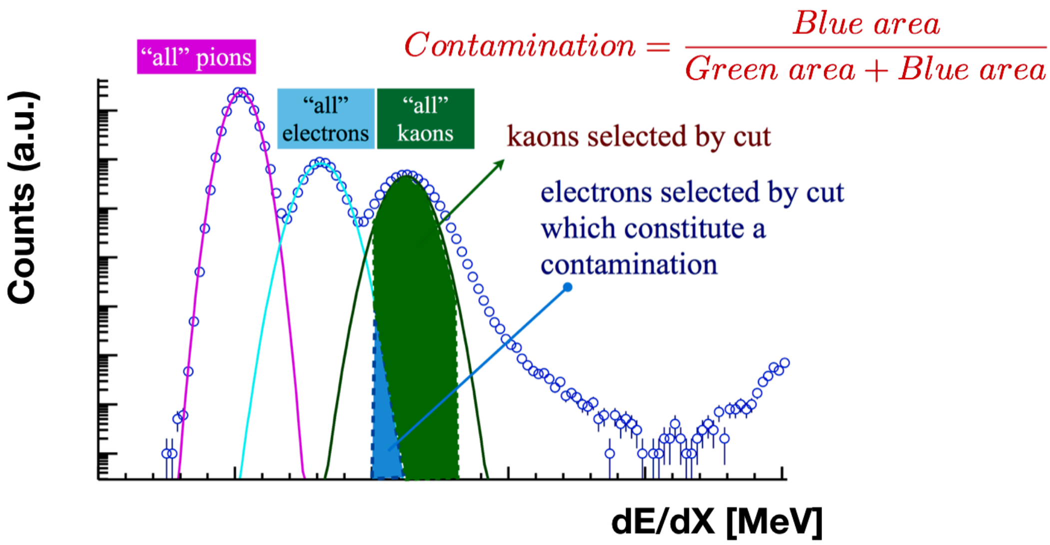

Figure 4.5: Illustration of the method used to calculate the contamination under the kaon peak.

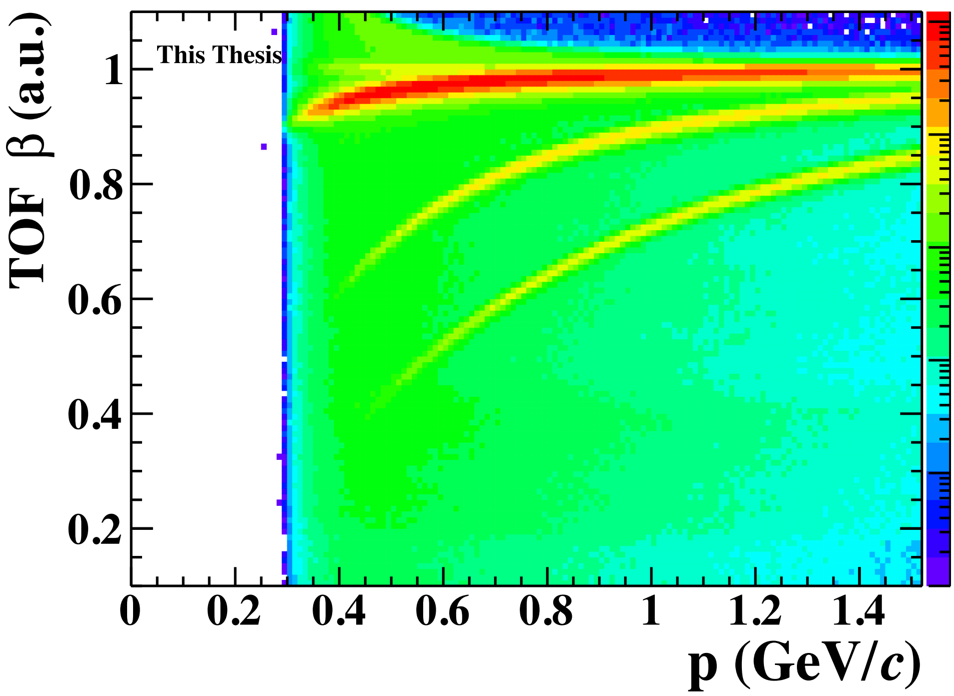

Figure 4.6: TOF β distribution as a function of track momentum in Pb-Pb collisions at $\sqrt{s_{\mathrm{NN}}}$ = 2.76 TeV.

p(GeV/c)	$\|n\sigma\|$	Detectors
$0.2 < p < 0.39$	$\|n\sigma\|_{TPC,k} < 2.0$	TPC
$0.39 < p < 0.47$	$\|n\sigma\|_{k_{left}}$ >-0.5,$\|n\sigma\|_{k_{right}}$ <2.0	TPC
$0.47 < p < 0.5$	$\|n\sigma\|_{TPC,k} < 2.0$	TPC
$0.5 < p < 0.7$	$\|n\sigma\|_{TPC,k} < 2.0$, $\|n\sigma\|_{TOF,k} < 2.0$	TPC + TOF
$0.7 < p < 1.5$	$\|n\sigma\|_{TOF,k} < 2.0$	TOF

Table 4.4: The variation of nσ cuts for different track momentum intervals in Pb-Pb collisions at $\sqrt{s_{\mathrm{NN}}}$ = 2.76 TeV.

tamination in the kaon for different momentum ranges was calculated by the following procedure as illustrated in Fig. 4.5.

The contamination is evaluated as the ratio of the area of the electron distribution overlapping with the selected region of the kaon distribution to that of the area of the selected kaon distribution (after applying nσ cuts). A similar procedure is employed to calculate the background contamination in kaons for TOF β distribution. The contamination level of electron and pion inside the kaon obtained from TPC and TOF for different momentum intervals is of the order of 2.7%. The TOF detector was used along with TPC in the range 0.5 GeV/c < p < 0.7 GeV/c, while only TOF information was used in the range 0.7 GeV/c < p < 1.5 GeV/c. The contamination in the region where only TOF is used is found to be of the order 2%.

4.5.2 K_s^0 Selection

The measurement of K_s^0 is carried out on basis of weak decay topology, $K_s^0 \rightarrow \pi^+ + \pi^-$. These decays are identified from the decay topology of V0 particle and from the invariant mass of K_s^0. The decay vertex of K_s^0 is reconstructed from pairs of detected $\pi^+\pi^-$ tracks. The cuts used to increase the purity of the K_s^0 sample is shown in Table 4.5.

Cuts	Value
p_{T}	0.2 - 1.5 (GeV/c)
$\|\eta\|$	< 0.8
DCA to the primary vertex	> 0.1 cm
$\|n\sigma\|$	< 2.0

Table 4.5: The cuts used to identify the decay daughters for K_s^0 reconstruction in Pb-Pb collisions at $\sqrt{s_{\mathrm{NN}}}$ = 2.76 TeV.

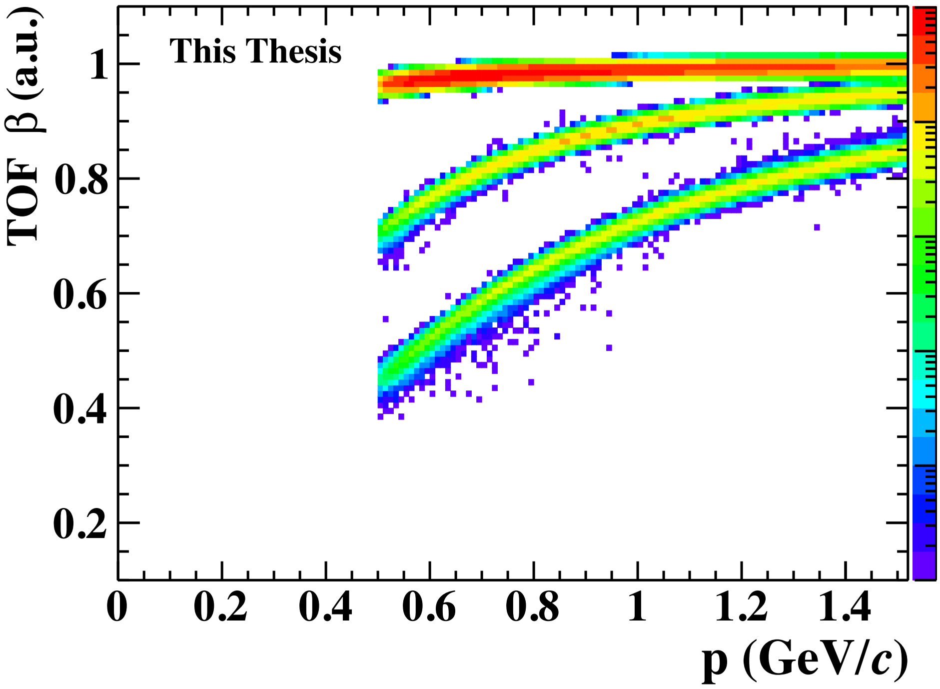

Figure 4.7: TOF β distribution as a function of track momentum in Pb-Pb collisions at $\sqrt{s_{\mathrm{NN}}}$ = 2.76 TeV, after implementing particle identification cuts.

Cuts	Value
p_{T}	0.4 - 1.5 (GeV/c)
$\|\eta\|$	< 0.5
decay length	$< 3\ c\tau$
cosine of pointing angle (Cos(PA))	> 0.99
Armenteros-Podolanski cut	$p_{\mathrm{T}}^{ARM} > 0.2\|\alpha\|$
reconstructed invariant mass	$0.480 < M_{\pi^+\pi^-} < 0.515$ GeV/c^2

Table 4.6: The cuts used on identified $\pi^+\pi^-$ pairs for K_s^0 reconstruction in Pb-Pb collisions at $\sqrt{s_{\mathrm{NN}}}$ = 2.76 TeV.

The invariant mass distribution of $\pi^+\pi^-$ pairs is obtained by considering the oppositely charged pions for MB events (0-80 % centrality) and is shown in Fig. 4.8. The K_s^0 extraction is performed by fitting the invariant mass distribution of $\pi^+\pi^-$ pairs by the following function,

$$f_{total}(M_{\pi^+\pi^-}) = f_{signal}(M_{\pi^+\pi^-}) + f_{bg}(M_{\pi^+\pi^-}), \tag{4.6}$$

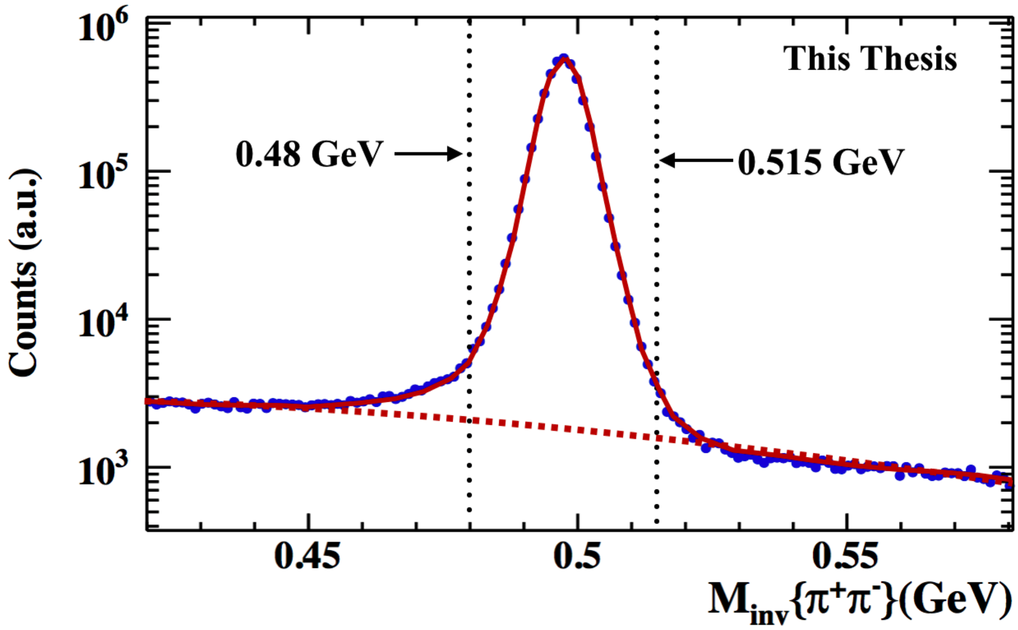

Figure 4.8: The invariant mass distribution of $\pi^+\pi^-$ pairs in Pb-Pb collisions at $\sqrt{s_{\rm NN}}$ = 2.76 TeV for minimum bias events.

where $f_{signal}(M_{\pi^+\pi^-})$ is given by a double Gaussian function as,

$$f_{signal} = A \times exp\left(-\left(\frac{(M_{\pi^+\pi^-} - m_1)^2}{2\sigma_{M_{\pi^+\pi^-}}} + \frac{(M_{\pi^+\pi^-} - m_2)^2}{2\sigma_{M_{\pi^+\pi^-}}}\right)\right), \tag{4.7}$$

where m_1 and m_2 are free parameters and have the dimension of mass. The background is described by a second order polynomial function (f_{bg}) given by,

$$f_{bg} = a_0 + a_1 \times M_{\pi^+\pi^-} + a_2 \times M^2_{\pi^+\pi^-}. \tag{4.8}$$

Fig. 4.9 shows the reconstructed invariant mass distribution of $\pi^+\pi^-$ pairs fitted with the f_{total} for different centrality bins. The contamination due to the random combination of $\pi^+\pi^-$ pairs appearing in the selected range ($0.48 < M_{\pi^+\pi^-} < 0.515$ GeV/c^2) is estimated by calculating the ratio of the number of background pairs to the sum of signal and background pairs,

$$Contamination(c) = Background/(Signal + Background), \tag{4.9}$$

where *Background* is the number of background pairs and is obtained by calculating the area under the f_{bg} function, whereas the $Signal + Background$ is estimated by calculating the area under f_{total} function in the range $0.48 < M_{\pi^+\pi^-} < 0.515$ GeV/c^2. The contamination percentage is shown in Table 4.7 for various centralities.

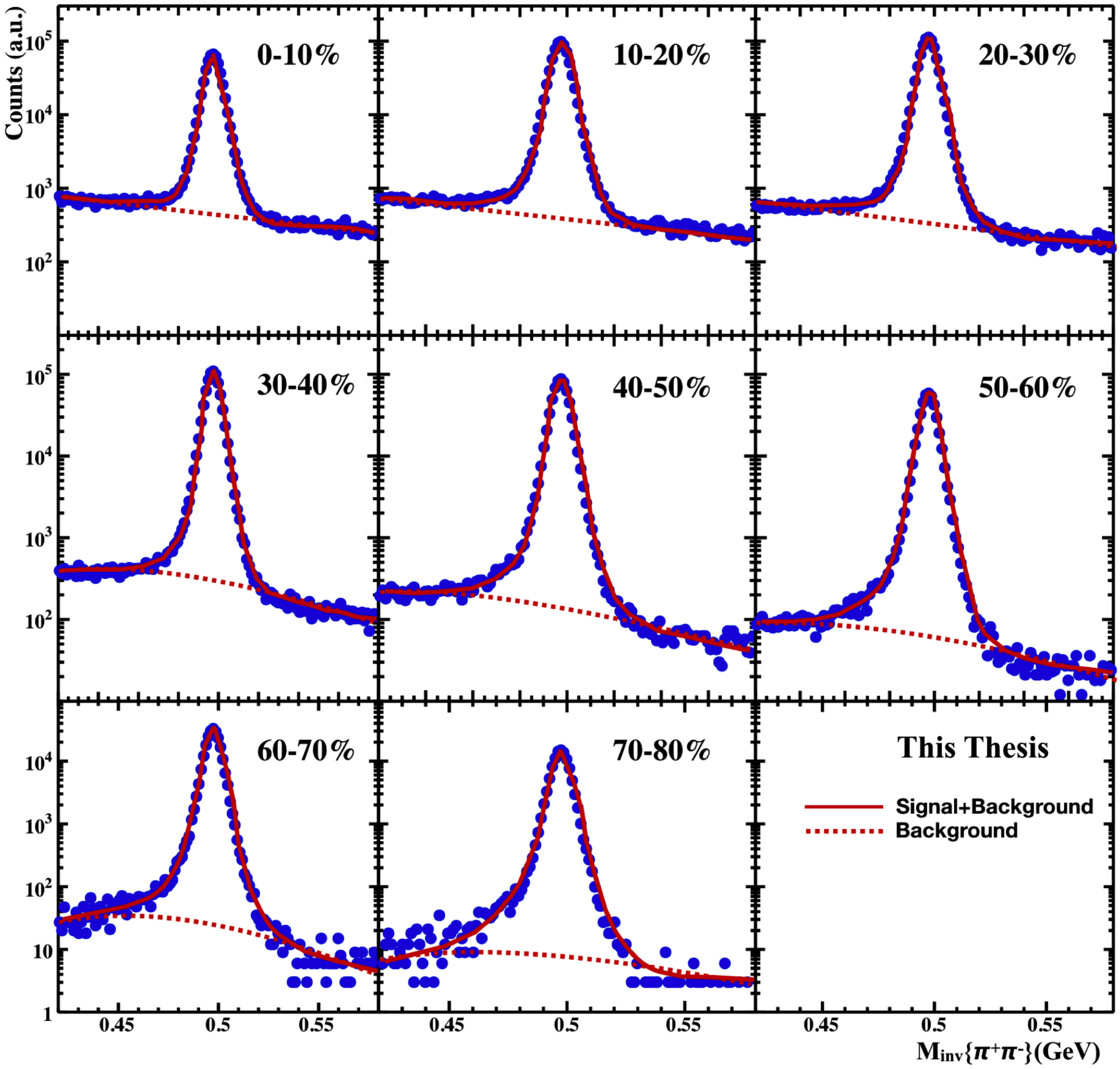

Figure 4.9: The invariant mass distribution of $\pi^+\pi^-$ pairs in Pb-Pb collisions at $\sqrt{s_{\rm NN}}$ = 2.76 TeV for various centrality classes.

Centrality(%)	Contamination(%)
0-10	3.76
10-20	3.41
20-30	2.19
30-40	2.02
40-50	1.69
50-60	1.61
60-70	1.48
70-80	1.31

Table 4.7: The value of contamination under the K^0_s signal region for various centralities in Pb-Pb collisions at $\sqrt{s_{\rm NN}}$ = 2.76 TeV.

The invariant mass distribution of $\pi^+\pi^-$ pairs is shown in Fig. 4.10 for five run number to check the variation of width with change in run number. This check was performed to study the impact of space charge effects and possible bias from background pions which can change the detection efficiency. The figure depicts that there is no discernible change in yields of the background and signal. The width of the distribution is also not varying, which confirms that there is no obvious impact from possible variation of the space charge effects for different runs.

4.6 Determination of ν_{dyn}

The K^0_ss and $K^\pm$s were selected after imposing various track cuts and topological cuts as described in the previous sections. The number of K^0_ss and $K^\pm$s were obtained on an event-by-event basis to calculate the $\nu_{dyn}[K^0_s, K^\pm]$ for each collision centrality. The yield of the K^0_ss and $K^\pm$s was corrected for the detection efficiency. The correction of background present in the K^0_s signal region has been accounted for as per the procedure described in section 4.8. Additionally, the $\nu_{dyn}[K^+, K^-]$ has been calculated to observe the effect of pair production. The expression of the correlator used for different combination of particles used in the analysis, given by,

$$\nu_{dyn}[K^0_s, K^\pm] = \frac{< N_{K^0_s}(N_{K^0_s} - 1) >}{< N_{K^0_s} >^2} + \frac{< N_{K^\pm}(N_{K^\pm} - 1) >}{< N_{K^\pm} >^2} - 2\frac{< N_{K^0_s} N_{K^\pm} >}{< N_{K^0_s} >< N_{K^\pm} >} \quad (4.10)$$

$$\nu_{dyn}[K^+, K^-] = \frac{< N_{K^+}(N_{K^+} - 1) >}{< N_{K^+} >^2} + \frac{< N_{K^-}(N_{K^-} - 1) >}{< N_{K^-} >^2} - 2\frac{< N_{K^+} N_{K^-} >}{< N_{K^+} >< N_{K^-} >}. \quad (4.11)$$

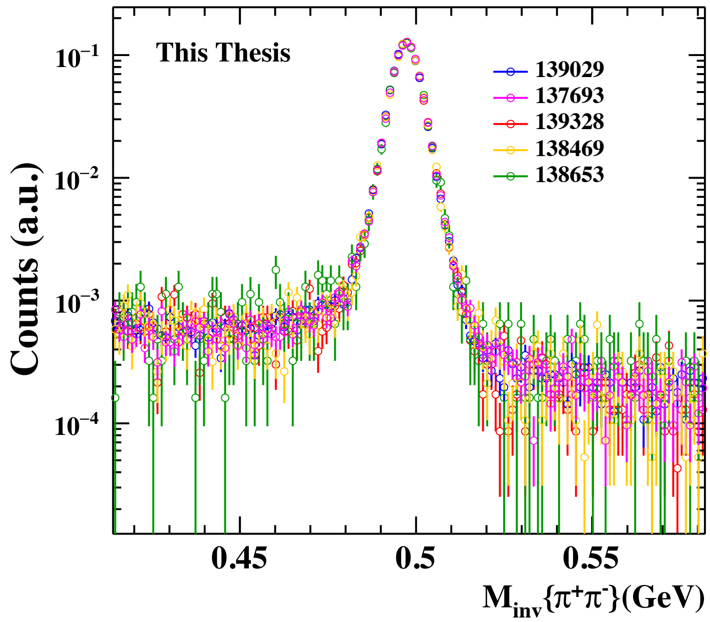

Figure 4.10: The invariant mass distribution of $\pi^+\pi^-$ pairs for 5 run numbers (0-80% centrality) in Pb-Pb collisions at $\sqrt{s_{NN}}$ = 2.76 TeV.

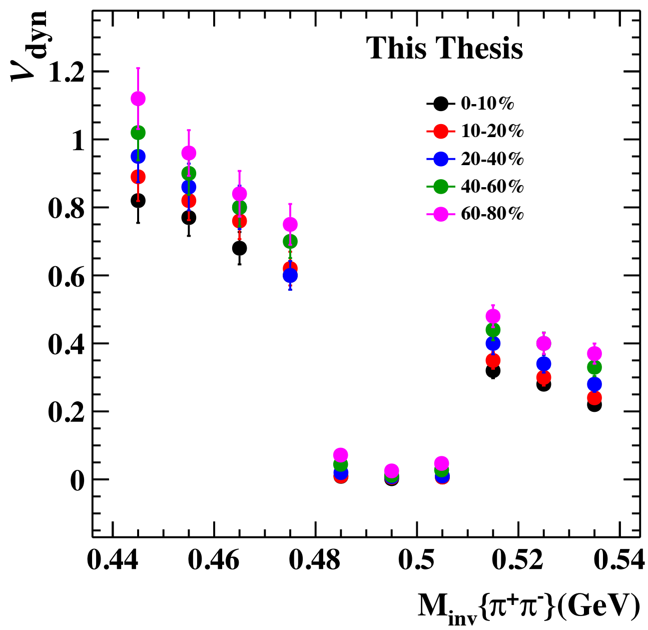

Figure 4.11: The variation of $\nu_{dyn}[K_s^0, K^{\pm}]$ as a function of invariant mass of $\pi^+\pi^-$ pairs in Pb-Pb collisions at $\sqrt{s_{NN}}$ = 2.76 TeV for various centrality classes.

4.6.1 Centrality Bin Width Correction

The values of obtained ν_{dyn} were corrected for finite bin width of selected centrality classes to minimise the effect of volume fluctuations. This correction is performed as per procedure mentioned in reference [62]. The wider centrality bin is further divided into 'n' number of narrower bins. The value of the correlator in the wider centrality bin is estimated as per following expression,

$$C = \frac{\sum_{r=1}^{n} n_r C^r}{\sum_{r=1}^{n} n_r} = \sum_{r=1}^{n} \omega_r C^r, \tag{4.12}$$

where n_r is the number of events in rth centrality bin and C^r correspond to the value of correlator in the rth centrality bin. The weight, ω_r, for a given rth centrality bin is $\omega_r = n_r/\sum n_r$. This method is employed to calculate the values of ν_{dyn} and to address the effect of variation of the volume within a wide centrality bin.

4.7 Efficiency Correction

The MC analysis is performed on events generated using dedicated HIJING simulation data. The acceptance×efficiency correction due to detector response and acceptance is defined for each $p_{\rm T}$ bin as $N_{\rm reconstructed}/N_{\rm generated}$, where $N_{\rm generated}$ refers to the number of $K^{\pm}$s (or K_s^0s) generated within pseudorapidity interval, $|\eta| < 0.5$, while $N_{\rm reconstructed}$ refers to the number of reconstructed $K^{\pm}$s (or K_s^0s) after passing through the selection criteria as used in real data analysis. Fig. 4.12 shows the basic distributions of kinematic observables such as $p_{\rm T}$, η and ϕ at generated and reconstructed level for $K^{\pm}$s, while the same is shown for K_s^0s in Fig. 4.13. These distributions are obtained for 0-80% centrality. The variation of the acceptance × efficiency (ϵ) for $K^{\pm}$ and K_s^0 as a function of $p_{\rm T}$, η, and ϕ obtained in 0-80% centrality is shown in Fig. 4.14, Fig. 4.15 and Fig. 4.16 respectively. The uncertainties in efficiency are calculated by using the Bayesian approach. It can be observed that, the efficiency factors are essentially independent of η and ϕ but show a considerable $p_{\rm T}$ dependence. Therefore, a $p_{\rm T}$ dependent efficiency correction is implemented for correcting the number of $K^{\pm}$s and K_s^0s.

The efficiency correction employs the following procedure. Let n_1, n_2, n_3, ...n_i be the number of uncorrected kaons associated with the $p_{\rm T}$ bins $p_{\rm T}1$, $p_{\rm T}2$, $p_{\rm T}3$, ...$p_{\rm T}i$ respectively. Let the efficiency factors corresponding to those $p_{\rm T}$ bins be ϵ_1, ϵ_2, ...ϵ_i and n_1^c, n_2^c, ...n_i^c be the number of kaons in those $p_{\rm T}$ bins after efficiency correction. The number of total kaons, N, after efficiency correction is given by,

$$N = \sum_i n_i^c \ \text{, where } \ n_i^c = \frac{n_i}{\epsilon_i}. \tag{4.13}$$

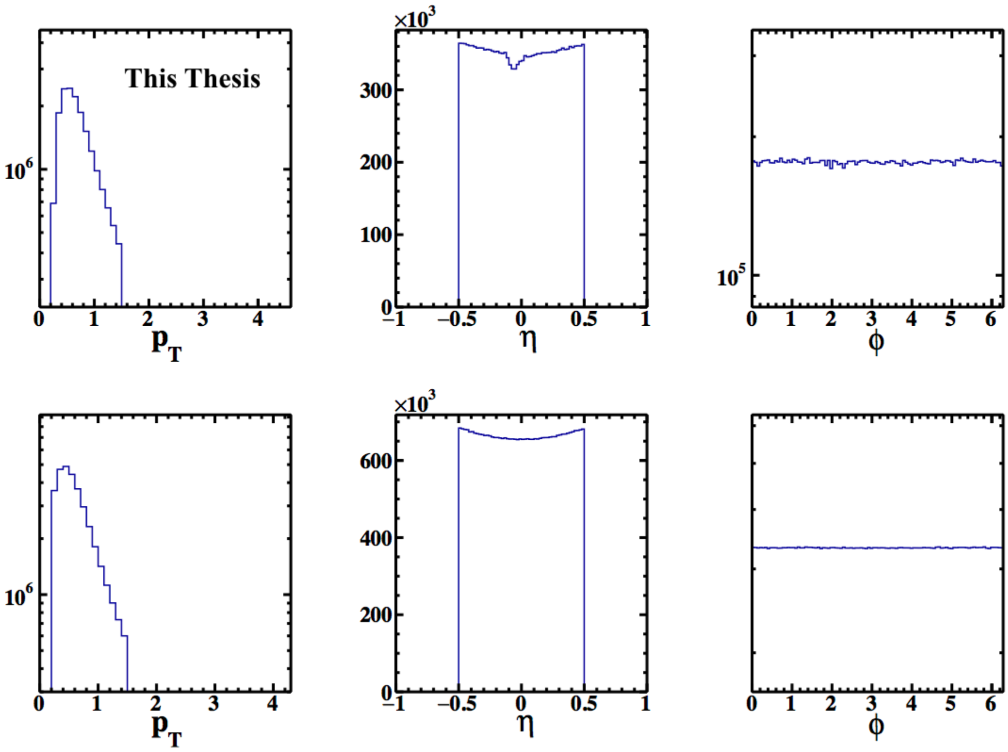

Figure 4.12: The transverse momentum (p_T), pseudorapidity (η) and azimuthal angle (ϕ) distribution of charged kaons in Pb-Pb collisions at $\sqrt{s_{\rm NN}}$ = 2.76 TeV, obtained from the reconstructed level (**Upper panels**) and generated level (**Bottom panels**) MC datasets.

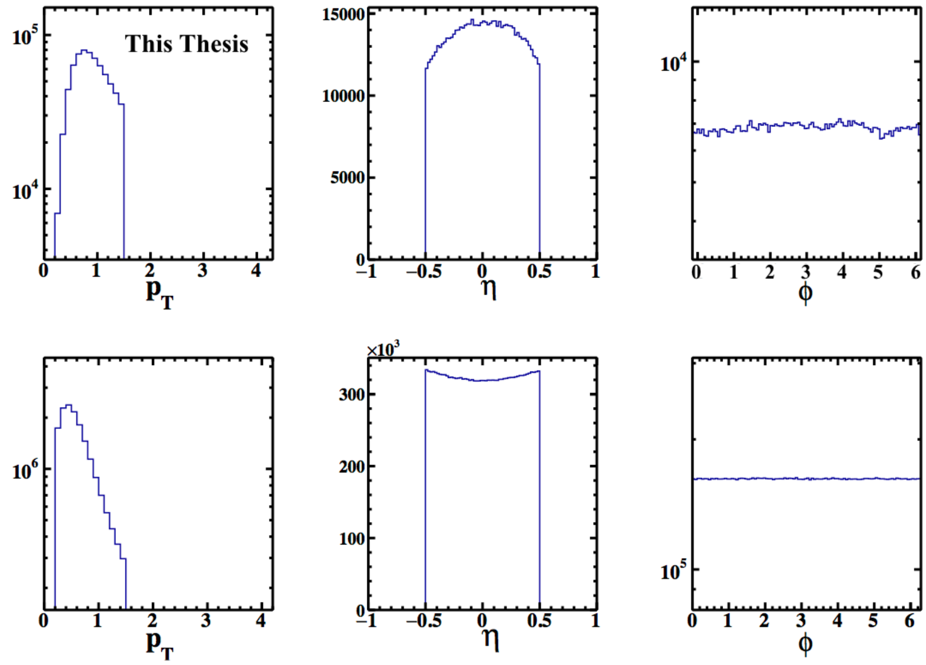

Figure 4.13: The transverse momentum (p_T), pseudorapidity (η) and azimuthal angle (ϕ) distribution of K_s^0 in Pb-Pb collisions at $\sqrt{s_{\mathrm{NN}}}$ = 2.76 TeV, obtained from the reconstructed level (**Upper panels**) and generated level (**Bottom panels**) MC datasets.

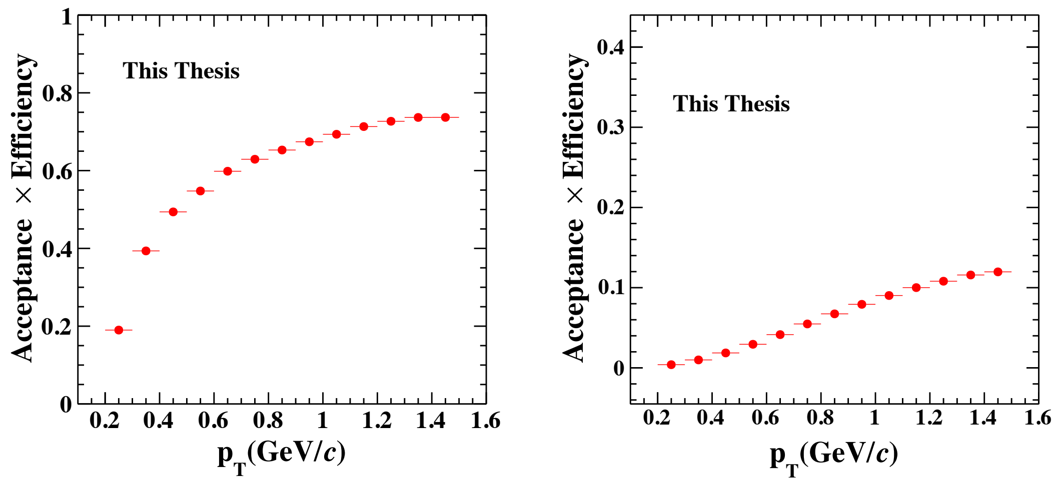

Figure 4.14: The variation of (Acceptance × Efficiency) as a function of transverse momentum obtained for $K^{\pm}$ (**Left panel**) and K_s^0 (**Right panel**) in MC dataset in Pb-Pb collisions at $\sqrt{s_{\mathrm{NN}}}$ = 2.76 TeV.

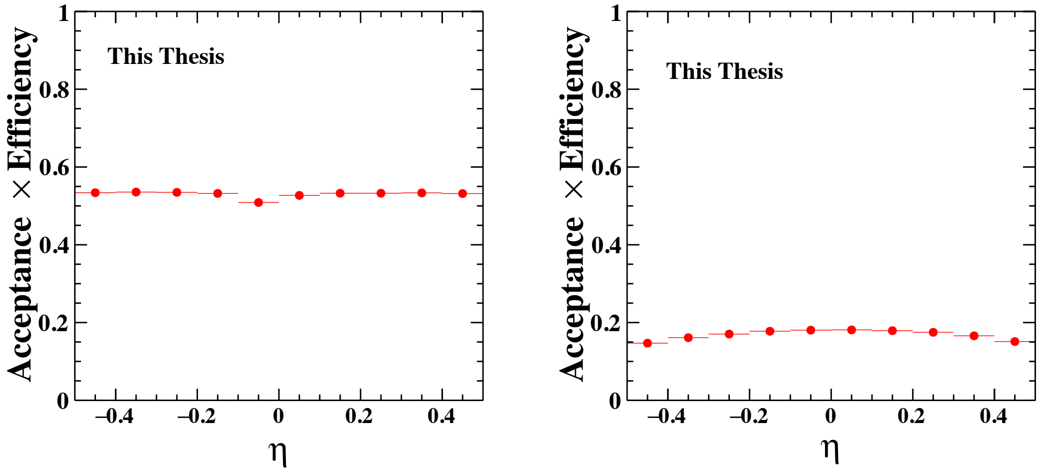

Figure 4.15: The variation of (Acceptance $\times$ Efficiency) as a function of pseudorapidity obtained for $K^{\pm}$(**Left panel**) and K_s^0 (**Right panel**) in MC dataset in Pb-Pb collisions at $\sqrt{s_{\mathrm{NN}}}$ = 2.76 TeV.

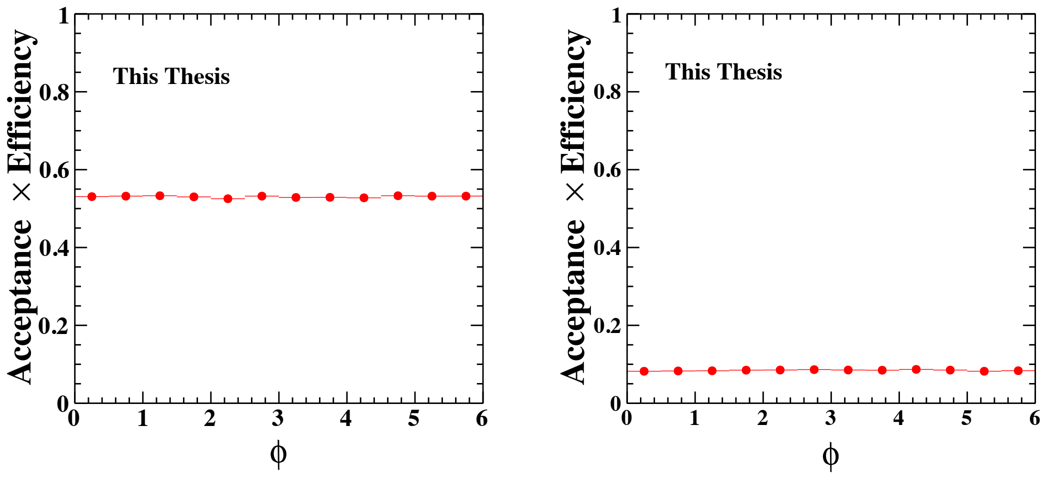

Figure 4.16: The variation of (Acceptance $\times$ Efficiency) as a function of azimuthal angle obtained for $K^{\pm}$(**Left panel**) and K_s^0 (**Right panel**) in MC dataset in Pb-Pb collisions at $\sqrt{s_{\mathrm{NN}}}$ = 2.76 TeV.

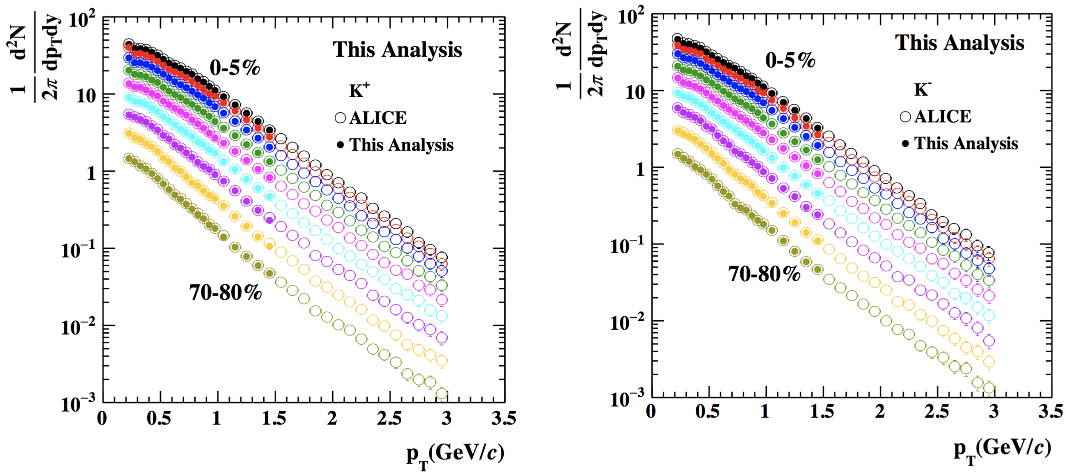

Figure 4.17: The comparison of the p_{T} spectra of K^+ (**Left panel**) and K^- (**Right panel**) with the measured ALICE data [63] for various centrality classes.

The corrected yields of K^+s and K^-s are obtained as a function of p_{T}, for various centrality bins to compare with the published spectra of $K^{\pm}$s [63]. The measured kaon yields are in good agreement with the published data [63] within systematic uncertainties, and is shown in Fig. 4.17. The corrected yields of K_s^0s are obtained as a function of p_{T}, for various centrality bins to compare with the published measured data and is shown in Fig. 4.18. Fig. 4.19 compares the value of $\nu_{dyn}[K_s^0, K^{\pm}]$ with and without efficiency correction. The values agree with each other within statistical uncertainties, which show that $\nu_{dyn}[K_s^0, K^{\pm}]$ is robust against detector inefficiency.

4.8 Background Correction

The values of $\nu_{dyn}[K_s^0, K^{\pm}]$ can be affected by the presence of random $\pi^+\pi^-$ pairs in the K_s^0 signal regions. These $\pi^+\pi^-$ pairs which are identified as K_s^0s, contaminate the K_s^0 signals and serve as combinatorial background in the signal regions. The influence of combinatorial background is studied by calculating the $\nu_{dyn}[K_s^0, K^{\pm}]$ in different bins of $\pi^+\pi^-$ invariant mass spectra. The variation of $\nu_{dyn}[K_s^0, K^{\pm}]$ as a function of $M_{\pi^+\pi^-}$ pairs is shown in Fig. 4.11 for different centralities. As can be observed from the figure, the values of $\nu_{dyn}[K_s^0, K^{\pm}]$ in the signal region are significantly lower than the ones in the side band background regions. This trend is observed to be consistent for all centralities. As the value of $\nu_{dyn}[K_s^0, K^{\pm}]$ is sensitive to the selected invariant mass region, it is thus necessary to correct the values of $\nu_{dyn}[K_s^0, K^{\pm}]$ for such contamination in the signal region. The quantitative estimation of background from side band regions is performed according to the procedure described below. Since the number of background pairs, N_b, under signal

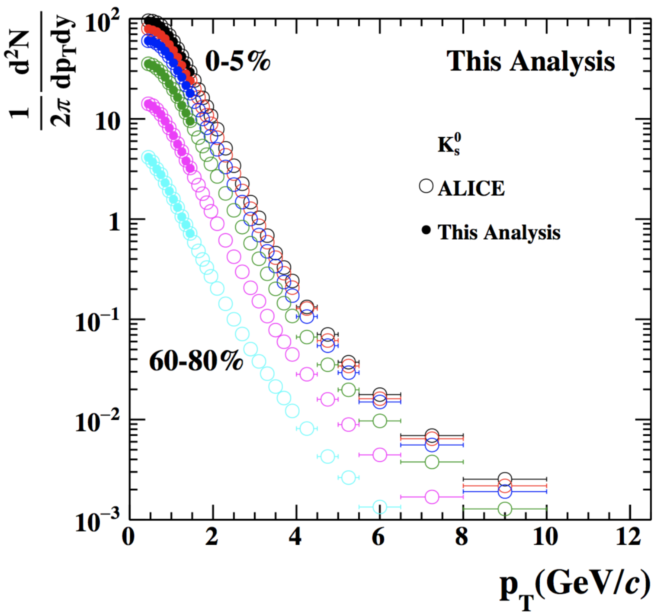

Figure 4.18: The comparison of the p_{T} spectra of K^0_s with the measured ALICE data [64] for various centrality classes.

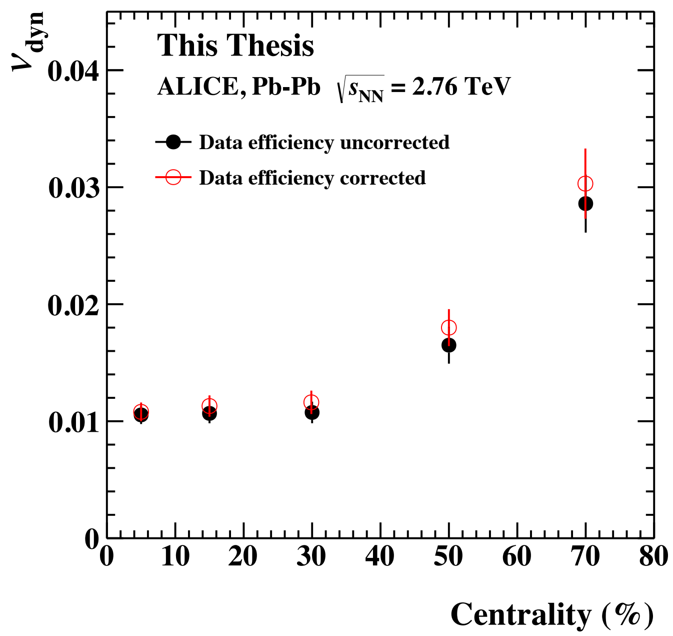

Figure 4.19: The variation of $\nu_{dyn}[K^0_s, K^{\pm}]$ as a function of centrality w/ and w/o efficiency correction in Pb-Pb collisions at $\sqrt{s_{\mathrm{NN}}}$ = 2.76 TeV.

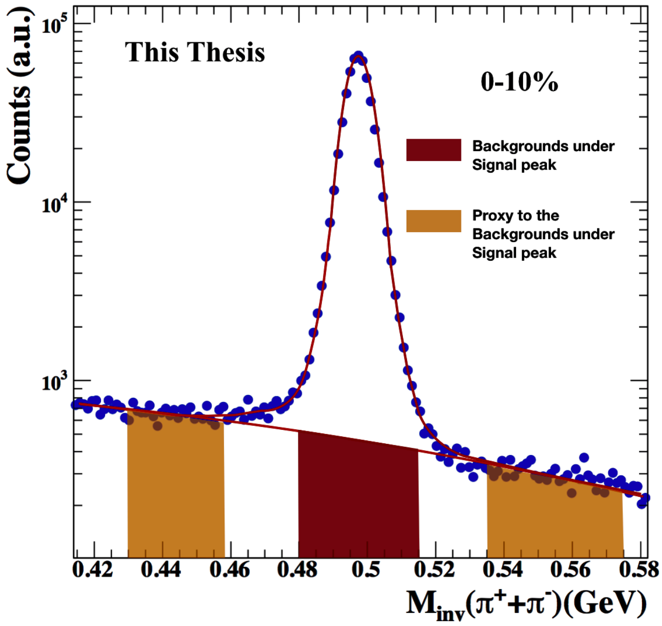

Figure 4.20: The invariant mass distribution of $\pi^+\pi^-$ pairs for 0-10% centrality in Pb-Pb collisions at $\sqrt{s_{NN}}$ = 2.76 TeV. The coloured band refers to the region selected for background calculation.

peak is not directly accessible, the combinatorial pairs in the side band regions (0.430 $< M_{\pi^+\pi^-} <$ 0.460 GeV/c^2 in the left side band and 0.540 $< M_{\pi^+\pi^-} <$ 0.575 GeV/c^2 in the right side band) are used as proxies for background pairs in the accepted mass range (0.480 $< M_{\pi^+\pi^-} <$ 0.515 GeV/c^2). The selection of side band regions for estimating the N_b is based on the number of background pairs under the signal region calculated from the estimated contamination. The reconstruction of K_s^0 based on topological cuts is subject to a combinatorial $\pi^+\pi^-$ pairs contamination ranging from 1.3% in peripheral collisions to 3.8% in central collisions, as illustrated in Table 4.7. The event-by-event fluctuations of this combinatorial background might increase the K_s^0 variance and might potentially bias the charged-neutral covariance term. Fig. 4.20 shows the signal and background regions of K_s^0 for 0-10% centrality. The contribution of the background from side band regions on ν_{dyn} values are calculated according to the procedure described below.

Let N_c = Number of $K^{\pm}$s.

N_s = Number of signal pairs under K_s^0 peak.

N_b = Number of background pairs.

$N_0 = N_s + N_b$.

Let ρ^0, ρ^s and ρ^b be the mean of N_0, N_s and N_b distributions, respectively and the corresponding second order moments are denoted by ρ^{00}, ρ^{ss} and ρ^{bb}.

$$\rho^{0} = \rho^{s} + \rho^{b} \tag{4.14}$$

$$\rho^{00} = \rho^{ss} + \rho^{bb} + 2\rho^{sb}. \tag{4.15}$$

From Eq. 4.14, the 2^{nd} moment, ρ^{0b} is defined as,

$$\rho^{0b} = \rho^{sb} + \rho^{bb} \tag{4.16}$$

$$=> \rho^{sb} = \rho^{0b} - \rho^{bb}. \tag{4.17}$$

The expression of ρ^{00} after using Eq. 4.17 in Eq. 4.15 is,

$$\rho^{00} = \rho^{ss} + \rho^{bb} + 2\left(\rho^{0b} - \rho^{bb}\right) \tag{4.18}$$

$$=> \rho^{ss} = \rho^{00} + \rho^{bb} - 2\rho^{0b} \tag{4.19}$$

$$\frac{\rho^{ss}}{\rho^{s}\rho^{s}} = \frac{\rho^{00}}{\rho^{s}\rho^{s}} + \frac{\rho^{bb}}{\rho^{s}\rho^{s}} - 2\frac{\rho^{0b}}{\rho^{s}\rho^{s}} \tag{4.20}$$

$$= \frac{\rho^{00}}{\rho^{0}\rho^{0}}\frac{\rho^{0}\rho^{0}}{\rho^{s}\rho^{s}} + \frac{\rho^{bb}}{\rho^{b}\rho^{b}}\frac{\rho^{b}\rho^{b}}{\rho^{s}\rho^{s}} - 2\frac{\rho^{0b}}{\rho^{0}\rho^{b}}\frac{\rho^{0}\rho^{b}}{\rho^{s}\rho^{s}}. \tag{4.21}$$

Let f = ρ^{b}/ρ^{0} be the contamination. Therefore, it can be written as,

$$\frac{\rho^{0}}{\rho^{s}} = 1/(1-f), \tag{4.22}$$

and

$$\frac{\rho^{b}}{\rho^{s}} = f/(1-f). \tag{4.23}$$

Using these expression of ratios,

$$\rho^{ss}/\rho^{s}\rho^{s} = \frac{< N_s(N_s-1) >}{< N_s >^2} \tag{4.24}$$

$$= \frac{1}{(1-f)^2}\frac{< N_0(N_0-1) >}{< N_0 >^2} - \frac{2f}{(1-f)^2}\frac{< N_0N_b >}{< N_0 >< N_b >} + \frac{f^2}{(1-f)^2}\frac{< N_b(N_b-1) >}{< N_b >^2}. \tag{4.25}$$

$$\rho^{sc}/\rho^{s}\rho^{c} = \frac{< N_sN_c >}{< N_s >< N_c >} \tag{4.26}$$

$$= \frac{1}{(1-f)}\frac{< N_0N_c >}{< N_0 >< N_c >} - \frac{f}{(1-f)}\frac{< N_bN_c >}{< N_b >< N_c >}. \tag{4.27}$$

$$\rho^{cc}/\rho^{c}\rho^{c} = \frac{< N_c(N_c-1) >}{< N_c >^2}. \tag{4.28}$$

The combined expressions of the variance terms give,

$$\nu_{dyn}^{corrected} = \frac{< N_c(N_c-1) >}{< N_c >^2} + \frac{< N_s(N_s-1) >}{< N_s >^2} - 2\frac{< N_sN_c >}{< N_s >< N_c >}, \tag{4.29}$$

$$\nu_{dyn}^{measured} = \frac{< N_c(N_c-1) >}{< N_c >^2} + \frac{< N_0(N_0-1) >}{< N_0 >^2} - 2\frac{< N_0N_c >}{< N_0 >< N_c >}, \tag{4.30}$$

where $\nu_{dyn}^{corrected}$ is the value of ν_{dyn} after accounting for background correction, and $\nu_{dyn}^{measured}$ is the value of ν_{dyn} without background correction. The variance, covariance and the background fraction are calculated for all centrality classes for left and right side bands, and the values are shown in Table 4.8 and Table 4.9. Fig.4.21 depicts the corrected

Centrality	0-10%	10-20%	20-40%	40-60%	60-80%
f = N_b/N_0	0.03756	0.03402	0.0211	0.0165	0.0139
$< N_b(N_b-1) > / < N_b >^2$	1.27377	1.56925	1.96528	2.63022	21.0824
$< N_c(N_c-1) > / < N_c >^2$	1.01501	1.01792	1.0712	1.1151	1.245
$< N_0(N_0-1) > / < N_0 >^2$	1.01631	1.01758	1.07682	1.1301	1.261
$< N_bN_0 > / < N_b >< N_0 >$	1.07252	1.13194	1.26304	1.56674	2.33141
$< N_0N_c > / < N_0 >< N_c >$	1.0104	1.0126	1.06869	1.1132	1.2387
$< N_bN_c > / < N_b >< N_c >$	1.01859	1.07857	1.18015	1.47524	2.07794
$< N_s(N_s-1) >< N_s >^2$	1.01215	1.01303	1.06903	1.11563	1.23434
$< N_sN_c > / < N_s >< N_c >$	1.01008	1.01328	1.0559	1.10713	1.22687
$\nu_{dyn}^{corrected}$	0.00699	0.00729	0.00843	0.016473	0.02559
$\nu_{dyn}^{measured}$	0.01051	0.01030	0.0106	0.0188	0.0286
$\frac{\lvert\nu_{dyn}^{corrected}-\nu_{dyn}^{measured}\rvert}{\nu_{dyn}^{measured}} \times 100$	33%	29.2%	20.74%	12.37%	10.5%

Table 4.8: The values of variance, covariance, background fraction and $\nu_{dyn}[K_s^0, K^{\pm}]$ calculated on the left side band of the signal region.

and measured values of $\nu_{dyn}[K_s^0, K^{\pm}]$ for all centralities. It can be observed that, after correction the values of $\nu_{dyn}[K_s^0, K^{\pm}]$ decreased from 8% in peripheral collisions to 33% in central collisions.

4.9 Monte Carlo Closure Test

An MC closure test has been performed considering the $\nu_{dyn}[K_s^0, K^{\pm}]$ values of both the generator and reconstructed level of HIJING. The analysis and correction procedures performed in reconstructed MC data are exactly similar to the one performed in experimental measured data. The values obtained at the generated level and reconstructed level should have good agreement after implementing corrections due to the detector inefficiencies and contamination at the reconstructed level. The closure test is done to ensure that the analysis is not biased by the detector effects. Fig. 4.22 shows the invariant mass distribution of $\pi^+\pi^-$ pairs obtained using HIJING reconstructed data for 0-10% centrality bin. The background correction procedure has been implemented and the values of background fraction

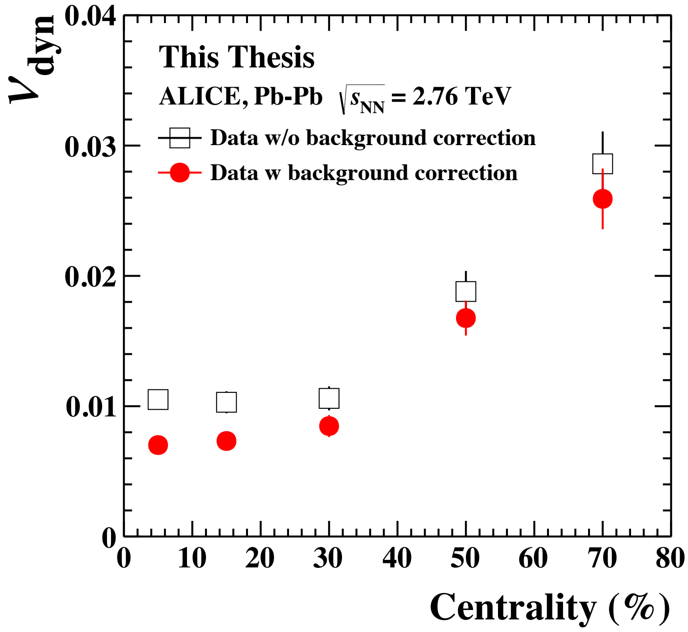

Figure 4.21: The variation of $\nu_{dyn}[K_s^0, K^{\pm}]$ as a function of centrality w/ and w/o background correction in Pb-Pb collisions at $\sqrt{s_{\mathrm{NN}}}$ = 2.76 TeV.

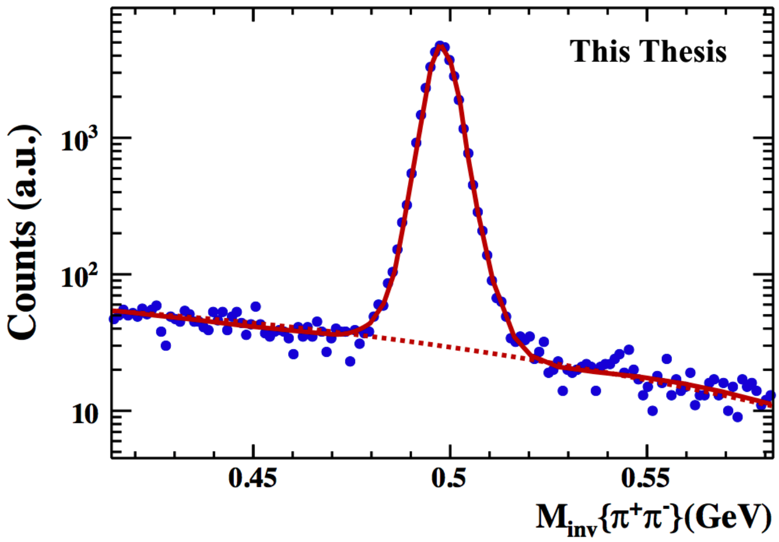

Figure 4.22: The invariant mass distribution of $\pi^+\pi^-$ pairs in Pb-Pb collisions at $\sqrt{s_{\mathrm{NN}}}$ = 2.76 TeV, obtained from MC data.

Centrality	0-10%	10-20%	20-40%	40-60%	60-80%
f = N_b/N_0	0.03764	0.03407	0.02115	0.01654	0.01396
$< N_b(N_b-1) > / < N_b >^2$	1.15577	1.80982	1.94753	2.11387	19.3271
$< N_c(N_c-1) > / < N_c >^2$	1.01501	1.01792	1.0712	1.1151	1.245
$< N_0(N_0-1) > / < N_0 >^2$	1.01631	1.01758	1.07682	1.1301	1.261
$< N_b N_0 > / < N_b >< N_0 >$	1.069503	1.08247	1.27601	1.19121	1.4003
$< N_0 N_c > / < N_0 >< N_c >$	1.0104	1.0126	1.06869	1.1132	1.2387
$< N_b N_c > / < N_b >< N_c >$	1.01853	1.18249	1.34359	1.92190	2.93196
$< N_s(N_s-1) >< N_s >^2$	1.0122	1.01521	1.06288	1.11461	1.23334
$< N_s N_c > / < N_s >< N_c >$	1.01004	1.01113	1.05578	1.10633	1.22605
$\nu_{dyn}^{corrected}$	0.007046	0.00737	0.008524	0.017055	0.02623
$\nu_{dyn}^{measured}$	0.01051	0.01030	0.0106	0.0188	0.0286
$\frac{\lvert\nu_{dyn}^{corrected}-\nu_{dyn}^{measured}\rvert}{\nu_{dyn}^{measured}} \times 100$	33.02%	28.41%	19.84%	9.28%	8.27%

Table 4.9: The values of variance, covariance, background fraction and $\nu_{dyn}[K_s^0, K^{\pm}]$ calculated on the right side band of the signal region.

and the corresponding correction factor are shown in Table 4.10. Fig. 4.23 compares the values of $\nu_{dyn}[K_s^0, K^{\pm}]$ as a function of centrality for both generated and reconstructed level in the upper panel and their ratios are plotted with centrality in the bottom panels. This figure indicates that the background-corrected values differ by 2-5% from the generated ones, while the values which are not background-corrected significantly differs from the generated ones. Therefore, background correction is required to obtain meaningful results.

Centrality	0-10%	10-20%	20-40%	40-60%	60-80%
f = N_b/N_0	0.0256	0.02072	0.01355	0.00569	0.00163
Correction	21.01%	18.75%	11.41%	3.67%	1.21%
$\nu_{dyn}^{Measured}$ HIJING reco	0.00048	0.00077	0.0014	0.00266	0.0116
$\nu_{dyn}^{Corrected}$ HIJING reco	0.000379	0.00064	0.001245	0.002566	0.01146
ν_{dyn} HIJING true	0.000368	0.000615	0.00122	0.0025	0.0112
$\nu_{dyn}^{Corrected}$ reco/ ν_{dyn} true	2.7%±2%	4.0%±2.3%	2.0%±1.7%	3.0%±2.4%	2.0%±2.1%

Table 4.10: The background correction factor obtained from the MC datasets for various centralities in Pb-Pb collisions at $\sqrt{s_{NN}}$ = 2.76 TeV.

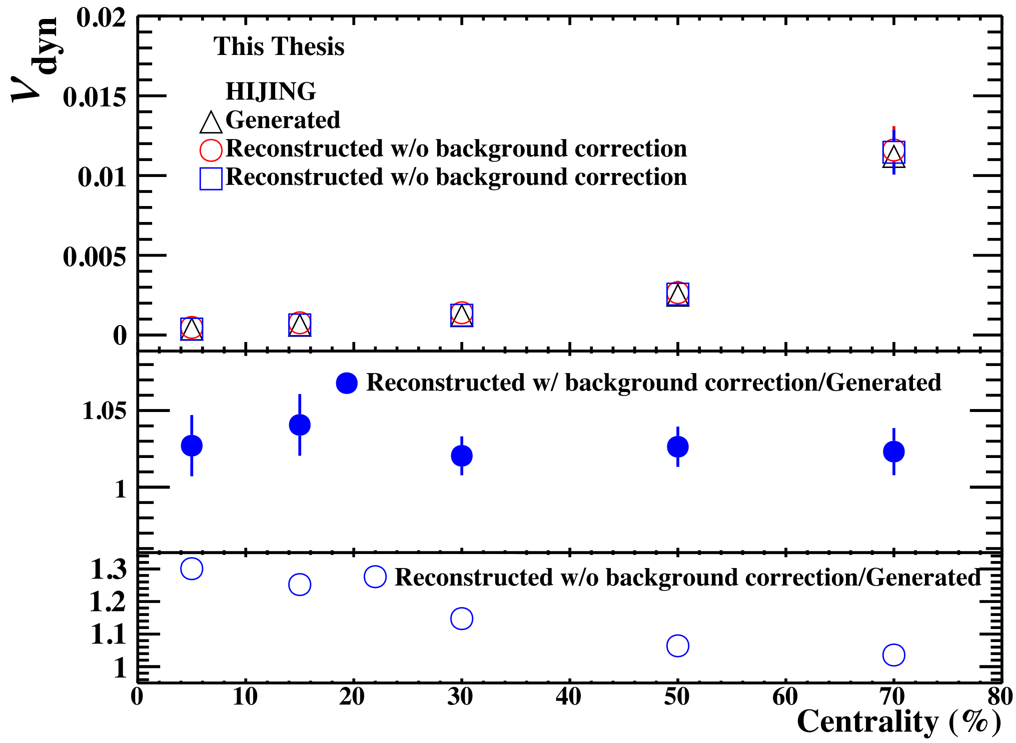

Figure 4.23: **Upper panel**: The variation of $\nu_{dyn}[K_s^0, K^{\pm}]$ with centrality obtained from MC for HIJING calculations. **Middle panel**: The ratio of $\nu_{dyn}[K_s^0, K^{\pm}]$ for reconstructed (background-corrected) to generated MC calculations as a function of centrality. **Bottom panel**: The ratio of $\nu_{dyn}[K_s^0, K^{\pm}]$ for reconstructed (background-uncorrected) to generated MC calculations as a function of centrality in Pb-Pb collisions at $\sqrt{s_{\rm NN}}$ = 2.76 TeV.

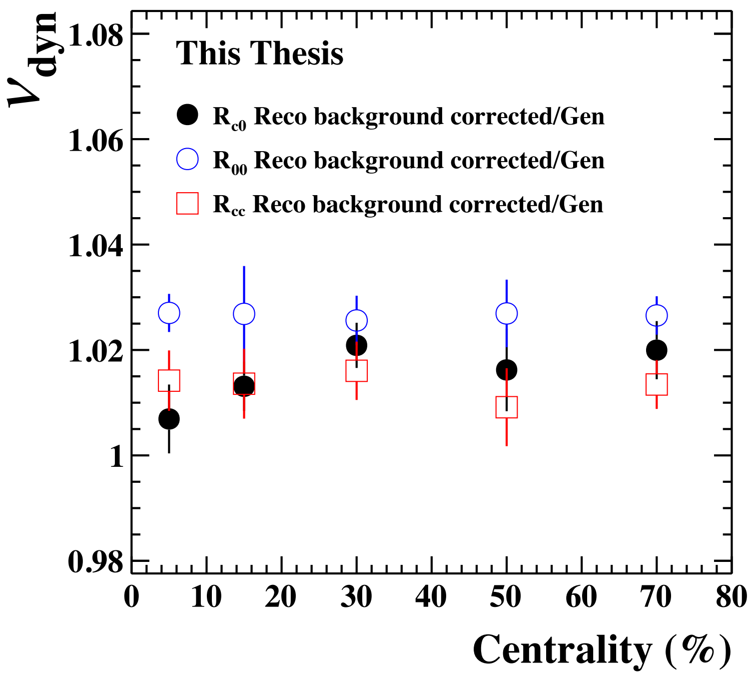

Figure 4.24: The ratio (reconstructed/generated) of the individual terms of $\nu_{dyn}[K_s^0, K^{\pm}]$ as a function of centrality with background correction obtained from MC estimation in Pb-Pb collisions at $\sqrt{s_{\mathrm{NN}}}$ = 2.76 TeV.

The slight difference between the generated and the reconstructed (background corrected) values can be understood by studying the individual terms in the expression of $\nu_{dyn}[K_s^0, K^{\pm}]$. The ratio of the individual terms (reconstructed/generated) as a function of centrality is shown in Fig. 4.24. As can be observed from the figure, the charge and neutral variance terms seem to have no centrality dependence within statistical uncertainties. However, the values are slightly lower for charged-neutral covariance term for most central collisions.

4.10 $\langle N \rangle$ and $\langle p_T \rangle$ vs Run Numbers

In this section, mean multiplicity, $\langle N \rangle$ and mean transverse momentum, $\langle p_T \rangle$ of kaons (K^+, K^- and K_s^0) are studied for all run numbers for most central collisions (0-10% centrality) to check the possible effect of biases from particle selection. The values of $\langle N \rangle$ and $\langle p_T \rangle$ obtained for different run numbers are shown in Fig. 4.25 and 4.26, respectively. The solid line in the figures shows the weighted average of $\langle N \rangle$. The standard deviation for the same for all run numbers is shown by the dashed line in the figure. The run numbers for which $\langle N \rangle$ (and $\langle p_T \rangle$) is beyond 1σ are excluded. 12 run numbers are excluded

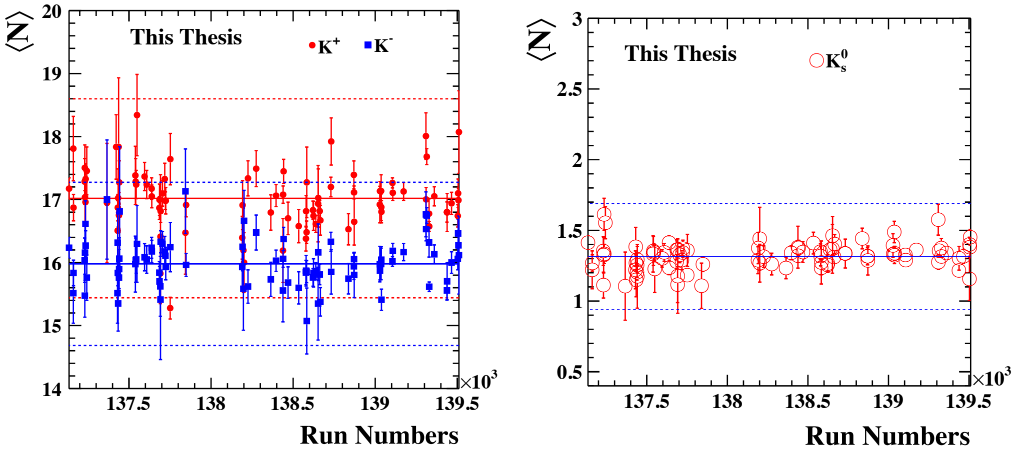

Figure 4.25: **Left panel**: The values of $\langle N_{K^+}\rangle$ and $\langle N_{K^-}\rangle$ for various run numbers obtained for 0-10% centrality. **Right panel**: The values of $\langle N_{K_s^0}\rangle$ for various run numbers in Pb-Pb collisions at $\sqrt{s_{\rm NN}}$ = 2.76 TeV obtained for 0-10% centrality.

from the dataset. Fig.4.27 compares the variation of $\nu_{dyn}[K_s^0, K^{\pm}]$ with (and without) the excluded run numbers with centrality. The values seem to agree with each other within uncertainties. Fig. 4.28 shows the scatter plot of $\langle N_{K_s^0}\rangle$s with $\langle N_{K^{\pm}}\rangle$s. The figure indicates that there is no obvious correlation between $\langle K_s^0\rangle$s and $\langle K^{\pm}\rangle$s obtained for different run numbers.

4.11 Estimation of Experimental Uncertainty

Each experimental measurement is associated with two types of uncertainties: statistical and systematic.

4.11.1 Determination of Statistical Uncertainty

The sub-sample method has been used to determine the statistical uncertainty. In this method, the considered dataset is divided into 'n' number of sub-samples randomly with approximately equal number of events in each sample. The analysis is performed on each sub-sample independently. The error in ν_{dyn} was obtained by estimating the standard deviation of the values obtained in sub-samples. This method is employed for each centrality bin.

$$\sigma_{<\nu_{dyn}>} = \frac{\sigma}{\sqrt{n}}, \tag{4.31}$$

where

$$\sigma = \sqrt{\frac{\sum_{i=1}^{n}(\nu_{dyn,i} - <\nu_{dyn}>)^2}{n-1}} \tag{4.32}$$

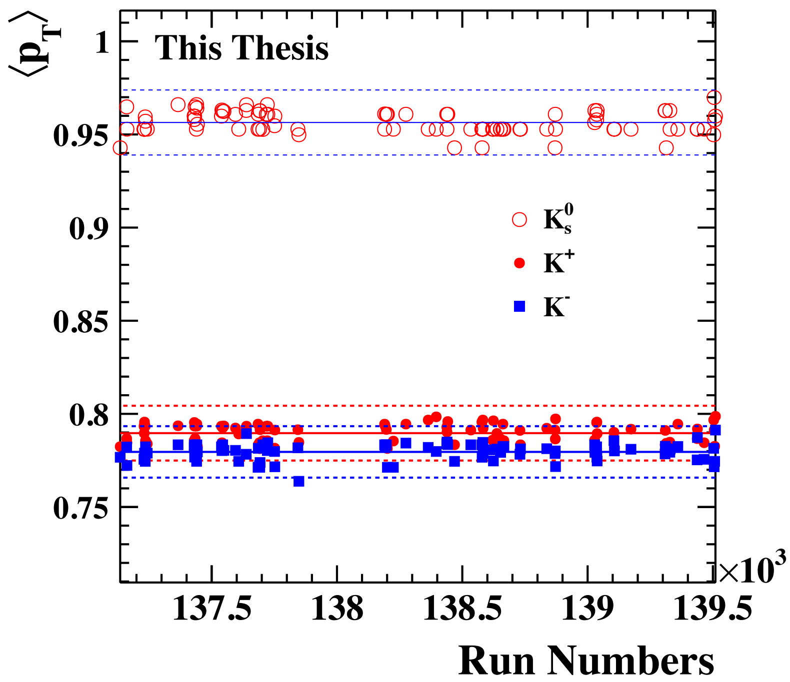

Figure 4.26: The $\langle p_{\rm T}\rangle$ of K^{+}s, K^{-}s and K_{s}^{0}s for various run numbers in Pb-Pb collisions at $\sqrt{s_{\rm NN}}$ = 2.76 TeV for 0-10% centrality.

$$< \nu_{dyn} >= \frac{1}{n}\sum_{i=1}^{n}\nu_{dyn,n}, \tag{4.33}$$

where $\nu_{dyn,i}$ is the the value of ν_{dyn} in ith sub-sample.

4.11.2 Determination of Systematic Uncertainty

There can be systematic uncertainty due to variation in event selection, track selection and experimental procedures. The possible sources of systematic uncertainties also include biases associated with the presence of secondary particles in the accepted sample and non-uniformities of the detection efficiency. The analysis procedure is performed with the identified systematic sources and the uncertainty is evaluated after comparing to the default measurement. The method is described as follows.

- The default values are the set of selection parameters used for the baseline measurement.
- A set of systematic sources are identified and the ν_{dyn} values are obtained by varying those sources.

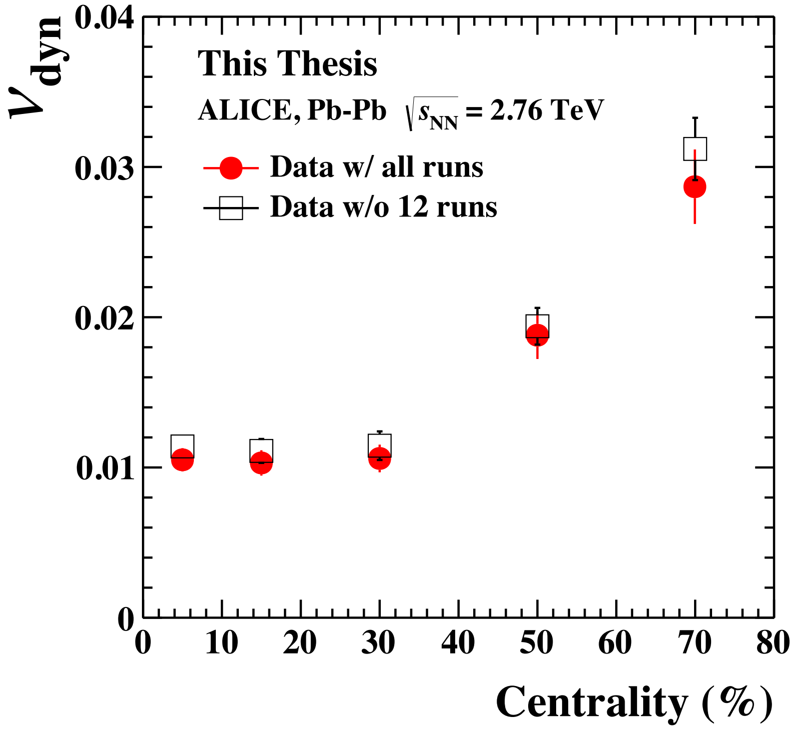

Figure 4.27: The comparison of $\nu_{dyn}[K_s^0, K^{\pm}]$ with centrality w/ and w/o excluded run numbers in Pb-Pb collisions at $\sqrt{s_{\rm NN}}$ = 2.76 TeV.

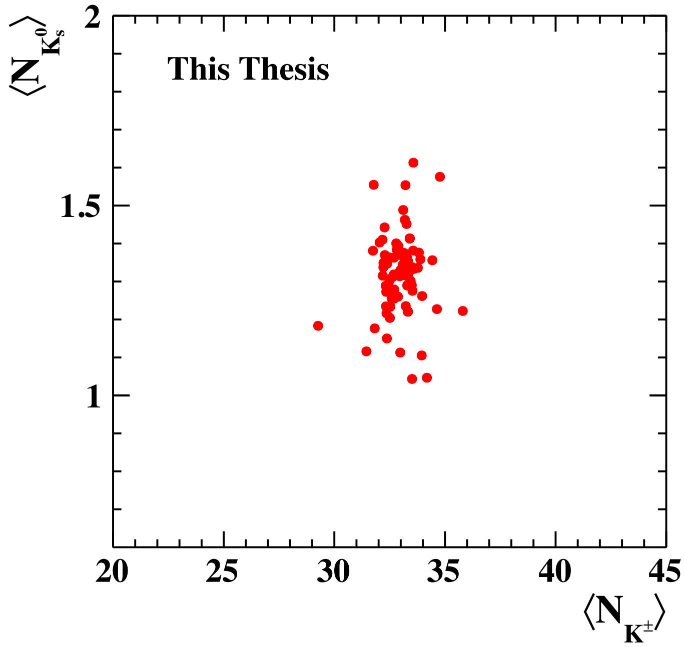

Figure 4.28: The variation of $\langle K_s^0 \rangle$s with $\langle K^{\pm} \rangle$s for all run numbers in Pb-Pb collisions at $\sqrt{s_{\rm NN}}$ = 2.76 TeV.

- For an identified source of error, if two or more variation of parameters are chosen, the RMS value is calculated to estimate the systematic uncertainty.
- In this analysis, the various sources of systematic uncertainties are assumed to be uncorrelated and thus values obtained are added in quadrature to obtain the total systematic uncertainty from all sources.

Cuts	Default values	varied
$\|V_z\|$	< 10 cm	±2
decay length	$< 3c\tau$	$\pm 1c\tau$
Cos(PA)	> 0.99	±0.002
Armenteros-Podolanski	> 0.2	±0.03
$\|\eta\|$	< 0.5	0.3, -0.5 < η < 0, 0 < η < 0.5
p_{T}	0.2-1.5 (GeV/c)	0.2< p_{T} <0.6, 0.6< p_{T} <1.5(GeV/c)
PID $\|n\sigma\|_k$	-0.5< $\|n\sigma\|_k$ <2.0	-2.0< $\|n\sigma\|_k$ < 2.0
K_s^0 inv. mass	1.5σ	±0.5σ

Table 4.11: The variation of cuts implemented for systematic studies in Pb-Pb collisions at $\sqrt{s_{\mathrm{NN}}}$ = 2.76 TeV.

Centrality(%)	0-10	10-20	20-40	40-60	60-80
Statistical	0.000781	0.000843	0.000921	0.00158	0.00248
Cos(PA)	0.00035	0.00041	0.00051	0.00068	0.0011
Armenteros-Podolanski	0.00023	0.00031	0.00042	0.00062	0.0013
PID $\|n\sigma\|_k$	0.00021	0.00029	0.00039	0.00055	0.00134
K_s^0 inv. mass	0.0001445	0.00027	0.00039	0.00067	0.0012
Event Outliers	0.0001	0.00021	0.00027	0.00041	0.0008
Decay radius	0.000221	0.0003	0.0004	0.00054	0.0012
Side band correction ν_{dyn}	0.0000685	0.00007	0.00009	0.00012	0.00018
K_s^0 invariant mass	0.00014	0.000126	0.000143	0.000180	0.0002
Decay length	0.000264	0.0003066	0.00034	0.000411	0.000625
$\|V_z\|$	0.000284	0.0003166	0.00035	0.000551	0.00065
Total	0.00087	0.0011	0.0013	0.0025	0.00415

Table 4.12: The values of the systematic uncertainty for $\nu_{dyn}[K_s^0, K^{\pm}]$ in Pb-Pb collisions at $\sqrt{s_{\mathrm{NN}}}$ = 2.76 TeV obtained for various centralities.

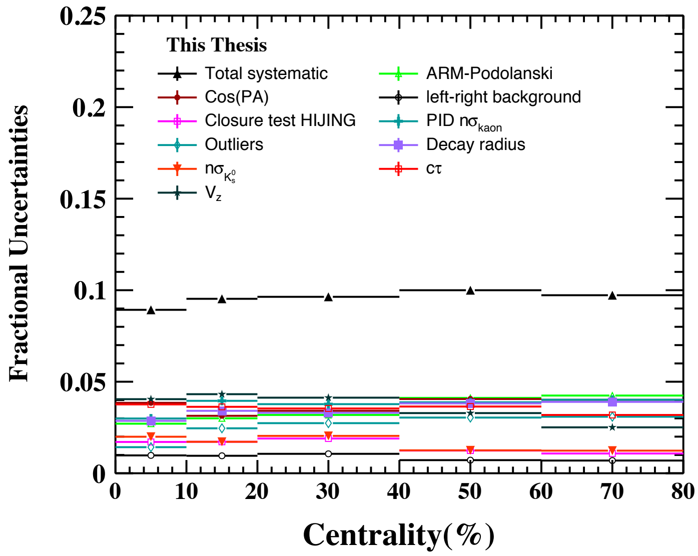

Figure 4.29: The fractional systematic uncertainty of $\nu_{dyn}[K_s^0, K^{\pm}]$ due to various cuts for various centralities in Pb-Pb collisions at $\sqrt{s_{\rm NN}}$ = 2.76 TeV.

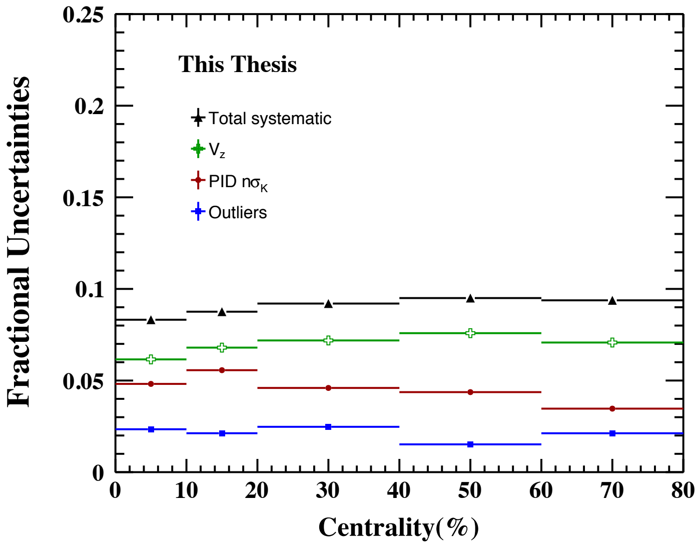

Figure 4.30: The fractional systematic uncertainty of $\nu_{dyn}[K^+, K^-]$ due to various cuts in Pb-Pb collisions at $\sqrt{s_{\rm NN}}$ = 2.76 TeV for various centralities.

Centrality(%)	0-10	10-20	20-40	40-60	60-80
Statistical	0.0003	0.0004	0.0007	0.0017	0.003
$\lvert V_z \rvert$	0.000224	0.00032	0.00071	0.00165	0.0032
PID $\lvert n\sigma \rvert_k$	0.000144	0.000262	0.00039	0.00095	0.00164
Event Outliers	0.0001	0.0001	0.00031	0.00039	0.0015
Total	0.0004	0.0006	0.0012	0.0029	0.005

Table 4.13: The values of the systematic uncertainty for $\nu_{dyn}[K^+, K^-]$ in Pb-Pb collisions at $\sqrt{s_{\mathrm{NN}}}$ = 2.76 TeV obtained for various centralities.

The change of the yield of K_s^0s is observed by varying the decay length between $2c\tau$ and $4c\tau$. The uncertainty obtained from the variation of decay length is less than 4%. The change in the purity of $K^{\pm}$s is observed by changing nσ cuts from -0.5< $\lvert n\sigma \rvert_k$ <2.0 to -2.0< $\lvert n\sigma \rvert_k$ < 2.0. The uncertainty associated with this variation is less than 4%. The range of the accepted primary vertices has been varied from ±10 cm to ±8 cm. The systematic uncertainty associated with this variation is estimated to be ~4%. The Cosine of the pointing angle of K_s^0s is varied between 0.998 to 0.992. The uncertainty of this variation is less than 4%. A variation of Armenteros-Podolanski cut between 0.17 to 0.23 gives an uncertainty of less than 4%. The systematic uncertainty due to side band background correction is estimated to be less than 2%. The total systematic uncertainty is estimated to be smaller than 10%, for all collision centralities. The Barlow checks are performed to accept (or reject) the sources of systematic uncertainty. Table. 4.11 shows the different types of sources, variation in their values and associated systematic uncertainty of $\nu_{dyn}[K_s^0, K^{\pm}]$. The checks on outliers are also performed. The systematic uncertainty due to outliers is estimated to be less than 2%. Fig . 4.29 shows the fractional systematic uncertainty of $\nu_{dyn}[K_s^0, K^{\pm}]$ for various centralities. Table. 4.13 shows the different types of sources, variation in their values and associated systematic uncertainty of $\nu_{dyn}[K^+, K^-]$. Fig . 4.30 shows the fractional systematic uncertainty of $\nu_{dyn}[K^+, K^-]$ for various centralities. The total systematic uncertainty is estimated to be smaller than 10%, for all collision centralities.

4.11.3 Error Propagation Technique

Three different methods have been used in this analysis while calculating the error in the ratio of measured quantity. Let dx be the uncertainty associated with the measured quantity x and dy be the uncertainty associated with another measured quantity y. The statistical error propagation is given by following expressions.

(1) Traditional error propagation:

$$\sigma = \frac{x}{y}\sqrt{\left(\frac{dx}{x}\right)^2 + \left(\frac{dy}{y}\right)^2}, \tag{4.34}$$

(2) Binomial error propagation:

$$\sigma = \frac{x}{y}\left(\frac{dx}{x} - \frac{dy}{y}\right), \tag{4.35}$$

and (3) Extreme error propagation:

$$\sigma = \frac{x}{y} - \left(\frac{x \pm dx}{y \pm dy}\right), \tag{4.36}$$

where σ is the final error after propagation. The binomial error propagation has been used in this analysis and the sources of errors are assumed to be uncorrelated.

4.12 Experimental Results

This section describes the experimental results of $\nu_{dyn}[K_s^0, K^{\pm}]$ measurements performed in Pb-Pb collisions at $\sqrt{s_{NN}} = 2.76$ TeV in ALICE as shown in Fig. 4.31. The ν_{dyn} values for charged and neutral pairs calculated by considering the expression of ν_{dyn} described in section 3.2. The measured values are compared with MC simulations obtained from HIJING and AMPT model. Three different tunes of the AMPT event generator were used to study the fluctuations in the strangeness sector.

- String Melting ON (SON) hadronic rescattering OFF (ROFF).
- String Melting OFF (SOFF) hadronic rescattering ON (RON).
- STRING Melting ON (SON) hadronic rescattering ON (RON).

The values of $\nu_{dyn}[K_s^0, K^{\pm}]$ estimated from HIJING show a slightly increasing trend from central to peripheral collisions. The values obtained from AMPT (SOFF, RON and SON,RON) are in agreement with HIJING in each centrality bin. The values are little bit higher for SON and ROFF, compared to other tunes. The ROFF mode switches off the decay of resonance particles, which might influence the decrease of produced kaons. This results in the change of moments of kaon multiplicity distribution and hence $\nu_{dyn}[K_s^0, K^{\pm}]$, which indicates that ν_{dyn} is sensitive to the production dynamics. The measured values of $\nu_{dyn}[K_s^0, K^{\pm}]$ show a monotonic decrease from peripheral to central collisions. The measured $\nu_{dyn}[K_s^0, K^{\pm}]$ values (red solid circles) are significantly higher (approximate factor of two in peripheral collisions and by an order of magnitude in most central collisions) than the values obtained in MC simulations.

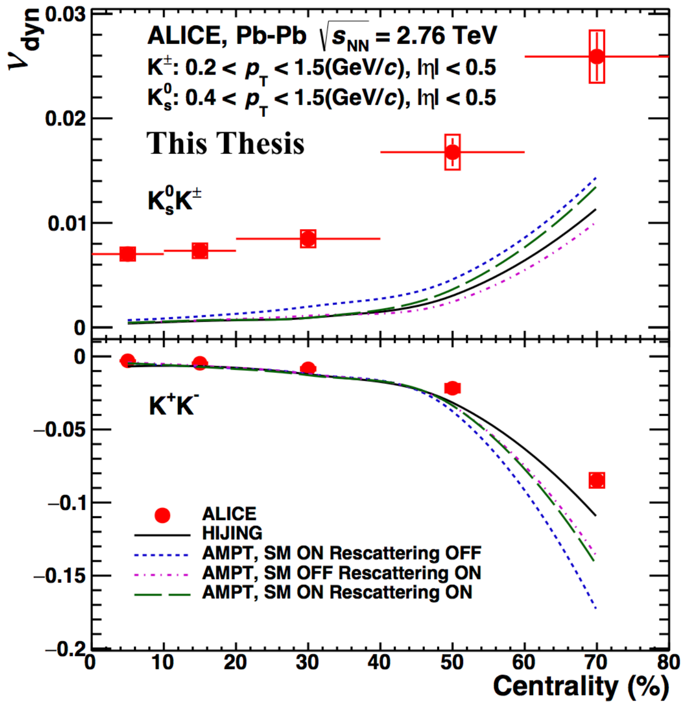

Figure 4.31: **Upper panel**: The values of $\nu_{dyn}[K^0_s, K^{\pm}]$ as a function of collision centrality classes; **Bottom panel**: The values of $\nu_{dyn}[K^+, K^-]$ as a function of collision centrality in Pb-Pb collisions at $\sqrt{s_{\rm NN}}$ = 2.76 TeV. The solid and dashed lines show the values obtained from MC simulations.

The magnitude of $\nu_{dyn}[K_s^0, K^{\pm}]$ is expected to scale inversely with the number of sources, N_s, for collision systems involving independent nucleon-nucleon collisions and no scattering of produced particles [51]. Generally, the number of sources is expected to be proportional to the produced charged-particle multiplicity. Therefore it is appropriate to scale the $\nu_{dyn}[K_s^0, K^{\pm}]$ with multiplicity of the collisions. Fig. 4.32 (Upper panel), shows the values of $\nu_{dyn}[K_s^0, K^{\pm}]$ scaled by the measured mean charged particle density, $\langle dN_{ch}/d\eta \rangle$ [59]. It can be observed from the figure that the values estimated from HIJING and AMPT models are essentially independent of collision centrality. In particular, the values obtained from HIJING exhibit a nearly perfect scaling with the multiplicity, while the values estimated with AMPT (with SON and ROFF) exhibit a modest collision centrality dependence. However, the measured data, exhibit a monotonic increase from central to peripheral collisions. The scaled $\nu_{dyn}[K_s^0, K^{\pm}]$ value is $\approx 1.37 \pm 0.12$ in the 60-80% collision centrality while it is 10.68 ± 1.07 in most central collisions. So, the observed trend in measured values strongly violates the expected $1/N_s$ scaling of $\nu_{dyn}[K_s^0, K^{\pm}]$ observable.

The strength of charged kaon correlations is examined by obtaining the values of $\nu_{dyn}[K^+, K^-]$ as a function of centrality and comparing it to the predictions of AMPT and HIJING models. This is shown in the bottom panel of Fig. 4.31, and the values scaled by the charged particle density are shown in the bottom panel of Fig. 4.32. It was observed that the deviations of measured $\nu_{dyn}[K^+, K^-]$ from HIJING and AMPT model predictions are smaller than those for $\nu_{dyn}[K_s^0, K^{\pm}]$. The scaled values of $\nu_{dyn}[K^+, K^-]\langle dN_{ch}/d\eta \rangle$ exhibit some collision centrality dependence, and the implied scaling violation is considerably smaller than that observed for $\nu_{dyn}[K_s^0, K^{\pm}]$. It was concluded that although HIJING and AMPT do not perfectly capture the magnitude and collision dependence of $\nu_{dyn}[K^+, K^-]$, they nonetheless provide a relatively accurate description of the role of charge conservation, for $K^{\pm}$s, in Pb-Pb collisions. This indicates that the large centrality dependence of $\nu_{dyn}[K_s^0, K^{\pm}]$ does not originate from anomalous charge correlations.

Furthermore, the three terms of $\nu_{dyn}[K_s^0, K^{\pm}]$ expression are investigated individually in both data and HIJING model. Fig. 4.33 shows the ratio of the measured value to the one obtained from HIJING for each individual term as a function of collision centrality. The ratio $R_{00}/R_{00}^{\mathrm{HIJING}}$ exhibits the largest deviation from unity but is otherwise independent, of collision centrality within uncertainties. The R_{00} term thus exhibits the $1/N_s$ scaling expected from a system consisting of independent sources. The $R_{cc}/R_{cc}^{\mathrm{HIJING}}$ ratio is closest to unity but features a modest collision centrality dependence. The ratio $R_{c0}/R_{c0}^{\mathrm{HIJING}}$ is of the order of unity in 60-80% collision centrality and is consistent with $R_{cc}/R_{cc}^{\mathrm{HIJING}}$ in that centrality. However, the deviation from unity increases from peripheral

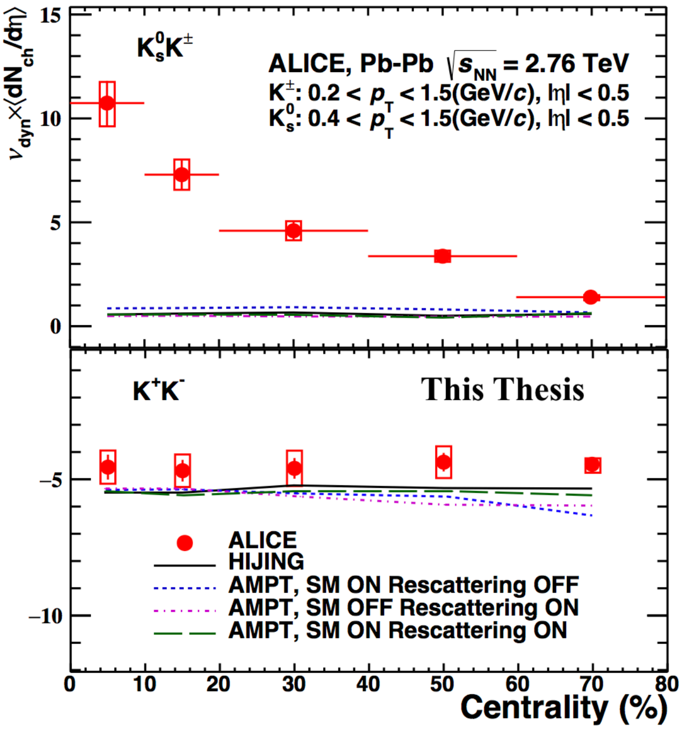

Figure 4.32: **Upper panel**: The values of $\nu_{dyn}[K^0_s, K^\pm]$ scaled by the charged particle density as a function of centrality; **Bottom panel**: $\nu_{dyn}[K^+, K^-]$ scaled by the charged particle density in Pb-Pb collisions at $\sqrt{s_{\rm NN}}$ = 2.76 TeV as a function of centrality.

to central collisions. Indeed, the largest deviation of $R_{c0}/R_{c0}^{\rm HIJING}$ from unity is observed in most 0-10% collisions. This factor is proportional to the covariance of the yield of $K^\pm$s and K^0_ss. It can be attributed to the weakening of correlations between K^0_ss and $K^\pm$s. The observed strong decrease of $R_{c0}/R_{c0}^{\rm HIJING}$ in central collisions signals that the level of correlations between K^0_ss and $K^\pm$s is weakening in this range relative to that predicted by HIJING. A weakening of correlation is observed due to production of DCC domains as described in phenomenological model [53]. The observed collision centrality dependence of $\nu_{dyn}[K^0_s, K^\pm]$ in data was consistent with expectations based on a simple DCC model, as described in section 3.2. However, significant contributions from other final stage effects in central collisions can also dilute the correlation developed in the initial stages.

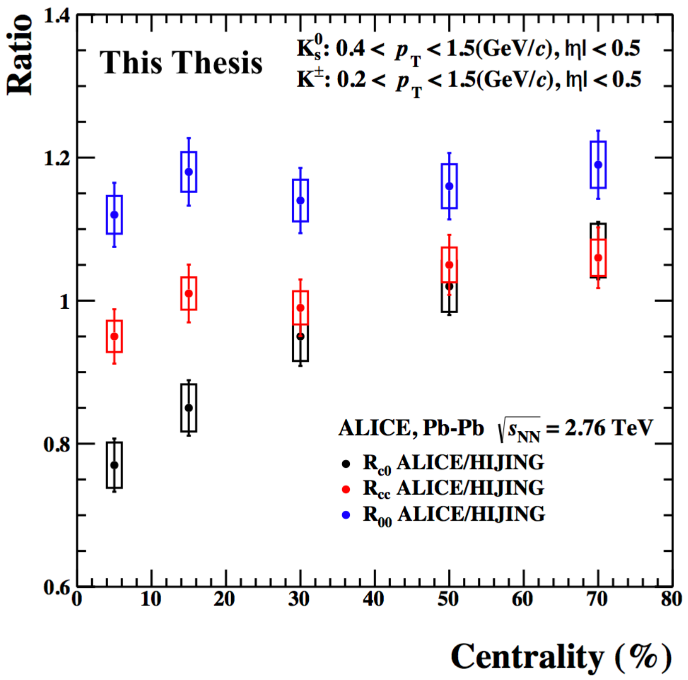

Figure 4.33: The ratio (Data/HIJING) of individual terms of $\nu_{dyn}[K_s^0, K^{\pm}]$ as a function of centrality in Pb-Pb collisions at $\sqrt{s_{NN}}$ = 2.76 TeV.

Chapter 5

Understanding Particle Production in High Energy Collisions Using Different Approaches

5.1 Global Measurements to Understand Particle Production at RHIC and LHC

A strongly-interacting deconfined state of matter known as quark-gluon-plasma is predicted to be produced in high energy heavy-ion collisions. The mechanism of particle production can be inferred by measuring the charged particle multiplicity and transverse energy distributions in such systems at very high energy densities and high temperatures. The production of high transverse momentum (p_{T}) particles (predominately due to hard processes), is expected to scale with the number of collisions, N_{coll}. Whereas the production of low p_{T} particles (from soft processes) is observed to scale with the number of participants, N_{part} [60]. The detailed study of the charged particle multiplicity density ($dN_{ch}/d\eta$) and the transverse energy density ($dE_T/d\eta$) with collision energy and centrality reveals about the contribution of hard and soft processes to the mechanism of the production of particles. The study of the variation of $dN_{ch}/d\eta$ ($dE_T/d\eta$) as a function of collision centrality and collision energy has been performed by considering three different approaches. The first approach considers the two-component model, where nucleus-nucleus collisions are divided into soft and hard interactions. The two component approach [60] parametrizes $dN_{ch}/d\eta$ as the following,

$$\frac{dN_{ch}}{d\eta} = n_{pp}\left((1-x)\frac{\langle N_{part}\rangle}{2} + x\langle N_{coll}\rangle\right), \tag{5.1}$$

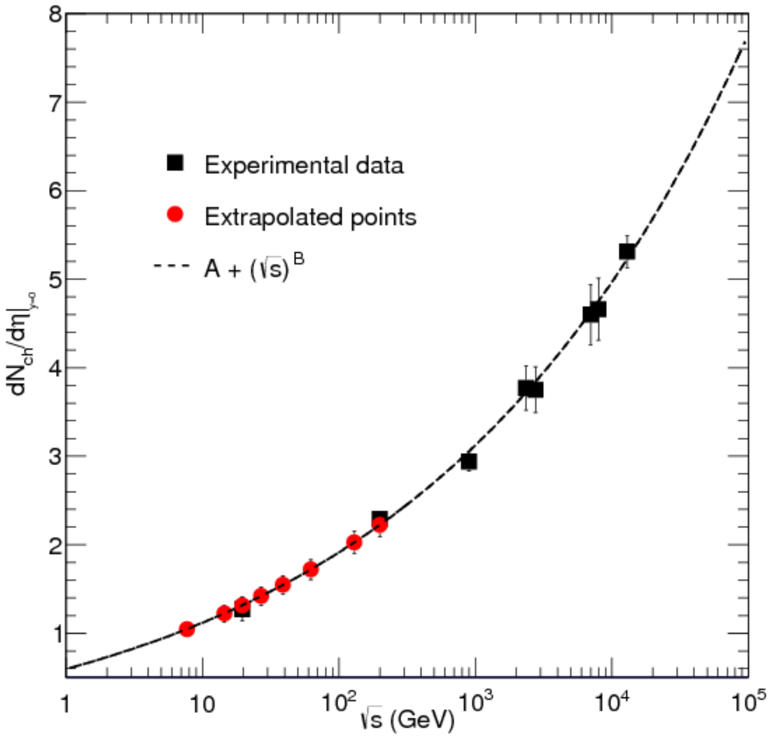

Figure 5.1: $\langle dN_{ch}/d\eta \rangle$ as a function of collision energy measured in pp collisions at RHIC [69] and LHC [70, 71]. The solid squares represent the experimentally measured n_{pp} data. The data is described by a power law fit ($A + \sqrt{s}^B$). The solid circles are the extrapolated data for the RHIC beam scan energies [72].

where n_{pp} refers to the mean charged-particle multiplicity in a single nucleon-nucleon collision and x refers to the fraction of the "hard" processes. In this approach, the parameter n_{pp} is constrained for a particular energy by using the experimentally measured values. This leads to the robust extraction of x parameter concerning collision centrality and beam energy. The charged particle multiplicity density ($dN_{ch}/d\eta$) is also studied by a single component model [65, 66, 67, 68] in the other two approaches. The variation of $dE_T/d\eta$ as a function of collision centrality and energy can be studied using a similar approach. In the case of $dE_T/d\eta$, mean $E_{T_{pp}}$ is considered as a free parameter due to lack of broad experimental measurement of $E_{T_{pp}}$ (for nucleon-nucleon collisions). In this study, the x parameter values used are obtained from the $dN_{ch}/d\eta$ distribution. The variation of $E_{T_{pp}}$ as a function of beam energy can be estimated by this method.

5.1.1 Analysis Procedure

The PHENIX experiment at the RHIC has measured $dE_T/d\eta$ and $dN_{ch}/d\eta$ distribution for different sets of energies [73] in Au-Au collisions. The ALICE experiment at the

$\sqrt{s_{NN}}$	a	b
7.7 GeV	0.315 ± 0.099	1.34 ± 0.057
19.6 GeV	0.312 ± 0.096	1.35 ± 0.055
27 GeV	0.306 ± 0.1	1.36 ± 0.058
39 GeV	0.301 ± 0.096	1.36 ± 0.056
62.4 GeV	0.395 ± 0.097	1.32 ± 0.054
130 GeV	0.367 ± 0.144	1.35 ± 0.073
200 GeV	0.356 ± 0.117	1.36 ± 0.065
2760 GeV	0.365 ± 0.052	1.41 ± 0.025
5020 GeV	0.352 ± 0.523	1.42 ± 0.027

Table 5.1: The parameters a and b obtained from the parametrization of N_{part} and N_{coll} for different collision energies [72].

LHC has measured $dN_{ch}/d\eta$ distribution in Pb-Pb collisions at 2.76 TeV and 5.02 TeV [68, 74] and the $dE_T/d\eta$ distribution in Pb-Pb collisions at 2.76 TeV [75]. The values for n_{pp}, were obtained by extrapolating the $\sqrt{s}$ dependence of measured n_{pp} in pp collisions at different energies, due to unavailability of the charged-particle multiplicity data in pp collisions at RHIC. This is shown in Fig. 5.1. The solid squares represent the measured data from RHIC [69] and LHC [70, 71]. The dashed line refers to the power law fitting of the measured data. The closed circles are the extrapolated n_{pp} values for the beam energies scan measurements at RHIC. The values of $\langle N_{part}\rangle$ and $\langle N_{coll}\rangle$ are required for the comparison of the two-component model with the experimental data. The Glauber MC model [58] has been considered to obtain the values of $\langle N_{part}\rangle$, whose power law parametrization provides the values of $\langle N_{coll}\rangle$ by the relation, $N_{coll} = a \times N_{part}^{b}$. Table 5.1 shows the values of the parameters for different energies. The data is fitted with Eq. 5.1 to obtain the value of the parameter x. A single component parametrization of the forms [65, 66, 67, 68],

$$\frac{dN_{ch}}{d\eta} \propto \langle N_{part}\rangle^{\alpha}, \tag{5.2}$$

$$\frac{dN_{ch}}{d\eta} \propto \langle N_{coll}\rangle^{\beta}, \tag{5.3}$$

have also been used to describe the $dN_{ch}/d\eta$ distribution, where α and β are the free parameters. The analysis of $dE_T/d\eta$ was also carried using similar steps with a little modification. The mean transverse energy ($E_{T_{pp}}$) obtained in pp collisions was treated as a free parameter and the values of the parameter x are obtained from the fits to the measured $dN_{ch}/d\eta$ data with Eq. 5.1.

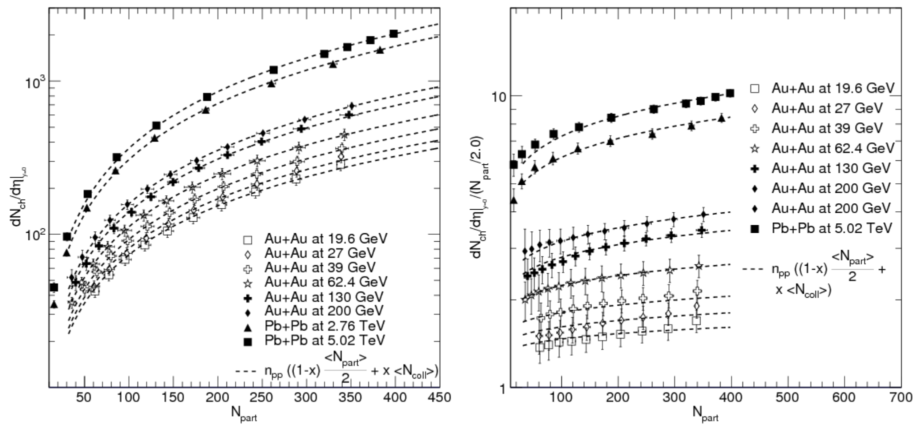

Figure 5.2: **Left panel**: The charged particle multiplicity densities as a function of number of participants measured in Au-Au and Pb-Pb collisions at RHIC and LHC energies, respectively. The dashed line represents the fits to the measured data with Eq. 5.1. **Right panel**: The charged particle multiplicity densities scaled with number of participants measured in heavy-ion collisions at RHIC and LHC energies. The dashed line represents the fits to the measured data with Eq. 5.1 [72].

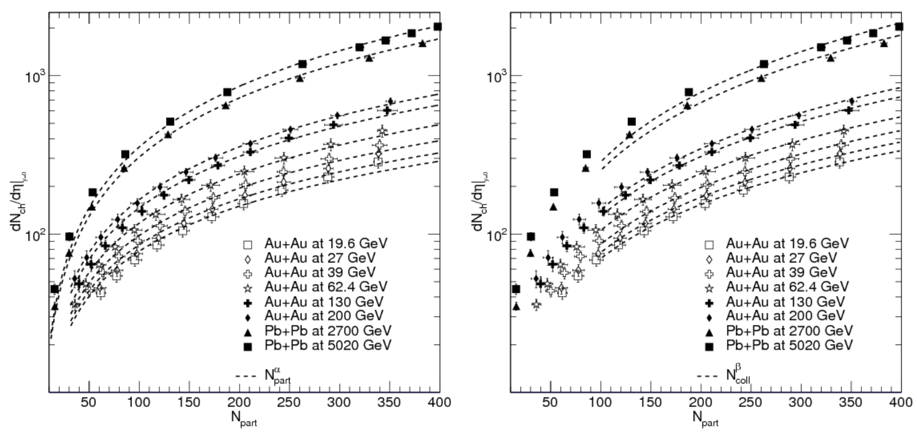

Figure 5.3: **Left panel**: The charged particle multiplicity densities as a function of number of participants measured in heavy-ion collisions at RHIC and LHC energies. The dashed line represents the fits to the measured data with Eq. 5.2. **Right panel**: The charged particle multiplicity densities as a function of number of participants measured in heavy-ion collisions at RHIC and LHC energies. The dashed line represents the fits to Eq. 5.3 [72].

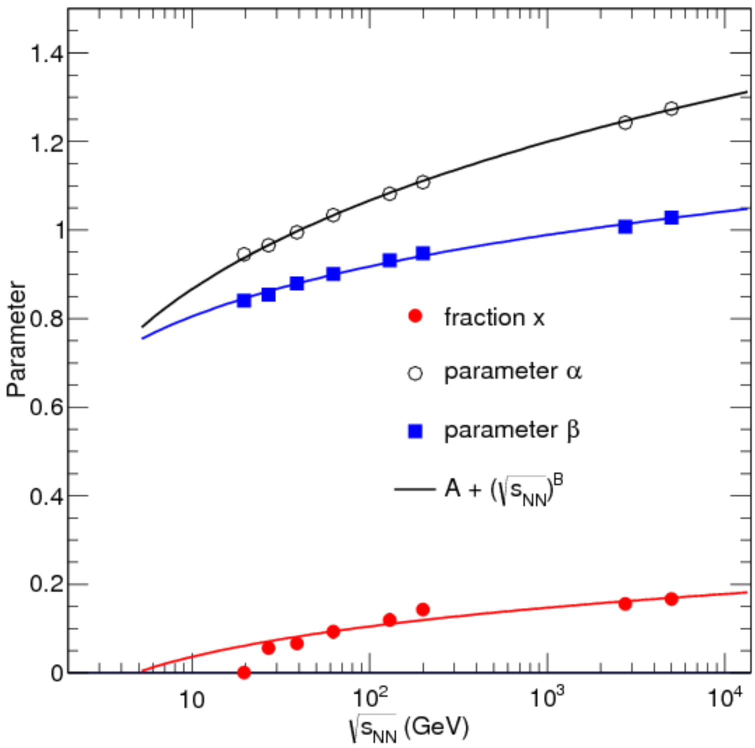

Figure 5.4: The variation of the parameters x (solid circles), α (open circles) and β (solid squares) as a function of $\sqrt{s_{\rm NN}}$. The solid lines are the power law parametrization [72].

5.1.2 Results: Charged Particle Multiplicity Densities

The left panel of the Fig 5.2 shows the fit of the $dN_{ch}/d\eta$ data measured at RHIC [73] and LHC [68, 74] energies, with the two component model. The right panel of the Fig 5.2 depicts the scaled values of the multiplicity densities with the number of participants. The dashed lines show the fit as per two component approach. The scaled values of the multiplicity densities are less dependent on the $\langle N_{part}\rangle$ at RHIC energies. However, the scaled values of the multiplicity density show a dependence on system size at the LHC energies. The scaled values of the multiplicity densities exhibit an increasing trend with system size due to large difference in energies. The single component fits (Eq. 5.2 and Eq. 5.3) are displayed in the left and right panels of Fig 5.3, respectively. It can be observed that the single component parametrization describes the measured data for all energies. Fig 5.4 depicts the variation of all three parameters, x, α and β as a function of $\sqrt{s_{\rm NN}}$. The parameters exhibit an increasing trend with increase in collision energies. The trend can be attributed to an increase in the number of hard processes with an increase in beam energy. A power law fit of the form $A + \sqrt{s_{\rm NN}}^B$ is considered to describe the trend. Fig 5.5 shows the pairwise ratios of $dN_{ch}/d\eta$ for two different energy sets per participant pairs. The ratio of the charged particle multiplicity densities at two

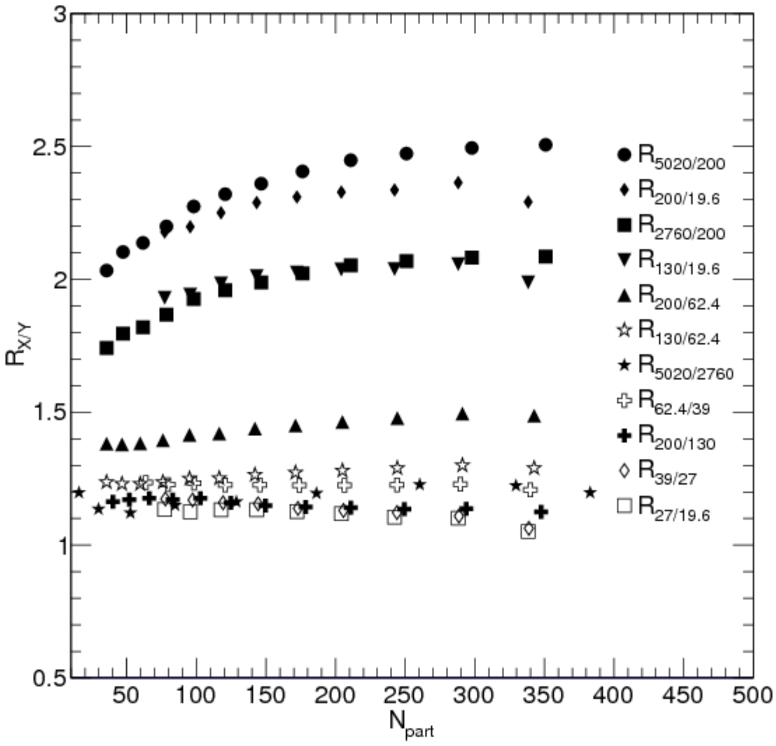

Figure 5.5: The pairwise ratios of the charged particle multiplicity density as a function of the number of participant pairs [72].

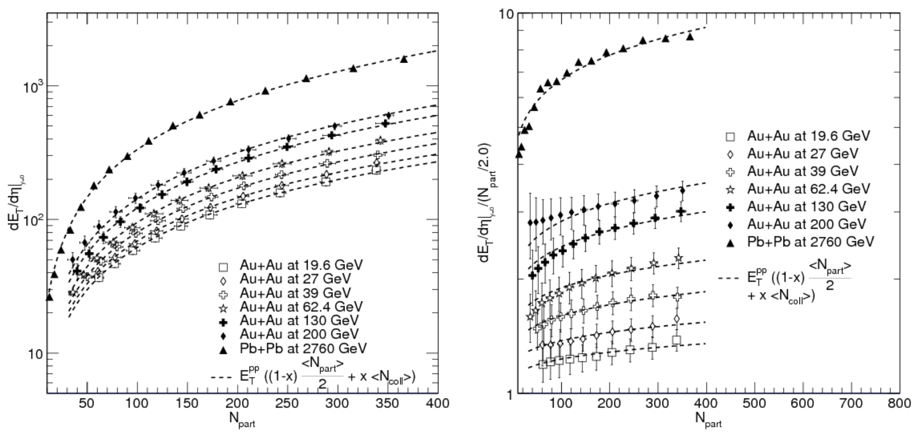

Figure 5.6: **Left panel**: The charged particle transverse energy densities as a function of number of participants measured in heavy-ion collisions at RHIC and LHC energies. The dashed line represents the fits to measured data with Eq. 5.1. **Right panel**: The charged particle transverse energy densities scaled by the number of participants measured in heavy-ion collisions at RHIC and LHC energies. The dashed line represents the fits to the measured data with Eq. 5.1 [72].

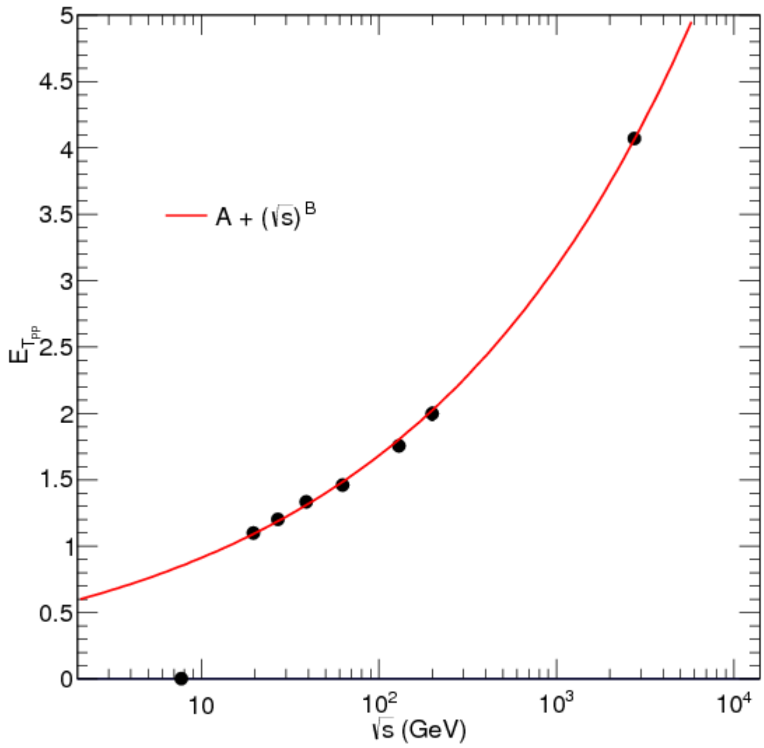

Figure 5.7: The variation of mean transverse energy measured in pp collisions as a function of center of mass energy. This is parametrized by a power law shown by the solid line [72].

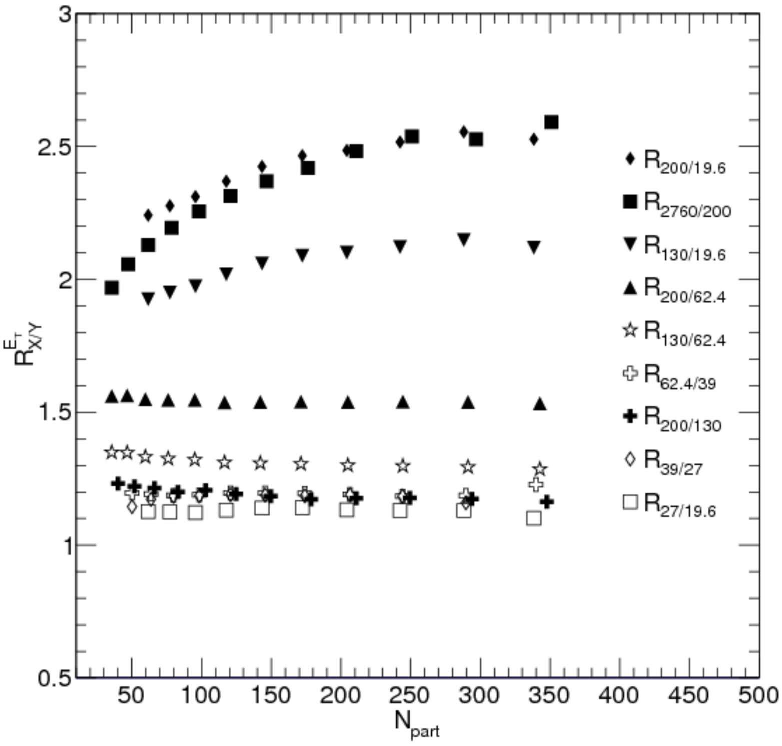

Figure 5.8: The variation of the pairwise ratios of the transverse energy density as a function of $\langle N_{part}\rangle$ [72].

different energies X and Y (where Y < X) can be obtained by quantifying the variable given by,

$$R_{X/Y} = \frac{dN_{ch}/d\eta}{\langle N_{part}\rangle/2}|X/\frac{dN_{ch}/d\eta}{\langle N_{part}\rangle/2}|Y. \tag{5.4}$$

The ratio is obtained for similar $\langle N_{part}\rangle$ values. If the range of the collision energy differs by a factor of 3 or less, the ratio is observed to be independent upon system size (for example $R_{27/19.6}$, $R_{39/27}$, $R_{62.4/39.0}$ and $R_{200/130}$). The magnitude of the ratio shows an increasing trend as a function of $\langle N_{part}\rangle$ for two different collisional energies which differ by a factor of 4 or more. The pairwise ratios increase by ~20 % from peripheral to central collisions. The observed trend is not due to energy difference only, ($R_{200/19.6}$ for a particular $\langle N_{part}\rangle$, are consistently higher than $R_{2760/200}$). This indicates that the observed trend is determined by both the collision energy difference and the contribution of the hard scattering component.

5.1.3 Results: Transverse Energy Densities

The two component model approach [60] can be used to describe the distribution of transverse energy density, $dE_T/d\eta$ as a function of $\langle N_{part}\rangle$. The values of the parameter x were obtained from $dN_{ch}/d\eta$ distribution fit, while the mean transverse energy obtained in pp collisions, $E_{T_{pp}}$, was treated as a free parameter. The left panel of the Fig 5.6 displays the results of the fit to the measured data. The data is well described by the model from RHIC to LHC energies. Fig 5.7 depicts the variation of the extracted values of $E_{T_{pp}}$ as a function of beam energy. The values are parametrized with the function ($A + \sqrt{s_{\rm NN}}^B$). The right panel of the Fig 5.6 depicts the variation of the scaled transverse energy densities as a function of centrality for various beam energies. There is no centrality dependence observed for the scaled energy densities. The pairwise ratios of $dE_T/d\eta$ at two different sets of energies as a function of number of participants are shown in Fig 5.8. A variable $R^{E_T}_{X/Y}$, is used to denote the magnitude of the ratio of transverse energy densities at energy X and energy Y given by,

$$R^{E_T}_{X/Y} = \frac{dE_T/d\eta}{\langle N_{part}\rangle/2}|X/\frac{dE_T/d\eta}{\langle N_{part}\rangle/2}|Y. \tag{5.5}$$

There is no system size dependence observed for the obtained ratios. The values of $R_{2760/200}$ are comparable to that of $R_{200/19.6}$ due to the same order of collision energy difference. The same was not observed for multiplicity densities. Despite the higher x values of $R_{130/19.6}$, the ratio is consistently lower compared to $R_{2760/200}$. This was not observed for the pairwise ratios of multiplicity densities. This observation indicates that x does not play a significant role to describe the observed trend.

5.2 Weibull Model to Study the Normalised Moments of Multiplicity Distribution in pp Collisions

The charged particle multiplicity distribution is measured by the ALICE experiment in larger pseudorapidity (η) gaps for various event classes, such as INEL (inelastic), INEL > 0 (INEL events having at least one charged particle for $|\eta| <1.0$) and NSD (non-singly diffractive events) [76]. This measurement in wider η ranges enables to reach higher multiplicity and explore large phase space. The forward η region is interesting being sensitive to the low Bjorken-x dynamics and the multiple particle interactions [77].

The global conservation laws like energy, momentum and charge affect the distribution of the charged particle multiplicity in pp collisions in full phase space. But the charged particle multiplicity distributions in limited phase space are less affected by the global constraints. The distributions are sensitive to the production dynamics of the particles and their fluctuations [78, 79]. The measurements are compared with several MC event generator predictions such as PYTHIA [80], PHOJET [81] etc. Several QCD processes are implemented in these models and the model predictions are found to underestimate the data [70, 76, 82, 83]. Hence, it is appropriate to study the distributions

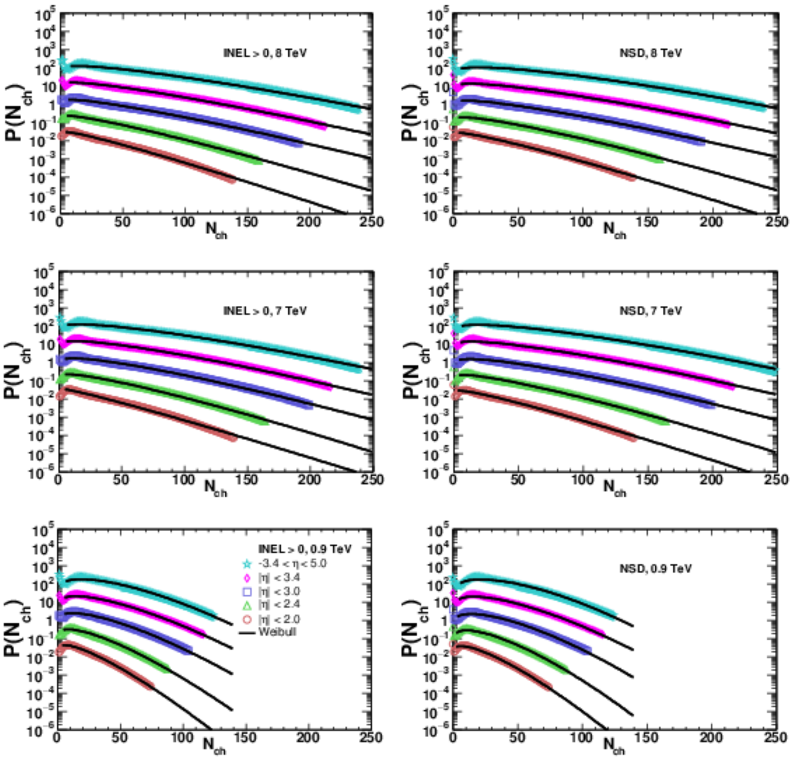

Figure 5.9: The charged particle multiplicity distribution measured by ALICE experiment in different η intervals for pp collisions at $\sqrt{s}$ = 0.9 TeV, 7 TeV, and 8 TeV [76]. The solid lines show the Weibull fit to the measured data [89].

for various event classes (large phase space) to constrain the existing MC models. The deviation of the charged particle multiplicity distribution from Poissonian shape indicates the existence of genuine multiple particle correlations [84, 85] at the LHC. The observables to study these multi-particle correlations are the normalized moments and factorial moments of the charged particle multiplicity distributions.

According to the MC models of production dynamics of the particles, the partons are fragmented into hadrons in a cascading process in high energy hadronic collisions. The Weibull distribution explains the complex processes which evolve through cascading and sequential branching [86, 87]. The Weibull distribution can therefore be used to explain the charged particle distributions in final states. In high energy hadronic and leptonic collisions [86, 87, 88], the charged particle multiplicity distributions are correctly described by the Weibull distribution. It has two parameters known as λ and k which are related to the mean multiplicity and the particle production dynamics, respectively.

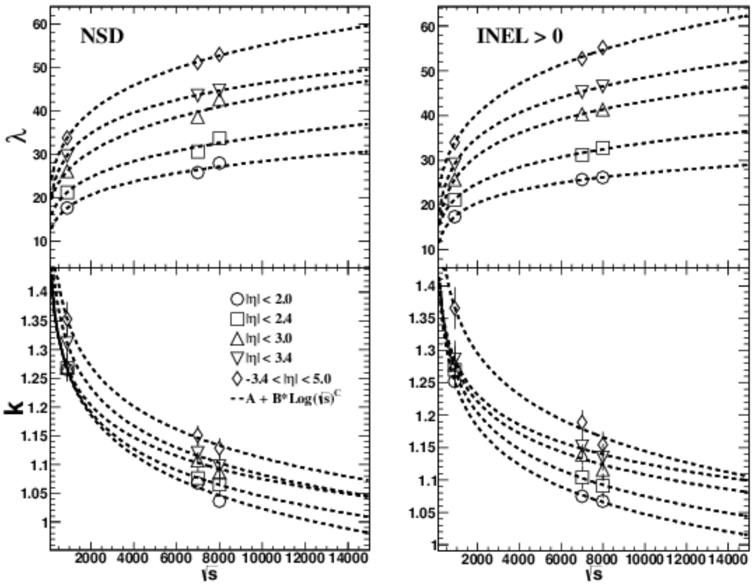

Figure 5.10: The variation of Weibull parameters k and λ with center of mass energy in pp collisions. The variation is parametrized by a power law of the form $A+B\times\log(\sqrt{s})^C$, shown by the dashed curve [89].

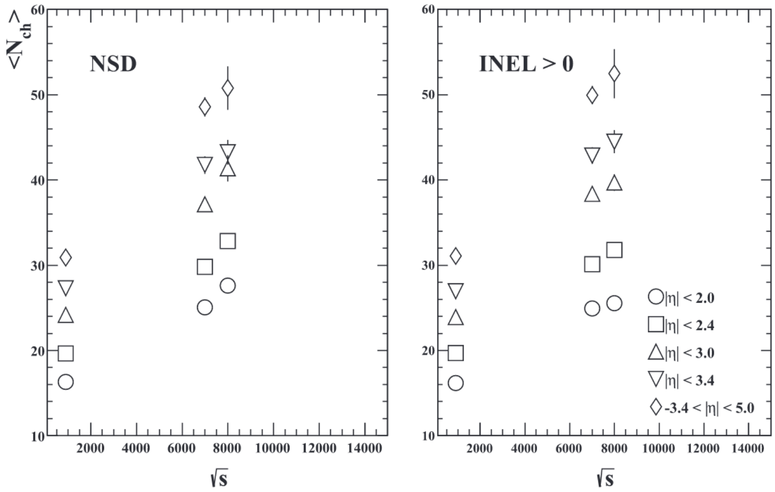

Figure 5.11: The variation of mean (N_{ch}) with centre of mass energy in pp collisions [89].

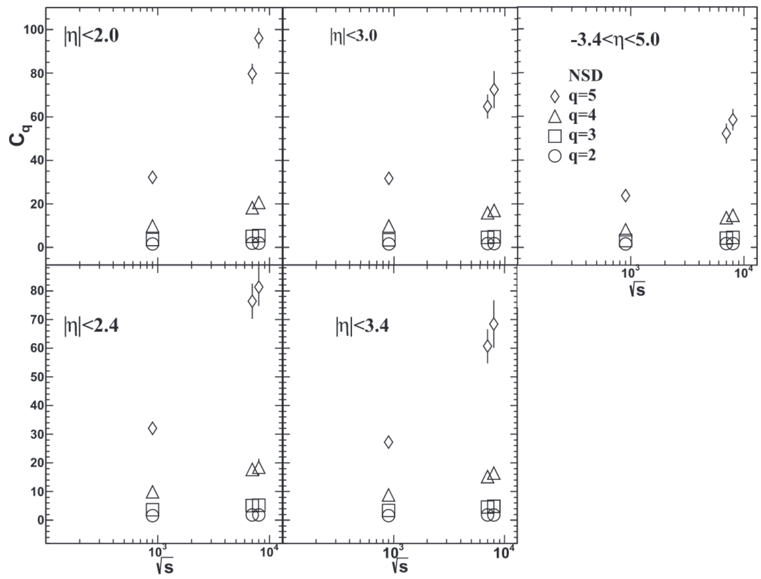

Figure 5.12: The variation of the normalized moments for NSD event class with collision energy as obtained from Weibull calculations for different η intervals [89].

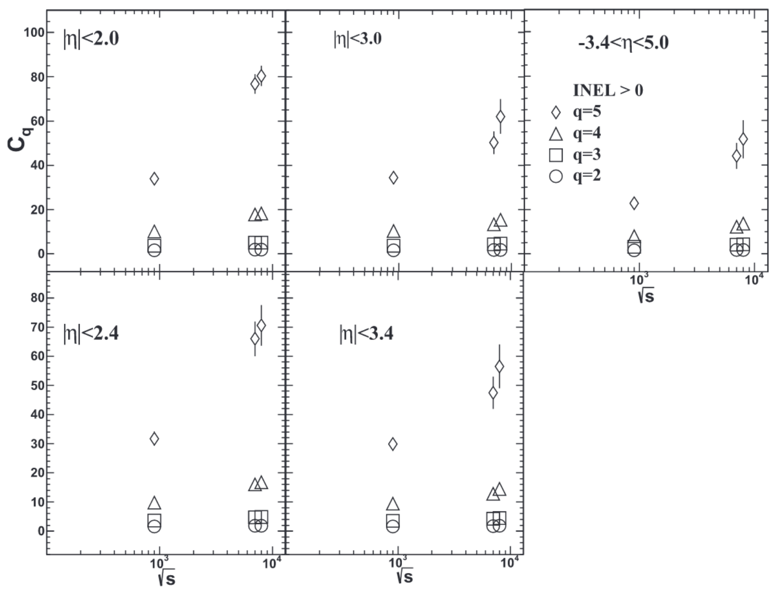

Figure 5.13: The variation of the normalized moments for INEL > 0 event class with collision energy as obtained from Weibull calculations for different η intervals [89].

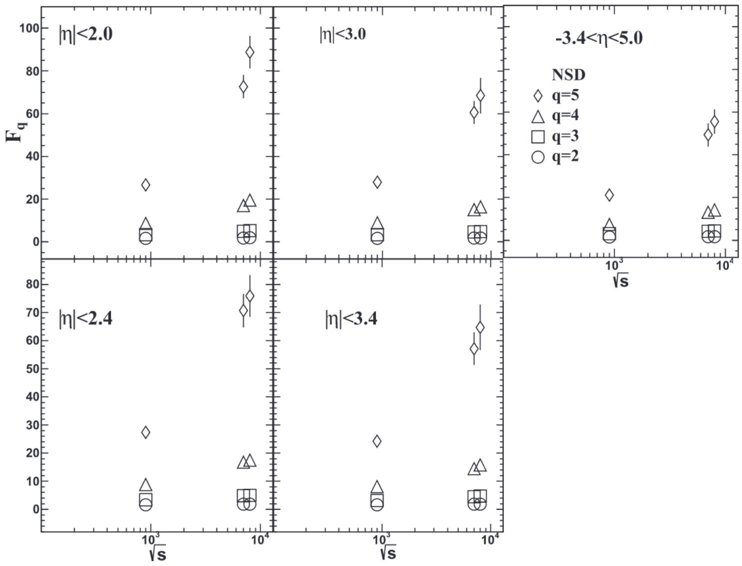

Figure 5.14: The variation of the normalized factorial moments for NSD event class with collision energy as obtained from Weibull calculations for different η intervals [89].

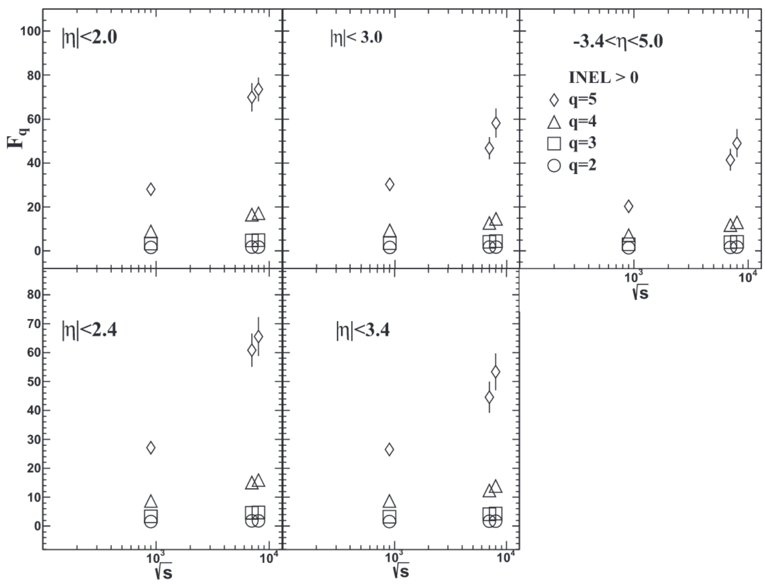

Figure 5.15: The variation of the normalized factorial moments for INEL > 0 event class with collision energy as obtained from Weibull calculations for different η intervals [89].

5.2.1 Weibull Distribution and its moments

The Weibull distribution for a continuous random variable x is given by [86],

$$f(\lambda, k) = \frac{k}{\lambda}\left(\frac{x}{\lambda}\right)^{(k-1)} e^{-\left(\frac{x}{\lambda}\right)^k}, \tag{5.6}$$

where λ represents the scale parameter and k refers to the shape parameter of the distribution. The n^{th} raw moment is given by,

$$m_n = \lambda^n \Gamma\left(1 + \frac{n}{k}\right). \tag{5.7}$$

The mean, $\langle x \rangle$, is given by,

$$\langle x \rangle = \lambda \Gamma\left(1 + \frac{1}{k}\right). \tag{5.8}$$

The n^{th} factorial moment of the variable x is defined as,

$$f_n = \left\langle \frac{x!}{(x-n)!} \right\rangle = \langle x(x-1)(x-2)..(x-n+1) \rangle. \tag{5.9}$$

The n^{th} normalized moment C_n and normalized factorial moment F_n are defined as,

$$C_n = m_n / m_1^n; \qquad F_n = f_n / m_1^n. \tag{5.10}$$

5.2.2 Analysis Method and Results

The Weibull parametrization has been used to describe the charged particle multiplicity distributions in pp collisions at $\sqrt{s} = 0.9$ TeV, 7 TeV and 8 TeV in forward η intervals for various event classes, which are measured by ALICE experiment at the LHC. The Weibull parameters are obtained from the lower order moments which describe the global characteristics of a distribution. These parameters are then used to calculate the higher order cumulants and factorial moments. The higher order moments are calculated to check the KNO scaling violation as reported in previous measurements for central rapidity regions [70, 82, 90]. Two different event classes, NSD and INEL > 0 have been considered in this study. The multiplicity distributions of the charged particles are fitted with Weibull distribution for five different η intervals i.e. $|\eta| < 2.0$, $|\eta| < 2.4$, $|\eta| < 3.0$, $|\eta| < 3.4$ and $-3.4 < \eta < 5.0$ for these two event classes at different energies, which is depicted in Fig. 5.9. The first few bins were not considered during the fits as the number of events due to diffractive processes were larger in those bins. It can be observed that the measured data are well described by the Weibull distribution. The variation of the λ and k (extracted from the fit) with collision energy for various η intervals are displayed in Fig. 5.10. The values of λ increase with increase in beam energy and η interval. The values of k decrease with beam energy and increase with η interval. The variations of these parameters are described by a power law of the form $A + B \times \log(\sqrt{s})^C$. Fig. 5.11 depicts the variation of the mean multiplicity, $\langle N_{ch} \rangle$, (obtained from Eq. 5.8) as a function of beam energy. The figure indicates that with an increase in beam energy, the mean multiplicity value increases. The forward η regions are dominated by soft interactions which include processes like re-scattering, diffractive interactions and low Bjorken-x physics. The increase in the values of parameter k with the increase in η gaps can be associated with the large contribution of the soft process. The trend of the parameters are similar to the previous observations performed in the central rapidity region [87, 88, 90].

The higher order (up to 5^{th}) normalized cumulants and factorial moments are calculated using Eq. 5.10. The variation of the normalized cumulants (C_q) with energy for NSD and INEL > 0 event classes are shown in Fig. 5.12 and Fig. 5.13, respectively. The variation of the normalized factorial moments (F_q) with energy for NSD and INEL > 0 event classes are depicted in Fig. 5.14 and Fig. 5.15, respectively. The figures clearly show that C_2 (and F_2) has almost no beam energy dependence but with an increase in energy, C_3 (and F_3) exhibits an increasing trend for all studied η intervals. The 4^{th} and the 5^{th} order moments, C_4 (and F_4) and C_5 (and F_5) exhibit an increasing trend with increase in energy and for large η windows, they become larger. This observation is obtained for both NSD and INEL > 0 event classes which indicates the KNO scaling violation.

5.3 Effect of Rope Hadronization on the Production of Strange Particles at LHC Energies

In heavy-ion collisions, the increased production of strange and multi-strange hadrons are considered to be the signature of the QGP medium [91]. The enhancement of strange and multi-strange particles in high multiplicity pp collisions as measured by LHC experiments at the ALICE [26] and the observation of long ridge like structures in two particle correlations in pp collisions performed by CMS and ATLAS [92, 93, 94] have aroused a lot of curiosity towards the collision of small systems. These observations are similar to the one observed in heavy-ion collisions and therefore make the study in smaller systems interesting.

The valence strange quarks are produced in hard processes (high p_{T}) like flavor excitation and flavor creation in the initial stage of the collision process. Due to the heavier mass of strange quarks compared to up and down quark mass, the strange particle productions are suppressed in low p_{T} regions. The enhanced production of strange and multi-strange hadrons in central and mid-central collisions in heavy-ion collisions is attributed to the production of strange and anti-strange quarks in the QGP medium [91, 95]. Several statistical models based on the grand canonical approach are considered, which describe successfully the heavy-ion measurements. The productions of strange particles in peripheral heavy-ion collisions are similar to pp collisions and are due to the strangeness canonical suppression. Many MC models based on string hadronization are considered to explain several experimental observations [96], which do not assume the formation of thermalized plasma medium in them. The rope hadronization is a mechanism based on string fragmentation in QCD, which quite successfully describes the strangeness enhancement within color reconnection framework [97, 98, 99]. The DIPSY model which assumes the formation of color ropes describes the enhancement of K_s^0 and Λ quite well but fails to quantify the enhanced production of Ξ and Ω [26].

5.3.1 Rope Hadronization

The production of hadrons in high energy hadronic collisions can be categorised into two simple steps, (i) initial hard scattering process leading to the production of partons and (ii) hadronization of the configuration of initial partons [100, 101]. The perturbative QCD is used to describe the generation of partons while, the string fragmentation of partons into the final state hadrons is described by nonperturbative QCD. The Lund string fragmentation model [96] has been very successful to describe the hadronization process. In this model, the massless string between two partons is stretched leading to linear confinement. The stretching of the string increases the potential energy in it and with an increase in potential energy, the quark-antiquark pair at the two ends of the string move apart which leads to the breaking of the string. The quarks from the broken string are then combined with each other to form hadrons. The multipartonic interactions in high energy collisions lead to the overlapping of strings and describe the underlying processes within the rope hadronization framework [102, 103]. The strings overlap to form color ropes within the rope hadronization framework. A higher energy density region is produced in the overlap region compared to the nearby regions, which leads to the creation of a pressure gradient. As a result, the string is pushed outwards (transverse direction) and can mimic flow like effects as measured in nucleus-nucleus collisions [104]. If the color rope hadronizes with higher string tension, more number of strange quarks and diquarks are expected to be produced, which results in the enhanced production of baryons and strange-hadrons. The rope hadronization mechanism was first implemented in DIPSY event generator [99].

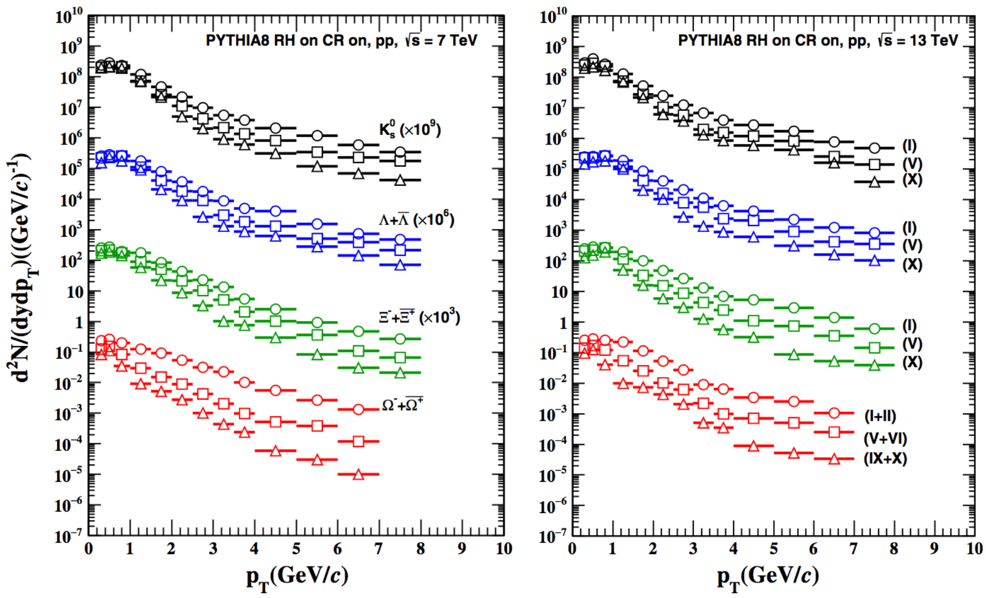

Figure 5.16: p_{T} distribution of strange and multi-strange hadrons in pp collisions at $\sqrt{s}$ = 7 TeV (**Left panel**) and 13 TeV (**Right panel**) for $|y| < 0.5$ generated with PYTHIA8 generator. The distribution are shown with QCD-based color reconnection scheme within the framework of rope hadronization. The open circles, squares and triangles correspond to different multiplicity classes [105].

5.3.2 Analysis Methods and Results

The enhanced production of strange particles is studied by rope hadronization mechanism [97, 106] in pp collisions at $\sqrt{s}$ = 7 and 13 TeV using PYTHIA8. The dependence of strange particle productions on beam energy are also studied by evaluating mean p_{T} ($\langle p_{\mathrm{T}}\rangle$) and mean integrated yield ($\langle dN/dy\rangle$). PYTHIA8 is a standalone generator which successfully describes the physical processes in e^+e^-, pp and $\mu^+\mu^-$ collisions. The detailed description of the physics processes in the model can be found in [107]. The Monash 2013 tune [108] has been considered in this study to generate 50 Million inelastic non-diffractive pp events at $\sqrt{s}$ = 7 TeV and 13 TeV energies. The multi-parton interactions (MPI) enabled with QCD-based color reconnection (CR) [103, 109] and rope hadronization for this study. The ranges of the multiplicity obtained by slicing the total number of events into ten different event multiplicity classes based on the total charged particle multiplicity in the ALICE V0 detector acceptance. The transverse momentum distribution, p_{T}, of various strange particles, K_S^0, Λ, Ξ and Ω for pp collisions at $\sqrt{s}$ = 7 TeV and 13 TeV in PYTHIA8 are shown in the left and right panels of Fig. 5.16, respectively. The spectra are obtained in the framework of both color reconnection and rope hadronization. The figure indicates that, the p_{T} spectra become harder with increase in multiplicity. The

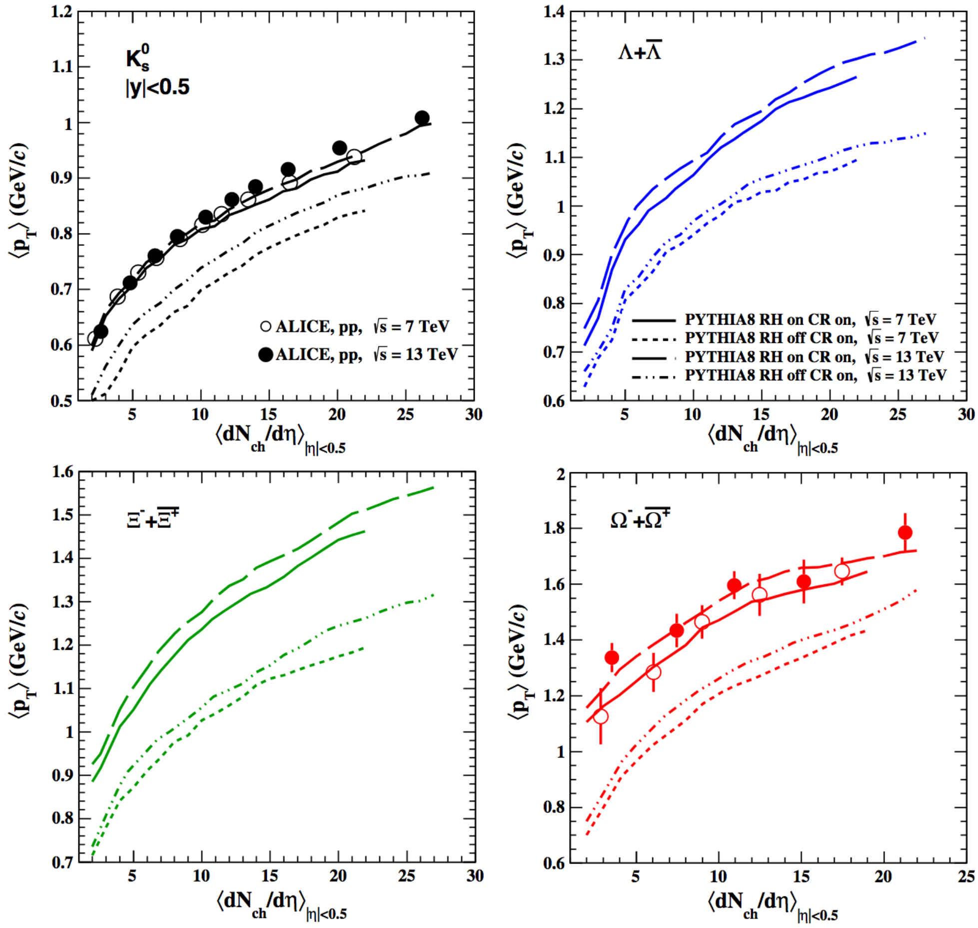

Figure 5.17: $\langle p_{\mathrm{T}} \rangle$ as a function of charged particle density for strange hadrons predicted by PYTHIA8 with and without rope hadronisation in pp collisions at $\sqrt{s}$ = 7 TeV and 13 TeV. The PYTHIA8 estimations at $\sqrt{s}$ = 7 TeV and 13 TeV are also compared to the available data as measured by the ALICE experiment [110] [105].

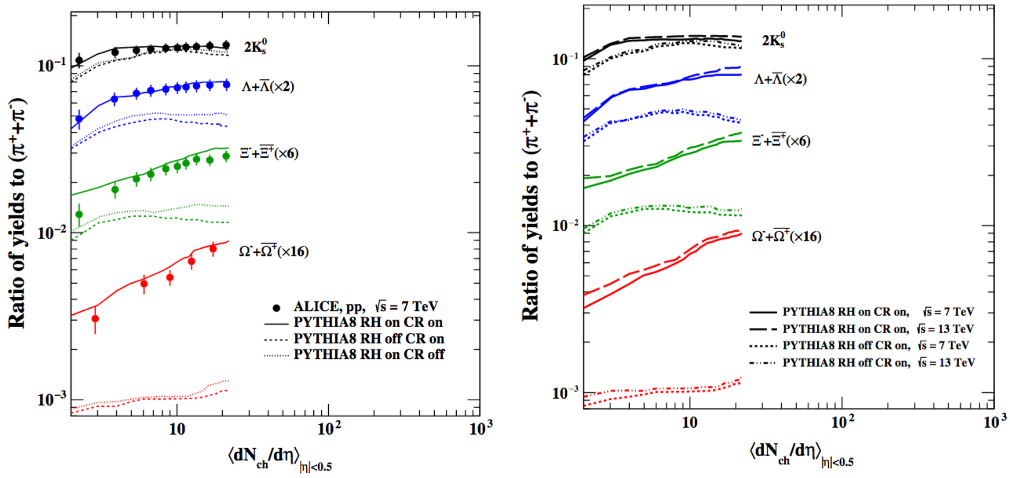

Figure 5.18: **Left panel**: The ratio of yield of strange hadrons to pions as a function of $\langle dN_{ch}/d\eta \rangle$ for $|\eta| < 0.5$ obtained for pp collisions at $\sqrt{s}$ = 7 TeV. The solid markers are data as measured by ALICE experiment at LHC [26]. The solid and dotted lines are estimates of PYTHIA8 (with color reconnection) rope hadronization ON and OFF, respectively. The data points and the PYTHIA8 predictions are suitably scaled for visibility. **Right panel**: The PYTHIA8 estimates of the ratio for pp collisions at $\sqrt{s}$ = 13 TeV compared to 7 TeV [105].

hardening is more for massive particles and is well reproduced by the rope hadronization mechanism. The spectra are obtained for various multiplicity classes for both the energies. To estimate the hardening rate for different multiplicity classes, mean of p_T, $\langle p_{\rm T} \rangle$, is estimated as a function of total charged particle multiplicity. The variation of $\langle p_{\rm T} \rangle$ as a function of multiplicity is shown in Fig. 5.17. The values of $\langle p_{\rm T} \rangle$ obtained with (and without) rope hadronization for K^0_S and Ω are compared with the measured values of ALICE. The values are also estimated for Λ and Ξ as shown in Fig. 5.17. The $\langle p_{\rm T} \rangle$ of strange and multi-strange particles are readily captured with rope hadronization and color reconnection settings for both the collision energies. The strangeness enhancement is quantified by obtaining the ratio of strange and multi-strange hadron yields to the yields of non-strange hadrons i.e, pions. Fig. 5.18 compares the enhancement of strange and multi-strange hadrons with multiplicity measured by ALICE to the values estimated with the PYTHIA8 model with multiplicity. The measured strangeness enhancement in pp collisions at $\sqrt{s}$ = 7 TeV is well described by the rope hadronization mechanism with the framework of color reconnection, while the values obtained without the effect of rope hadronization fail to describe the measured data. The values obtained from the rope hadronization without the color reconnection also fails to describe the data, which indicates that the color reconnection framework is needed with the rope hadronization mechanism to describe the

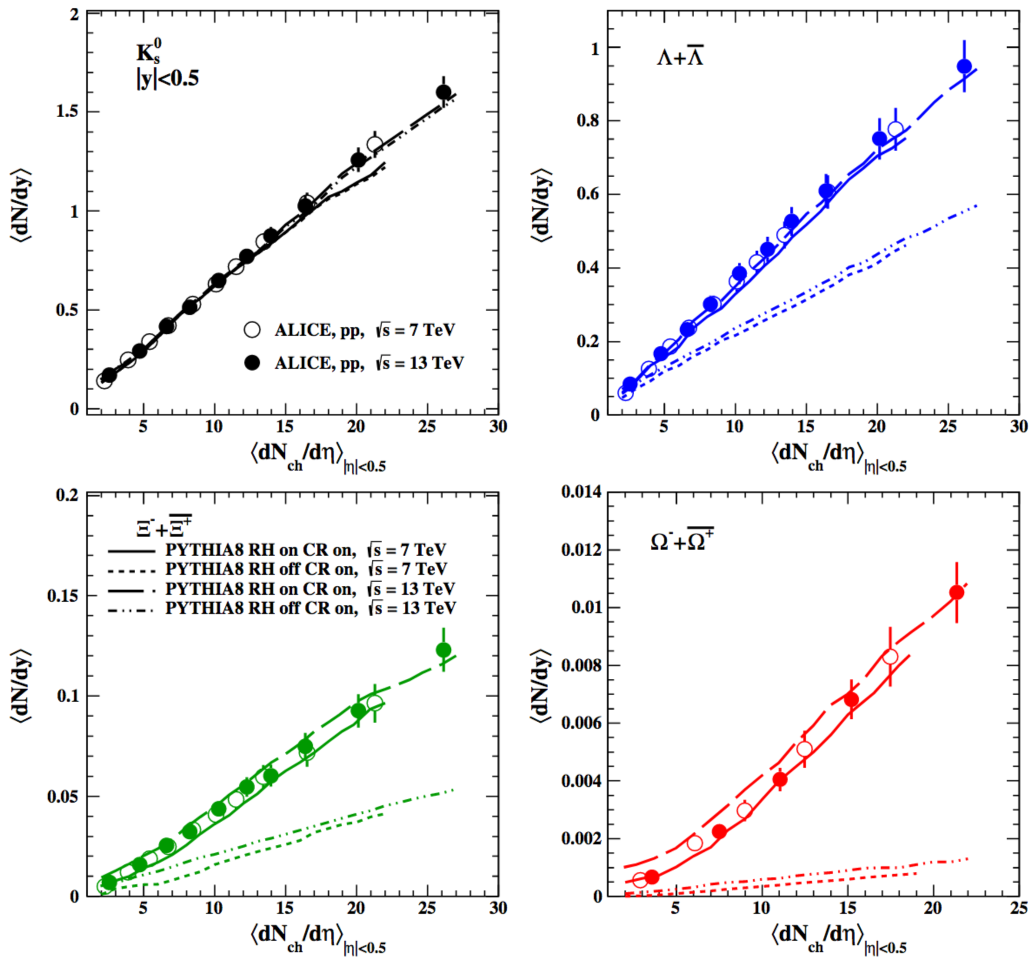

Figure 5.19: The PYTHIA8 predictions of p_T integrated yields for strange and multi-strange hadrons as a function of $\langle dN_{ch}/d\eta\rangle_{|\eta|<0.5}$ using rope hadronization [105].

enhancement in data. The diquark junctions are produced in the QCD based color reconnection that lead to an enhanced production of baryons. The strange baryon enhancements can be explained by this mechanism. The QCD based color reconnection with the rope hadronization mechanism clearly described the measurement of enhanced production of strange particles. Fig. 5.18 displays the enhancements of various strange particles predicted for pp collisions at $\sqrt{s}$ = 13 TeV and are compared with 7 TeV energies. There is no significant energy difference observed for similar multiplicity classes.

The integrated yield of various strange hadrons are obtained as a function of charged particle multiplicity in pp collisions at $\sqrt{s}$ = 7 TeV and 13 TeV to further verify the enhancement in strangeness. Fig. 5.19 displays the comparison of the PYTHIA8 model with the measured data. The model nicely describes the enhancement and the values are in well agreement with the measurement. The study shows that the enhancement is due to the increase in event activity rather than the beam energies. The rope hadronization mechanism within the framework of QCD based color reconnection, which does not assume the formation of thermalised QGP medium is able to describe the strangeness enhancement in pp collisions.

Chapter 6

Summary

The thesis focuses on event-by-event fluctuations of charged and neutral kaons in Pb-Pb collisions at $\sqrt{s_{\rm NN}}$ = 2.76 TeV. This is the first measurement of the event-by-event multiplicity fluctuations in the kaon sector using the ν_{dyn} observable in heavy-ion collisions. The reported work has been carried out using the data collected by the ALICE detector in Pb-Pb collisions at the LHC. The analysis was carried out for different centrality classes (namely 0-10%, 10-20%, 20-40%, 40-60%, and 60-80%). The quality track cuts were obtained by applying various event and track selection cuts. The combined information of TPC and TOF detectors were used to identify charged kaons. The K^0_ss were reconstructed from the invariant mass analysis of their hadronic decay channel $K^0_s \rightarrow \pi^+ + \pi^-$. These were selected after implementing various topological cuts based on decay length, Cosine of pointing angle (Cos(PA)), Armenteros-Podolanski parameter, DCA to primary vertex, etc. The combinatorial background (due to random $\pi^+\pi^-$ pairs not originating from K^0_s decay vertex) present in the selected mass range of $\pi^+\pi^-$ invariant mass distribution was accounted for by performing a detailed background correction. The yield of $K^\pm$s and K^0_ss was corrected for detector efficiency and limited detector acceptance. The statistical uncertainty was estimated using the sub sample method. The systematic uncertainties due to various sources were estimated for each centrality class. The effect of centrality bin width correction has also been studied.

The obtained values of $\nu_{dyn}[K^0_s, K^\pm]$ were studied as a function of centrality. The measured $\nu_{dyn}[K^0_s, K^\pm]$ values monotonically decreased from peripheral to central collisions. The values were also compared to the expectation of HIJING and AMPT (3 modes) MC models. The estimated values from both the models showed a similar trend as a function of collision centrality and underestimated the measured values. The $\nu_{dyn}[K^+, K^-]$ was also estimated and compared to the MC expectations as a function of collision centrality. The obtained values were negative and the magnitude decreased from peripheral to central collisions. The MC estimations also showed a good agreement with the measured values. The observation was attributed to the charge conservation as charged kaons are predominately produced by pair creation. The observable ν_{dyn} obeys an approximate $1/\mathrm{N_s}$ dependence, where $\mathrm{N_s}$ is the number of sources. The scaled values of measured $\nu_{dyn}[K^0_s, K^\pm]$ (scaled with the number of sources approximated as $\langle dN_{ch}/d\eta\rangle$) exhibited a violation of source scaling, however, the violation was not observed in MC models. The scaled $\nu_{dyn}[K^+, K^-]$ exhibited some collision centrality dependence, and the implied scaling violation was considerably smaller than that observed for $\nu_{dyn}[K^0_s, K^\pm]$. The study indicated that the correlated production of neutral and charged kaons is different from the correlated production of oppositely charged kaons. The analysis of the event-by-event multiplicity fluctuations of $K^\pm$s and K^0_ss can be explored in the differential region of η and ϕ for hadronic and nuclear collisions at various energies. The study might signal the production of DCC regions in the experimental data for the differential measurement. The analysis can be performed in high statistics Pb-Pb data at $\sqrt{s_{\mathrm{NN}}}$ = 5.02 TeV in narrow centrality classes.

This thesis presents the simple toy model simulation of the implementation of DCC like events, which was carried out to study the sensitivity of the ν_{dyn} observable to the presence of DCC like events at LHC energy. The $\nu_{dyn}[K^0_s, K^\pm]$ was estimated as a function of centrality for four different scenarios related to the size and number of DCC domains. For a given centrality class, $\nu_{dyn}[K^0_s, K^\pm]$ showed a monotonic increase with the size of the DCC domain and had a large magnitude for the events containing large DCC domains. The values of $\nu_{dyn}[K^0_s, K^\pm]$ scaled by the mean of the number of kaons ($\sqrt{\langle N_{K^0_s}\rangle\langle N_{K^\pm}\rangle}$) and mean charged-particle multiplicity ($\langle dN_{ch}/d\eta\rangle$) were independent of the considered collision centrality class for the baseline measurement, where DCC fluctuations were not introduced. However, with the implementation of DCC fluctuations in the MC model, the scaled values were no longer invariant with centrality but sharply rose in most central collisions. The scaled values of the MC (containing DCC fluctuations) were consistent with the ALICE measurement for $\nu_{dyn}[K^0_s, K^\pm]$.

The mechanism of particle production in high energy hadronic and heavy-ion collisions were studied using different phenomenological approaches in this thesis. The first approach involved a two-component Glauber model, which was used to describe the contribution of hard and soft processes towards particle production in heavy-ion (Au-Au and Pb-Pb) collisions. The model aptly described the charged particle multiplicity density and the transverse energy density. It was observed that the fractional contribution of hard processes increased with the increase in beam energy. A pairwise ratio of multiplicity densities for two different energies was obtained for similar $\langle N_{part}\rangle$ values. A scaling observed for the pairwise ratio indicated that the observed trend was due to the contribution from the hard scattering component and the energy difference while the same was not observed for transverse energy densitites. The second approach involved the study of the normalized moments of multiplicity distribution in pp collisions in the forward rapidity region using the Weibull model. Two different event classes, NSD (non-singly diffractive events) and INEL > 0 (inelastic events having at least one charged particle for $|\eta| < 1.0$) were considered for this study. The model described the charged particle multiplicity distributions quite well. The higher order normalized cumulants and factorial moments (upto 5^{th} order) were calculated from the extracted fit parameters in different event classes for various η intervals. The normalized cumulants and factorial moments showed an increasing trend with the increase in energy for all η windows, however, the second order moments exhibited no beam energy dependence. The observed trend of the higher order moments with beam energy suggested a strong violation of KNO scaling in forward regions, obtained for both NSD and INEL > 0 event classes. The third approach involved the study of enhancement of strange particles in high multiplicity pp collisions using rope hadronization mechanism implemented in PYTHIA8 model. The measured strangeness enhancement in pp collisions at $\sqrt{s} = 7$ TeV in ALICE was well described by the rope hadronization mechanism within the framework of color reconnection, while the values obtained without the effect of rope hadronization failed to describe the measured data. The values obtained from the rope hadronization without the color reconnection also failed to describe the data, which indicated that the color reconnection framework is needed with the rope hadronization mechanism to describe the enhancement in data. The observed enhancement of strange particles saturated at higher multiplicities and was independent of the collision energies. The production mechanism of various resonance baryons and mesons can be studied by rope hadronization mechanism. The heavy quark (charm and bottom) productions can also be explored in this microscopic model of rope hadronization.

References

[1] M. Breidenbach, J. I. Friedman, H. W. Kendall, E. D. Bloom, D. H. Coward, H. DeStaebler, J. Drees, L. W. Mo, and R. E. Taylor, "Observed behavior of highly inelastic electron-proton scattering," *Phys. Rev. Lett.* **23** (Oct, 1969) 935–939. `https://link.aps.org/doi/10.1103/PhysRevLett.23.935`.

[2] D. Griffiths, *Introduction to Elementary Particles*. John Wiley and Sons, 1 ed., 1987.

[3] https://home.cern/science/physics/standard model.

[4] A. Halzen, Francis; Martin, *Quarks and Leptons: An Introductory Course in Modern Particle Physics*. John Wiley and Sons, 1 ed., 1983.

[5] S. Bethke, "Experimental tests of asymptotic freedom," *Prog. Part. Nucl. Phys.* **58** (2007) 351–386, `arXiv:hep-ex/0606035 [hep-ex]`.

[6] D. J. Gross and F. Wilczek, "Ultraviolet behavior of non-abelian gauge theories," *Phys. Rev. Lett.* **30** (Jun, 1973) 1343–1346. `https://link.aps.org/doi/10.1103/PhysRevLett.30.1343`.

[7] H. D. Politzer, "Reliable perturbative results for strong interactions?," *Phys. Rev. Lett.* **30** (Jun, 1973) 1346–1349. `https://link.aps.org/doi/10.1103/PhysRevLett.30.1346`.

[8] F. Karsch, *Lattice QCD at High Temperature and Density*, pp. 209–249. Springer Berlin Heidelberg, Berlin, Heidelberg, 2002. `https://doi.org/10.1007/3-540-45792-5_6`.

[9] R. Rapp and J. Wambach, *Chiral Symmetry Restoration and Dileptons in Relativistic Heavy-Ion Collisions*, pp. 1–205. Springer US, Boston, MA, 2002. `https://doi.org/10.1007/0-306-47101-9_1`.

[10] A. P. F. Karsch, E. Laermann, “The pressure in 2, 2+1 and 3 flavour qcd,” *Physics Letters B* **478** (Apr, 2000) 447–455.

[11] F. W. Mark Alford, Krishna Rajagopal, “Qcd at finite baryon density: nucleon droplets and color superconductivity,” *Physics Letters B* **422** (Mar, 1998) 247–256.

[12] M. A. Halasz, A. D. Jackson, R. E. Shrock, M. A. Stephanov, and J. J. M. Verbaarschot, “Phase diagram of qcd,” *Phys. Rev. D* **58** (Sep, 1998) 096007. `https://link.aps.org/doi/10.1103/PhysRevD.58.096007`.

[13] S. Voloshin and Y. Zhang, “Flow study in relativistic nuclear collisions by fourier expansion of azimuthal particle distributions,”. `https://doi.org/10.1007/s002880050141`.

[14] A. M. Poskanzer and S. A. Voloshin, “Methods for analyzing anisotropic flow in relativistic nuclear collisions,” *Phys. Rev. C* **58** (Sep, 1998) 1671–1678. `https://link.aps.org/doi/10.1103/PhysRevC.58.1671`.

[15] R. Snellings, “Elliptic Flow: A Brief Review,” *New J. Phys.* **13** (2011) 055008, `arXiv:1102.3010 [nucl-ex]`.

[16] **NA49 Collaboration** Collaboration, H. A. et al, “Directed and elliptic flow in 158 gev/nucleon $pb + pb$ collisions,” *Phys. Rev. Lett.* **80** (May, 1998) 4136–4140. `https://link.aps.org/doi/10.1103/PhysRevLett.80.4136`.

[17] **STAR Collaboration** Collaboration, K. H. e. a. Ackermann, “Elliptic flow in $au + au$ collisions at $\sqrt{s_{\mathrm{nn}}} = 130\mathrm{GeV}$,” *Phys. Rev. Lett.* **86** (Jan, 2001) 402–407. `https://link.aps.org/doi/10.1103/PhysRevLett.86.402`.

[18] **ALICE Collaboration** Collaboration, K. e. a. Aamodt, “Higher harmonic anisotropic flow measurements of charged particles in pb-pb collisions at $\sqrt{s_{NN}} = 2.76$ TeV,” *Phys. Rev. Lett.* **107** (Jul, 2011) 032301. `https://link.aps.org/doi/10.1103/PhysRevLett.107.032301`.

[19] **ALICE Collaboration** Collaboration, J. e. a. Adam, “Anisotropic flow of charged particles in pb-pb collisions at $\sqrt{s_{NN}} = 5.02$ TeV,” *Phys. Rev. Lett.* **116** (Apr, 2016) 132302. `https://link.aps.org/doi/10.1103/PhysRevLett.116.132302`.

[20] **ATLAS Collaboration** Collaboration, G. e. a. Aad, "Measurement of the azimuthal anisotropy for charged particle production in $\sqrt{s_{NN}} = 2.76$ tev lead-lead collisions with the atlas detector," *Phys. Rev. C* **86** (Jul, 2012) 014907. `https://link.aps.org/doi/10.1103/PhysRevC.86.014907`.

[21] **CMS Collaboration** Collaboration, S. e. a. Chatrchyan, "Measurement of higher-order harmonic azimuthal anisotropy in pbpb collisions at $\sqrt{s_{NN}} = 2.76$ tev," *Phys. Rev. C* **89** (Apr, 2014) 044906. `https://link.aps.org/doi/10.1103/PhysRevC.89.044906`.

[22] **ALICE Collaboration** Collaboration, S. A. et al., "Anisotropic flow in xeâĂŞxe collisions at snn=5.44 tev," *Physics Letters B* **784** (2018) 82 – 95. `http://www.sciencedirect.com/science/article/pii/S037026931830515X`.

[23] **ALICE** Collaboration, K. Aamodt *et al.*, "Elliptic flow of charged particles in Pb-Pb collisions at 2.76 TeV," *Phys. Rev. Lett.* **105** (2010) 252302, `arXiv:1011.3914 [nucl-ex]`.

[24] **ALICE** Collaboration, S. Acharya *et al.*, "Investigations of anisotropic flow using multi-particle azimuthal correlations in pp, p-Pb, Xe-Xe, and Pb-Pb collisions at the LHC," `arXiv:1903.01790 [nucl-ex]`.

[25] **ALICE** Collaboration, B. B. Abelev *et al.*, "Multi-strange baryon production at mid-rapidity in Pb-Pb collisions at $\sqrt{s_{NN}} = 2.76$ TeV," *Phys. Lett.* **B728** (2014) 216–227, `arXiv:1307.5543 [nucl-ex]`. [Erratum: Phys. Lett.B734,409(2014)].

[26] **ALICE** Collaboration, J. Adam *et al.*, "Enhanced production of multi-strange hadrons in high-multiplicity proton-proton collisions," *Nature Phys.* **13** (2017) 535–539, `arXiv:1606.07424 [nucl-ex]`.

[27] J. Rafelski and B. Müller, "Strangeness production in the quark-gluon plasma," *Phys. Rev. Lett.* **48** (Apr, 1982) 1066–1069. `https://link.aps.org/doi/10.1103/PhysRevLett.48.1066`.

[28] **STAR Collaboration** Collaboration, B. I. e. a. Abelev, "Enhanced strange baryon production in au+au collisions compared to $p + p$ at $\sqrt{s_{NN}} = 200$ gev," *Phys. Rev. C* **77** (Apr, 2008) 044908. `https://link.aps.org/doi/10.1103/PhysRevC.77.044908`.

[29] H. Heiselberg, "Event-by-event physics in relativistic heavy ion collisions," *Phys. Rept.* **351** (2001) 161–194, `arXiv:nucl-th/0003046 [nucl-th]`.

[30] V. Koch, "Aspects of chiral symmetry," *Int. J. Mod. Phys.* **E6** (1997) 203–250, `arXiv:nucl-th/9706075 [nucl-th]`.

[31] J. D. Bjorken, K. L. Kowalski, and C. C. Taylor, "Baked Alaska," in *Results and perspectives in particle physics.Proceedings, Les Rencontres de Physique de lq Vallee d'Aoste, La Thuile, Italy, March 7 - 13, 1993*, pp. 507–528. 1993. `http://www-public.slac.stanford.edu/sciDoc/docMeta.aspx?slacPubNumber=SLAC-PUB-6109`.

[32] J. D. Bjorken, "Disoriented chiral condensate: Theory and phenomenology," *Acta Phys. Polon.* **B28** (1997) 2773–2791, `arXiv:hep-ph/9712434 [hep-ph]`.

[33] K. Rajagopal and F. Wilczek, "Static and dynamic critical phenomena at a second order QCD phase transition," *Nucl. Phys.* **B399** (1993) 395–425, `arXiv:hep-ph/9210253 [hep-ph]`.

[34] J. Schaffner-Bielich and J. Randrup, "Disoriented chiral condensate dynamics with the su(3) linear sigma model," *Phys. Rev. C* **59** (Jun, 1999) 3329–3342. `https://link.aps.org/doi/10.1103/PhysRevC.59.3329`.

[35] S. Gavin, "Disoriented chiral condensates," *Nucl. Phys.* **A590** (1995) 163C–177C.

[36] S. Gavin and J. I. Kapusta, "Kaon and pion fluctuations from small disoriented chiral condensates," *Phys. Rev.* **C65** (2002) 054910, `arXiv:nucl-th/0112083 [nucl-th]`.

[37] **STAR** Collaboration, L. Adamczyk *et al.*, "Charged-to-neutral correlation at forward rapidity in Au+Au collisions at $\sqrt{s_{NN}}$=200 GeV," *Phys. Rev.* **C91** no. 3, (2015) 034905, `arXiv:1408.5017 [nucl-ex]`.

[38] J. I. Kapusta and S. M. H. Wong, "Is anomalous production of Ω and $\overline{\Omega}$ evidence for disoriented chiral condensates?," *Phys. Rev. Lett.* **86** (May, 2001) 4251–4254. `https://link.aps.org/doi/10.1103/PhysRevLett.86.4251`.

[39] M. Abdel-Aziz and S. Gavin, "Strange fluctuations at RHIC," *Nucl. Phys.* **A715** (2003) 657–660, `arXiv:nucl-th/0209019 [nucl-th]`. [J. Phys.G30,S271(2004)].

[40] L. Evans and P. Bryant, "LHC Machine," *JINST* **3** (2008) S08001.

[41] J. Haffner, "The CERN accelerator complex. Complexe des accÃl'lÃl'rateurs du CERN,". http://cds.cern.ch/record/1621894. General Photo.

[42] **ALICE** Collaboration, K. Aamodt *et al.*, "The ALICE experiment at the CERN LHC," *JINST* **3** (2008) S08002.

[43] **ALICE** Collaboration, P. Cortese *et al.*, "ALICE: Physics performance report, volume I," *J. Phys.* **G30** (2004) 1517–1763.

[44] **ALICE** Collaboration, G. Dellacasa *et al.*, "ALICE technical design report of the inner tracking system (ITS),".

[45] **ALICE** Collaboration, K. Aamodt *et al.*, "Alignment of the ALICE Inner Tracking System with cosmic-ray tracks," *JINST* **5** (2010) P03003, arXiv:1001.0502 [physics.ins-det].

[46] **ALICE** Collaboration, G. Dellacasa *et al.*, "ALICE: Technical design report of the time projection chamber,".

[47] W. Blum, L. Rolandi, and W. Riegler, *Particle detection with drift chambers*. Particle Acceleration and Detection. 2008. http://www.springer.com/physics/elementary/book/978-3-540-76683-4.

[48] **ALICE** Collaboration, G. Dellacasa *et al.*, "ALICE technical design report of the time-of-flight system (TOF),".

[49] **ALICE** Collaboration, P. Cortese *et al.*, "ALICE technical design report on forward detectors: FMD, T0 and V0,".

[50] **ALICE** Collaboration, F. Carena *et al.*, "The ALICE data acquisition system," *Nucl. Instrum. Meth.* **A741** (2014) 130–162.

[51] C. Pruneau, S. Gavin, and S. Voloshin, "Methods for the study of particle production fluctuations," *Phys. Rev. C* **66** (Oct, 2002) 044904. https://link.aps.org/doi/10.1103/PhysRevC.66.044904.

[52] P. Christiansen, E. Haslum, and E. Stenlund, "Number-ratio fluctuations in high-energy particle production," *Phys. Rev. C* **80** (Sep, 2009) 034903. https://link.aps.org/doi/10.1103/PhysRevC.80.034903.

[53] R. Nayak, S. Dash, B. Nandi, and C. Pruneau, "Modeling of Charged-Neutral Kaon Fluctuations as a Signature of DCC Production in A–A Collisions," arXiv:1908.01130 [hep-ph].

[54] B. K. Nandi, G. C. Mishra, B. Mohanty, D. P. Mahapatra, and T. K. Nayak, "Search for DCC in relativistic heavy ion collision through event shape analysis," *Phys. Lett.* **B449** (1999) 109–113, arXiv:nucl-ex/9812004 [nucl-ex].

[55] P. Tribedy, S. Chattopadhyay, and A. Tang, "Study of gamma-charge correlation in heavy ion collisions, various approaches," *Phys. Rev.* **C85** (2012) 024902, arXiv:1108.2495 [nucl-ex].

[56] X.-N. Wang and M. Gyulassy, "HIJING: A Monte Carlo model for multiple jet production in p p, p A and A A collisions," *Phys. Rev.* **D44** (1991) 3501–3516.

[57] Z.-W. Lin, C. M. Ko, B.-A. Li, B. Zhang, and S. Pal, "A Multi-phase transport model for relativistic heavy ion collisions," *Phys. Rev.* **C72** (2005) 064901, arXiv:nucl-th/0411110 [nucl-th].

[58] M. L. Miller, K. Reygers, S. J. Sanders, and P. Steinberg, "Glauber modeling in high energy nuclear collisions," *Ann. Rev. Nucl. Part. Sci.* **57** (2007) 205–243, arXiv:nucl-ex/0701025 [nucl-ex].

[59] **ALICE** Collaboration, B. Abelev *et al.*, "Centrality determination of Pb-Pb collisions at $\sqrt{s_{NN}}$ = 2.76 TeV with ALICE," *Phys. Rev.* **C88** no. 4, (2013) 044909, arXiv:1301.4361 [nucl-ex].

[60] D. Kharzeev and M. Nardi, "Hadron production in nuclear collisions at RHIC and high density QCD," *Phys. Lett.* **B507** (2001) 121–128, arXiv:nucl-th/0012025 [nucl-th].

[61] **ALICE Collaboration** Collaboration, "The ALICE definition of primary particles,". https://cds.cern.ch/record/2270008.

[62] **STAR** Collaboration, X.-F. Luo, "Probing the QCD Critical Point with Higher Moments of Net-proton Multiplicity Distributions," *J. Phys. Conf. Ser.* **316** (2011) 012003, arXiv:1106.2926 [nucl-ex].

[63] **ALICE** Collaboration, B. Abelev *et al.*, "Centrality dependence of π, K, p production in Pb-Pb collisions at $\sqrt{s_{NN}}$ = 2.76 TeV," *Phys. Rev.* **C88** (2013) 044910, arXiv:1303.0737 [hep-ex].

[64] **ALICE** Collaboration, B. B. Abelev *et al.*, "K_S^0 and Λ production in Pb-Pb collisions at $\sqrt{s_{NN}}$ = 2.76 TeV," *Phys. Rev. Lett.* **111** (2013) 222301, arXiv:1307.5530 [nucl-ex].

[65] **NA50** Collaboration, M. C. Abreu *et al.*, "Pseudorapidity distributions of chargedparticles as a function of centrality in Pb Pb collisions at 158-GeV and 40-GeV per nucleon incident energy," *Phys. Lett.* **B530** (2002) 33–42.

[66] **WA98** Collaboration, M. M. Aggarwal *et al.*, "Scaling of particle and transverse energy production in Pb-208 + Pb-208 collisions at 158-A-GeV," *Eur. Phys. J.* **C18** (2001) 651–663, `arXiv:nucl-ex/0008004 [nucl-ex]`.

[67] **NA57, WA97** Collaboration, N. Carrer *et al.*, "Determination of the event centrality in the WA97 and NA57 experiments," *J. Phys.* **G27** (2001) 391–396.

[68] **ALICE** Collaboration, K. Aamodt *et al.*, "Centrality dependence of the charged-particle multiplicity density at mid-rapidity in Pb-Pb collisions at $\sqrt{s_{NN}}$ = 2.76 TeV," *Phys. Rev. Lett.* **106** (2011) 032301, `arXiv:1012.1657 [nucl-ex]`.

[69] **PHOBOS** Collaboration, B. B. Back *et al.*, "Collision geometry scaling of Au+Au pseudorapidity density from s(NN)**(1/2) = 19.6-GeV to 200-GeV," *Phys. Rev.* **C70** (2004) 021902, `arXiv:nucl-ex/0405027 [nucl-ex]`.

[70] **ALICE** Collaboration, J. Adam *et al.*, "Charged-particle multiplicities in protonâĂŞproton collisions at $\sqrt{s}$ = 0.9 to 8 TeV," *Eur. Phys. J.* **C77** no. 1, (2017) 33, `arXiv:1509.07541 [nucl-ex]`.

[71] **ALICE** Collaboration, J. Adam *et al.*, "Pseudorapidity and transverse-momentum distributions of charged particles in protonâĂŞproton collisions at $\sqrt{s}$ = 13 TeV," *Phys. Lett.* **B753** (2016) 319–329, `arXiv:1509.08734 [nucl-ex]`.

[72] S. Dash, B. K. Nandi, R. Nayak, A. K. Pandey, and P. Sett, "Comprehending particle production at RHIC and LHC energies using global measurements," *Mod. Phys. Lett.* **A32** no. 2, (2017) 1750060, `arXiv:1609.08609 [nucl-th]`.

[73] **PHENIX** Collaboration, A. Adare *et al.*, "Transverse energy production and charged-particle multiplicity at midrapidity in various systems from $\sqrt{s_{NN}}$ = 7.7 to 200 GeV," *Phys. Rev.* **C93** no. 2, (2016) 024901, `arXiv:1509.06727 [nucl-ex]`.

[74] **ALICE** Collaboration, J. Adam *et al.*, "Centrality dependence of the charged-particle multiplicity density at midrapidity in Pb-Pb collisions at $\sqrt{s_{\mathrm{NN}}}$ = 5.02 TeV," *Phys. Rev. Lett.* **116** no. 22, (2016) 222302, `arXiv:1512.06104 [nucl-ex]`.

[75] **ALICE** Collaboration, C. Loizides, "Charged-particle multiplicity and transverse energy in Pb-Pb collisions at $\sqrt{s_{NN}} = 2.76$ TeV with ALICE," *J. Phys.* **G38** (2011) 124040, `arXiv:1106.6324 [nucl-ex]`.

[76] **ALICE** Collaboration, S. Acharya *et al.*, "Charged-particle multiplicity distributions over a wide pseudorapidity range in proton-proton collisions at $\sqrt{s} =$ 0.9, 7, and 8 TeV," *Eur. Phys. J.* **C77** no. 12, (2017) 852, `arXiv:1708.01435 [hep-ex]`.

[77] R. Corke and T. Sjostrand, "Multiparton Interactions and Rescattering," *JHEP* **01** (2010) 035, `arXiv:0911.1909 [hep-ph]`.

[78] W. Kittel and E. A. De Wolf, *Soft multihadron dynamics*. 2005.

[79] E. A. De Wolf, I. M. Dremin, and W. Kittel, "Scaling laws for density correlations and fluctuations in multiparticle dynamics," *Phys. Rept.* **270** (1996) 1–141, `arXiv:hep-ph/9508325 [hep-ph]`.

[80] T. Sjostrand, S. Mrenna, and P. Z. Skands, "A Brief Introduction to PYTHIA 8.1," *Comput. Phys. Commun.* **178** (2008) 852–867, `arXiv:0710.3820 [hep-ph]`.

[81] F. W. Bopp, R. Engel, and J. Ranft, "Rapidity gaps and the PHOJET Monte Carlo," in *High energy physics. Proceedings, LAFEX International School, Session C, Workshop on Diffractive Physics, LISHEP'98, Rio de Janeiro, Brazil, February 16-20, 1998*, pp. 729–741. 1998. `arXiv:hep-ph/9803437 [hep-ph]`.

[82] **CMS** Collaboration, V. Khachatryan *et al.*, "Charged Particle Multiplicities in *pp* Interactions at $\sqrt{s} = 0.9$, 2.36, and 7 TeV," *JHEP* **01** (2011) 079, `arXiv:1011.5531 [hep-ex]`.

[83] **LHCb** Collaboration, R. Aaij *et al.*, "Measurement of charged particle multiplicities in *pp* collisions at $\sqrt{s} = 7$TeV in the forward region," *Eur. Phys. J.* **C72** (2012) 1947, `arXiv:1112.4592 [hep-ex]`.

[84] E. K. G. Sarkisian, "Description of local multiplicity fluctuations and genuine multiparticle correlations," *Phys. Lett.* **B477** (2000) 1–12, `arXiv:hep-ph/0001262 [hep-ph]`.

[85] R. K. Nayak, S. Dash, E. K. Sarkisyan-Grinbaum, and M. Tasevsky, "Describing dynamical fluctuations and genuine correlations by Weibull regularity," `arXiv:1704.08377 [hep-ph]`.

[86] B. W. K and W. K. H *J. Appl. Phys.* **78** (1995) 2758.

[87] S. Dash, B. K. Nandi, and P. Sett, "Weibull model of Multiplicity Distribution in hadron-hadron collisions," *Phys. Rev.* **D93** no. 11, (2016) 114022, `arXiv:1409.5831 [hep-ph]`.

[88] S. Dash, B. K. Nandi, and P. Sett, "Multiplicity distributions for e^+e^- collisions using Weibull distribution," *Phys. Rev.* **D94** no. 7, (2016) 074044, `arXiv:1607.08688 [hep-ph]`.

[89] R. Nayak and S. Dash, "Multiplicity distribution and normalized moments in pâĂŞp collisions at LHC in forward rapidity using Weibull model," *J. Phys.* **G46** no. 7, (2019) 075003, `arXiv:1802.06990 [hep-ph]`.

[90] A. K. Pandey, P. Sett, and S. Dash, "Weibull Distribution and the multiplicity moments in $pp\,(p\bar{p})$ collisions," *Phys. Rev.* **D96** no. 7, (2017) 074006, `arXiv:1706.07585 [hep-ph]`.

[91] J. Rafelski and B. Muller, "Strangeness Production in the Quark - Gluon Plasma," *Phys. Rev. Lett.* **48** (1982) 1066. [Erratum: Phys. Rev. Lett.56,2334(1986)].

[92] **CMS** Collaboration, V. Khachatryan *et al.*, "Observation of Long-Range Near-Side Angular Correlations in Proton-Proton Collisions at the LHC," *JHEP* **09** (2010) 091, `arXiv:1009.4122 [hep-ex]`.

[93] **CMS** Collaboration, V. Khachatryan *et al.*, "Measurement of long-range near-side two-particle angular correlations in pp collisions at $\sqrt{s}$ =13 TeV," *Phys. Rev. Lett.* **116** no. 17, (2016) 172302, `arXiv:1510.03068 [nucl-ex]`.

[94] **ATLAS** Collaboration, G. Aad *et al.*, "Observation of Long-Range Elliptic Azimuthal Anisotropies in $\sqrt{s}$ =13 and 2.76 TeV pp Collisions with the ATLAS Detector," *Phys. Rev. Lett.* **116** no. 17, (2016) 172301, `arXiv:1509.04776 [hep-ex]`.

[95] P. Koch, B. Muller, and J. Rafelski, "Strangeness in Relativistic Heavy Ion Collisions," *Phys. Rept.* **142** (1986) 167–262.

[96] B. Andersson, G. Gustafson, G. Ingelman, and T. Sjostrand, "Parton Fragmentation and String Dynamics," *Phys. Rept.* **97** (1983) 31–145.

[97] C. Bierlich, "Microscopic collectivity: The ridge and strangeness enhancement from stringâĂŞstring interactions," *Nucl. Phys.* **A982** (2019) 499–502, arXiv:1807.05271 [nucl-th].

[98] C. Flensburg, G. Gustafson, and L. Lonnblad, "Inclusive and Exclusive Observables from Dipoles in High Energy Collisions," *JHEP* **08** (2011) 103, arXiv:1103.4321 [hep-ph].

[99] C. Bierlich, G. Gustafson, L. LÃűnnblad, and A. Tarasov, "Effects of Overlapping Strings in pp Collisions," *JHEP* **03** (2015) 148, arXiv:1412.6259 [hep-ph].

[100] B. Andersson, G. Gustafson, and B. Soderberg, "A General Model for Jet Fragmentation," *Z. Phys.* **C20** (1983) 317.

[101] B. Andersson and G. Gustafson, "Semiclassical Models for Gluon Jets and Leptoproduction Based on the Massless Relativistic String," *Z. Phys.* **C3** (1980) 223.

[102] T. S. Biro, H. B. Nielsen, and J. Knoll, "Color Rope Model for Extreme Relativistic Heavy Ion Collisions," *Nucl. Phys.* **B245** (1984) 449–468.

[103] C. Bierlich and J. R. Christiansen, "Effects of color reconnection on hadron flavor observables," *Phys. Rev.* **D92** no. 9, (2015) 094010, arXiv:1507.02091 [hep-ph].

[104] C. Bierlich, G. Gustafson, and L. LÃűnnblad, "A shoving model for collectivity in hadronic collisions," arXiv:1612.05132 [hep-ph].

[105] R. Nayak, S. Pal, and S. Dash, "Effect of rope hadronization on strangeness enhancement in p−p collisions at LHC energies," *Phys. Rev.* **D100** no. 7, (2019) 074023, arXiv:1812.07718 [hep-ph].

[106] C. Bierlich, "Rope Hadronization and Strange Particle Production," *EPJ Web Conf.* **171** (2018) 14003, arXiv:1710.04464 [nucl-th].

[107] T. SjÃűstrand, S. Ask, J. R. Christiansen, R. Corke, N. Desai, P. Ilten, S. Mrenna, S. Prestel, C. O. Rasmussen, and P. Z. Skands, "An Introduction to PYTHIA 8.2," *Comput. Phys. Commun.* **191** (2015) 159–177, arXiv:1410.3012 [hep-ph].

[108] P. Skands, S. Carrazza, and J. Rojo, "Tuning PYTHIA 8.1: the Monash 2013 Tune," *Eur. Phys. J.* **C74** no. 8, (2014) 3024, arXiv:1404.5630 [hep-ph].

[109] J. R. Christiansen and P. Z. Skands, "String Formation Beyond Leading Colour," *JHEP* **08** (2015) 003, `arXiv:1505.01681 [hep-ph]`.

[110] **ALICE** Collaboration, V. Vislavicius, "Multiplicity dependence of identified particle production in proton-proton collisions with ALICE," *Nucl. Phys.* **A967** (2017) 337–340, `arXiv:1704.04737 [hep-ex]`.

List of Publications

1. Ranjit Nayak, Sadhana Dash and Subhadip Pal, Effect of Rope Hadronisation on Strangeness Enhancement in p-p collisions at LHC energies, arXiv:1812.07718, Phys. Rev. D 100, 074023 (2019).

2. Ranjit Nayak and Sadhana Dash, Multiplicity distribution and normalized moments in p-p collisions at LHC in forward rapidity using Weibull model, arXiv:1802.06990, J.Phys. G46 (2019) no.7, 075003.

3. Sadhana Dash, B.K. Nandi, Ranjit Nayak et al, Comprehending particle production at RHIC and LHC energies using global measurements, arXiv:1609.08609, Mod. Phys. Lett. A 32, 1750060 (2017).

4. Ranjit Nayak, Sadhana Dash, Claude A. Pruneau, Basanta K. Nandi, Modelling of Charged-Neutral Kaon Fluctuations as a Signature of DCC Production in A–A Collisions, arxiv:1908.01130. PRC 004900 (2020).

5. Nirbhay K Behera, Ranjit Nayak and Sadhana Dash, Baseline study for net-proton number fluctuations at top RHIC and LHC energies with Angantyr model, arXiv:1909.12113. To be published in PRC.

6. Ankita Goswami, Ranjit Nayak, B.K. Nandi and Sadhana Dash, Effect of color reconnection and rope formation on resonance production in p-p collisions in Pythia 8, arXiv:1911.00559.

7. Ranjit Nayak et al, Describing dynamical fluctuations and genuine correlations by Weibull regularity, arXiv:1704.08377

6.1 Conference Publications

1. R. Nayak et. al. Study of Centrality and Beam Energy Dependence of $dN_{ch}/d\eta$ and $dE_T/d\eta$ at Midrapidity Using Two Component Approach presented in XXII DAE

High Energy Physics Symposium at Delhi University, 12 -16 Dec 2016, Delhi, India, published in Springer Proc.Phys. 203 (2018) 267-270.

2. R. Nayak et. al. Weibull Approach to Study Multiplicity Moments in e^+e^- and p$\bar{p}$ Collisions presented in XXII DAE High Energy Physics Symposium at Delhi University, 12 -16 Dec 2016, Delhi, India, published in Springer Proc.Phys. 203 (2018) 263-266.

3. R.Nayak [ALICE collaboration] Kaon Isospin Fluctuations in Pb-Pb Collisions at $\sqrt{s_{NN}}$ = 2.76 TeV with ALICE at the LHC presented in HOT Quarks 2018 conference at Texel, The Neatherlands, 7-15 September 2018. MDPI Proc. 10 (2019) no.1, 22.

4. R.Nayak [ALICE collaboration] Relative Yield of Neutral and Charged Kaons in Pb-Pb Collisions at $\sqrt{s_{NN}}$ = 2.76 TeV with ALICE at the LHC presented in EPS HEP 2019 conference at Ghent, Belgium, 10-17 July 2019. To be published in Proceedings of Science (PoS).

Acknowledgements

I wish to express my deepest gratitude to my supervisor, Professor Sadhana Dash, who has the substance of a genius: she convincingly guided and encouraged me to be professional and do the right thing even when the road got tough. Without her persistent help, the goal of this thesis would not have been realized. She has guided me from installing analysis software to do physics analysis. I will be indebted to her for her constant constructive criticism and invaluable ideas which made me focused throughout my PhD period. I can not forget her support, co-operation and meaningful advice to my life. Thank you madam for giving me the opportunity to be a small part in your career and I owe you all success ahead.

I would like to extend my deepest regards to Prof. Claude A. Pruneau, for his guidance on my work. Despite living in different time zones, we have made countless valuable discussions. I would like to thank him from the bottom of my heart for patiently helping me in my work. He is like a mentor, friend and philosopher to me. My learning from him will continue throughout my life.

I would like to pay my special thanks to Prof. Basanta Kumar Nandi for his useful discussions in weekly group meetings. He always motivated me to do qualitative physics in my career. I am highly benefited for his continuous encouragements, and my understanding on DCC physics has broadened after many useful discussions with him. I would like to express my gratitude for his constant support and providing me all opportunities during my PhD period.

I am also thankful to Prof. Raghava Varma for his advice to do constructive research during my initial days at IIT Bombay. I am obliged to Prof. S. Umasankar for consistently evaluating me after each annual progress seminar. I am also thankful to Prof. Urjit A Yajnik for discussion and lectures on topological defects. I would like to thank all my professors who taught me during my PhD coursework.

Special thanks goes to ALICE-India collaboration members with whom I have discussed most of my analysis results. I can not stop here to mention Dr. Tapan K. Nayak who constantly discusses my analysis results whenever I was at CERN. I am also thankful to Prof. Bedangdas Mohanty for constantly encouraging me and motivated me to do the DCC analysis. I am also thankful to Prof. Sudhir Raniwala for many scientific discussions on my analysis during collaboration meetings. I am also thankful to Dr. Subhasis Chattopadhaya for his constant support and providing me all opportunities during my analysis work. I would also like to thank Prof. Pradip Sahu and Dr. Saikat Biswas for giving me the opportunity to learn the making of GEM foils at IOP Bhubaneswar.

It was really great opportunity for me to work with Prof. Anthony R. Timmins and Dr. Marco V. Leeuwen for many technical discussions regarding to my analysis work. I would like to thank all ALICE collaboration members for their valuable comments on my analysis work.

I wish to express my sincere thanks to Dr. Prithwish Tribedy, Prof. Chitrasen Jena, Prof. Prabhat R. Pujahari, Dr. Priyanka Sett and Dr. Nirbhaya K. Behera for many countless physics discussions during this work.

I wished to thank my friend Dr. Arvind Khuntia, Debasish Mallick and Dr. Prasanna K. Dhani for many useful discussions regarding statistical measurements and QCD physics. I am also thankful to all my M.Sc. batch mates of Utkal University for their enormous love and encouragement.

I was lucky to always have some great people around me at IIT Bombay. They have made my PhD life jovial with their help and good wishes. My sincere thanks to all of them - Saswati, Geeta, Arabinda, Suman, Saptak, Kausik, Elizabeth, Deepak, Chanchal, Priyanka. I am also lucky to have some wonderful lab-mates with whom I have many countless discussions regarding each others work. Thank you Dr. Himani Bhatt, Dr. Ashutosh Pandey, Dr. Pragati Sahoo, Dr. Ankita Goswami, Bharati, Baidya, Tulika, Dibakar, Pritam, Dr. Preeti Dhankar, Dr. Manoj Jadhav, Dr. Shyam Kumar for your love and support.

At the end, most importantly I would like to express my respect and humbleness to my grandmother and my parents for their never ending blessings. This thesis would not have been possible without their patience and encouragement. I am also thankful to my younger brother for his moral support during this thesis work. Also my sincere thanks to my wife JyotiAmrita for her patience and support during difficult times throughout.